Low Energy Cosmic Ray Anisotropies Observed using the Pierre Auger Observatory

Kerridwen Bette Barber

B.Sc. (Hons)

A thesis presented to the University of Adelaide

for admission to the degree of

Doctor of Philosophy

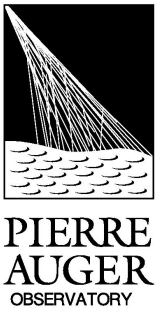

School of Chemistry & Physics

Department of Physics

July 2014

Contents

Abstract

The Pierre Auger Observatory is a hybrid cosmic ray detector located in the high plains of Argentina. It comprises an array of water-Cherenkov stations overlooked by four fluorescence detector sites and was designed and built for the purpose of studying ultra-high energy cosmic rays ($>10^{18}$ eV). Due to the distribution of cosmic ray energies following a power law, in the process of studying these high energy events, the observatory also collects vast amounts of data on lower energy cosmic ray events. The low solar activity of the 2006 to 2009 period presents an opportunity to study the behaviour of the very low cosmic ray flux which would otherwise be overwhelmed by the solar wind during more active periods.

This research aims to investigate the anisotropy in the low energy cosmic ray flux in the southern hemisphere using the calibration data for the Pierre Auger Observatory's surface detector. The energy ranges accessible via these calibration data were determined via numerical simulation of both air shower propagation through the atmosphere as well as the surface detector response to the surface particles, and were found to be of the order of 100 GeV. Following corrections to remove atmospheric and other spurious effects, investigations into the anisotropy present in the data were performed in both solar and sidereal time, spanning periods of both low and high solar activity.

Declaration of Originality

I, Kerridwen Bette Barber, certify that this work contains no material which has been accepted for the award of any other degree or diploma in my name in any university of other tertiary institution and, to the best of my knowledge and belief, contains no material previously published or written by another person, except where due reference has been made in the text. In addition, I certify that no part of this work will, in the future be used as a submission in my name for any other degree or diploma in any university or other tertiary institution without the prior approval of the University of Adelaide and where applicable, any partner institution responsible for the joint award of this degree.

I give consent to this copy of my thesis, when deposited in the University Library, being made available for loan and photocopying, subject to the provisions of the Copyright Act 1968.

I also give permission for the digital version of my thesis to be made available on the web, via the University's digital research repository, the Library Search and also through web search engines, unless permission has been granted by the University to restrict access for a period of time.

Signed:..... **Date**: .....

Acknowledgements

First and foremost, I would like to acknowledge and thank my supervisors, Roger Clay and Bruce Dawson. I cannot thank them enough for the continued level of support, encouragement, knowledge, wisdom and patience that they have offered me over the course of my Ph.D.

I would also like to thank the other members of the High Energy Astrophysics group at the University of Adelaide, both past and present. It has been an absolute pleasure to study with them. In particular I would like to express my heartfelt thanks to my office mate, Ben Whelan. He has been an amazing source of kindness and enthusiasm; always happy to talk over any ideas, be a fresh pair of eyes, or even just help me believe that I could do this.

The opportunity to work with such a vast and diverse group as The Pierre Auger Collaboration (`www.auger.org/admin/Collaborators/author_list_alphabetical.html`) has been a wonderful experience. Particular thanks go to Xavier Bertou and Hernán Asorey for the very useful discussions about the low energy data possibilities that made this research possible.

My friends and family have offered unwavering love and support over the course of my studies. In particular, my close friend Myffie has been an amazing source of understanding and strength (and many cups of tea). My parents, John and Bette, have encouraged and supported me no matter what my decisions in life. Their unconditional love, support and knowing that they'll always be there has given me the strength to get through some of the more stressful times of my Ph.D.

I would also like to acknowledge my work colleagues at the Bureau of Meteorology who have put up with my "thesis stress" for the past months and have given me the time I needed to complete this work.

Last, but certainly not least, I would like to thank my partner in life, my husband, Matthew. He has been a constant source of love, support and strength. I cannot thank him enough for his unwavering faith in me, the patience he has shown, and the encouragement he's given me when I've needed it most. I cannot imaging trying to do this without him.

1: Introduction to Cosmic Rays

While the existence of mysterious charged particles were known before the start of the 20th century, it wasn't until this time that an understanding of the "cosmic" origin of these particles was developed. Before the start of the 20th century, it was known that electroscopes gradually lost their charge over time, even when kept in the dark and away from the presence of any radioactive source and, at the time, this was believed to be due to the presence of some kind of background ionising radiation of terrestrial origin. In 1912, Victor Hess performed balloon experiments that measured the ionising radiation variation up to around 5 km altitude hoping to show that the flux of this ionising radiation decreased [1]. However, what he instead found was that it increased with altitude beyond $\sim$ 2000 m rather than decreasing as he had expected, and so concluded that this radiation was instead of cosmic origin. Further experiments conducted during a solar eclipse showed no reduction in this radiation and so he could further conclude that it was not of solar origin either. In 1936 Hess was awarded the Nobel Prize for his discovery of cosmic radiation, which was later termed "cosmic rays" by Robert Milliken [2]. Werner Kolhörster expanded on Hess's experiments, measuring the variation of ionising radiation with altitude up to around 9 km [3]. He found that the radiation intensity at this altitude was around 50 times that at the Earth's surface. Kolhörster went on to establish the first institute dedicated to cosmic ray research [2].

Studies of cosmic rays at the Earth's surface do not directly detect the cosmic rays that have propagated through space. In the 1930s, the French physicist, Pierre Auger, performed a series of coincidence experiments in which he used Wilson chambers and Geiger-Müller tubes separated by large distances. He concluded that the particles being measured by his detectors were secondary particles produced in the atmosphere from a single primary particle [4]. These secondary particles are produced in a cascade as the primary cosmic ray particle interacts with the molecules near the top of the Earth's atmosphere and continues downwards to the Earth's surface. This cascade of secondary particles is known as an extensive air shower (EAS). From measurements of the properties of EAS at ground level it is possible to determine information about the nature of the primary cosmic ray particle. These early experiments showed cosmic ray particles with unexpectedly high energies (around

10^{15} eV)[4] and pioneering work done at the Volcano Ranch observatory revealed primary particles with energy in excess of 10^{20} eV [5]. Such unexpected discoveries led to further questions about the nature and origin of cosmic rays.

Early cosmic ray research also greatly advanced the understanding of particle physics and led to the discovery of new subatomic particles such as the positron in 1933 [6] and the muon in 1937 [7].

This chapter describes the current understanding of cosmic ray physics from the nature and energy spectrum of the cosmic ray flux as seen at the Earth to the possible sources and acceleration mechanisms of cosmic rays of varying energies. The interactions of cosmic rays with the Earth's atmosphere and the subsequent development of extensive air showers will also be described.

1.1 Energy Spectrum

The cosmic ray energy spectrum describes the particle flux as a function of energy and ranges from a few GeV to beyond 10^{20} eV. Figure 1.1.1 shows the differential all-particle spectrum which falls steeply with energy E and can be described by the power law:

$$\frac{dN}{dE} \propto E^{-\gamma} \tag{1.1.1}$$

in units of $\mathrm{m^{-2}s^{-1}sr^{-1}eV^{-1}}$ with $\gamma \simeq 2.7$.

The steepness of this energy spectrum is such that at GeV energies the flux is over 1,000 particles per square metre per second but around 1 PeV (10^{15} eV) the flux is only of the order of 1 particle per square metre per year. At even higher energies this flux further decreases to much less than 1 particle per square kilometre per century above 100 EeV (10^{20} eV). Consequently, in order to detect high energy cosmic rays, balloon and satellite experiments cease to be feasible and very large ground detectors are required. The detection of cosmic rays is described further in Section 2.1.

The spectrum is most accurately known below around 10^{15} eV since the primary cosmic ray flux can be measured directly by balloon and satellite experiments. These experiments allow not only the primary energy but also composition to be directly measured. This is not possible with the ground-based detectors. Determination of the properties of primary cosmic ray particles with ground-based detectors rely on reconstructions performed using measurements taken of the secondary particles at ground level.

The cosmic ray energy spectrum shows two major features. The first is a steepening of the fitted power law at around 10^{15} eV known as the "knee" where γ changes from around 2.7 to 3 and the second is a flattening around 10^{19} eV known as the

"ankle". In addition to these two main features, there is also a second slight steepening of the spectrum at around 10^{17} eV which is known as the "second knee" where γ changes from around 3 to 3.2 [3].

One possible theory to explain the observed features in the all-particle energy spectrum is that, if the energy spectra of individual galactic cosmic ray elements are described by a power law with a cut-off at a given energy, then the "knee" of the all-particle spectrum may be explained as the start of the sequential cut-offs of each elemental nucleus [8]. This model also goes some way to explain the existence of the "second knee" and "ankle" as the end of the sequence of cut-offs of stable and all remaining galactic source cosmic ray nuclei respectively. While measurements of the secondary particle components at ground level agree with this model, experiments measuring the mass composition by the position of shower maximum (X_{max}) do not [9].

Following the discovery of the cosmic microwave background (CMB) in 1965 [10], Greisen [11], Zatsepin and Kuzmin [12] theorised that extremely high energy cosmic rays would interact with this background thereby losing energy. The result of this would be an eventual suppression of the flux of cosmic rays detected, called the GZK cut-off, and is expected to occur above around 6×10^{19} eV.

Modern experiments such as the Pierre Auger Observatory focus on investigating these highest energy cosmic rays (above 10^{18} eV), known as ultra-high energy cosmic rays, or UHECRs. Since the flux at such high energies is of the order of one per km^2 per year, in order to detect UHECRs reliably at significant rates, the detectors must span vast areas. One of the purposes of such experiments has been to determine the presence or absence of a GZK cut-off. Figure 1.1.2 shows the UHECR energy spectrum as measured at the Pierre Auger Observatory (described in detail in Chapter 3) above 10^{18} eV as reported in 2011 [13].

1.2 Composition

The composition of cosmic rays at low energies (below around 10^{15} eV) is well known from direct measurements. Figure 1.2.1 shows a comparison between the relative abundances of galactic cosmic rays and solar system material normalised to Si at 1 TeV [14]. It can clearly be seen in this Figure that, while the two abundances are similar, there are two main regions in which the cosmic ray abundances differ significantly from those of the solar system material.

Both the solar system and cosmic ray abundances show the same odd/even trend where the even atomic numbered elements (i.e. the more tightly bound nuclei) are the more abundant. However, the cosmic ray abundances for elements Li, Be and B as well as Sc, Ti, V, Cr and Mn are significantly higher than those of the solar

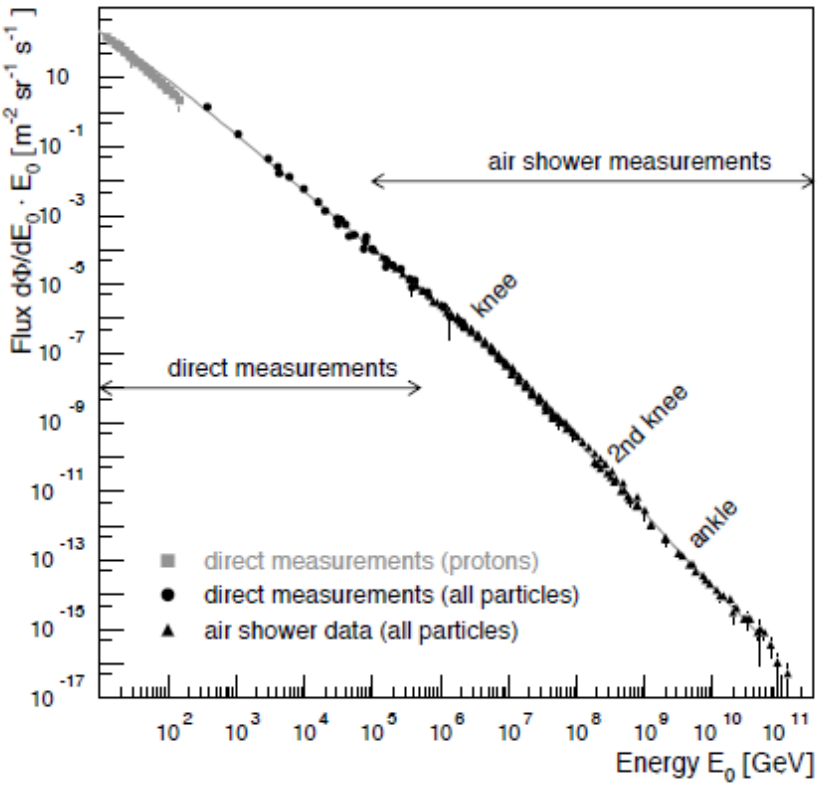

Figure 1.1.1: The differential all-particle cosmic ray energy spectrum showing the "knee" at around 10^{15} eV and the "ankle" at around 10^{19} eV [3].

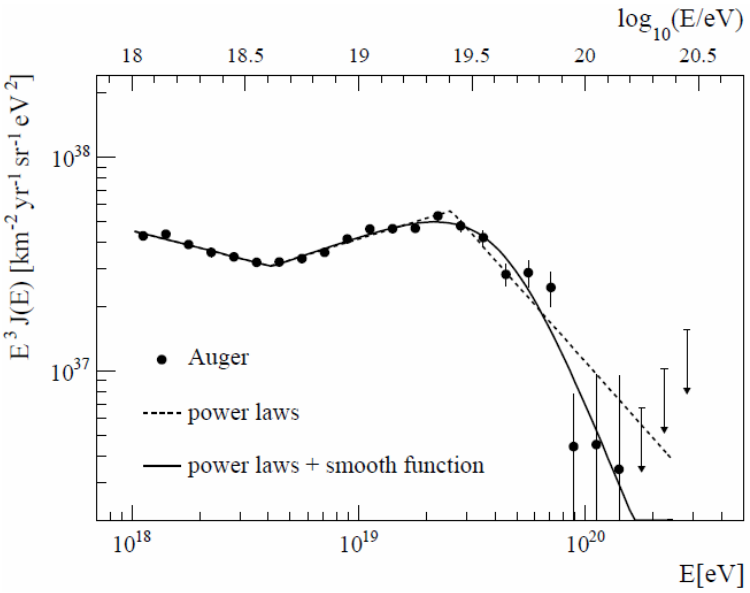

Figure 1.1.2: The published results from the Pierre Auger Observatory in 2011. Note that at these very high energies, the results are very limited by the extremely low statistics [13].

system material. The reason for this is that these elements are not produced as end products of stellar nucleosynthesis and so are not present in significant quantities in the solar system material whereas they may be produced as spallation products in cosmic ray collisions. In particular, Li, Be and B are spallation products of carbon and oxygen while Sc, Ti, V, Cr and Mn are spallation products of iron [14].

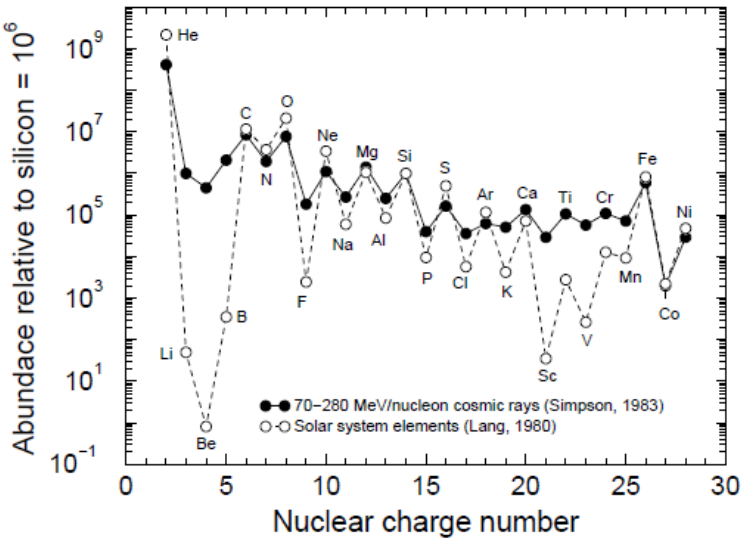

Figure 1.2.1: The relative abundances of galactic cosmic rays and solar system material normalised to Si= 10^6 [14].

Above around 10^{15} eV, direct measurements of the primary cosmic ray particles are no longer feasible and the properties of the primary particle must be deduced from EAS measurements. Such measurements cannot provide an exact determination of the cosmic ray composition, relying instead on reconstructions based on theoretical models. Since there is currently no way to experimentally verify the validity of these models at such high energies using particle accelerators, all results from these reconstructions must be treated with some caution.

The galactic cosmic ray flux composition as a function of energy is generally considered as resulting from a "bottom-up" model of cosmic ray production. If it is assumed that an accelerated cosmic ray particle is magnetically confined within a source region, then it may be expected that the maximum attainable energy of the particle (with charge Z) will be approximately Z multiplied by the maximum energy of a proton. This leads to the expectation that the average mass of the galactic cosmic ray flux would increase with increasing energy, as the maximum energy of each species is passed sequentially. However, once the extragalactic cosmic ray flux begins to dominate, the composition would then be expected to transition back to the lighter nuclei [8, 3].

In the region between the knee and ankle ($10^{15} - 10^{19}$ eV), composition measurements are consistent with this model, showing a decrease in the abundance of the lighter elements with increasing energy. Measurements of the spectra also show that the cut-off energy for each species appears to be proportional to its charge, which is consistent with a rigidity dependence on either the acceleration limits of the source or with a confinement of the cosmic rays within the Galactic magnetic field [15, 16].

Above the ankle ($\sim 10^{19}$ eV), the cosmic ray flux is expected to have transitioned from galactic to extragalactic origin [17]. In this region it is expected that the primary cosmic ray flux will contain a mix of predominantly protons and iron, since the particles with intermediate masses are expected to disintegrate during propagation and hence not arrive at the Earth in great quantities [3].

1.3 Origins and Acceleration Mechanisms

As described in Section 1.1, it is believed that the cosmic rays with energy below the "knee" (that is around 10^{15} eV) originate from galactic sources while those above the ankle may originate from extra-galactic sources. This section aims to describe possible acceleration mechanisms and sources.

The main problem with identifying cosmic ray sources is that, being primarily charged particles, cosmic rays are deflected by the various magnetic fields permeating the interstellar and intergalactic space. Consequently, for all but the highest energies, a cosmic ray's arrival direction will bear little resemblance to its actual source direction. What can be studied instead is the overall directionality of these particles, or their deviation from an isotropic flux. A description of the study of cosmic ray anisotropies is given in Chapter 4.

Galactic cosmic rays are generally considered to be accelerated in sites such as supernova remnants via the process of diffusive shock acceleration [18]. If, as described in Section 1.2, we consider cosmic rays to be confined within their acceleration region, the maximum attainable energy for a particle with charge Z will be approximately proportional to Z. This relationship is also dependent upon the size R (kpc) of the acceleration region as well as the magnetic field strength B (μG) such that the maximum attainable energy E_{max} becomes:

$$E_{max} \approx 10^{18}\text{eV} Z \beta_s \left(\frac{R}{\text{kpc}}\right)\left(\frac{B}{\mu\text{G}}\right) \tag{1.3.1}$$

where β_s is the shock velocity in units of c [3].

Hillas extended this acceleration model to cosmic rays of extragalactic origin and devised a diagram, similar to that shown in Figure 1.3.1, in which he plotted various astrophysical objects as a function of their size and magnetic field strength,

in comparison to the values predicted from Equation 1.3.1 required to accelerate protons and iron to 10^{20} eV. It is clear from this diagram that there are very few known objects capable of accelerating particles to these extreme energies.

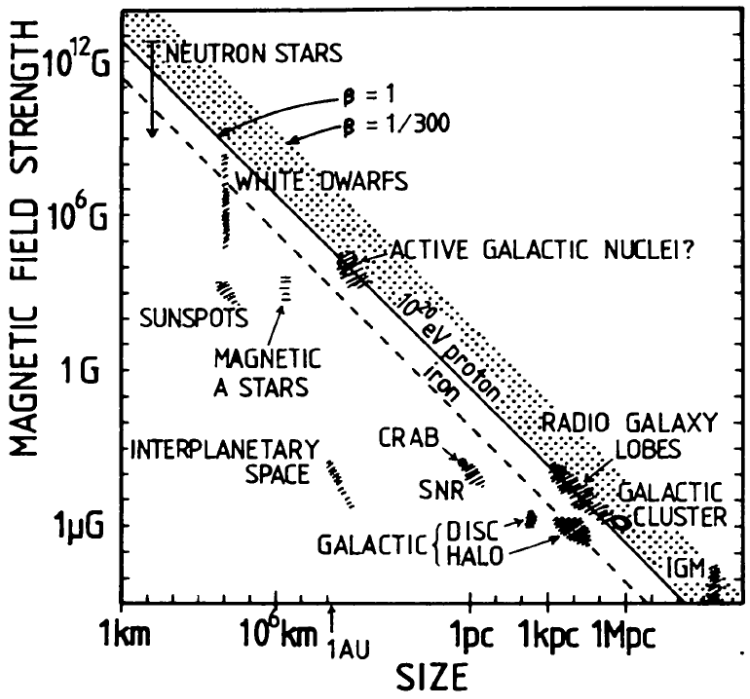

Figure 1.3.1: A reproduction of the diagram produced by Hillas showing candidate astrophysical sources plotted as a function of their size and magnetic field strength. The diagonal lines represent the size and magnetic field strength calculated to be capable of accelerating iron and protons to 100 EeV (10^{20} eV) [19].

1.4 Extensive Air Showers

An extensive air shower (EAS) is initiated when an incoming high energy cosmic ray particle (primary particle) reaches the top of the Earth's atmosphere and interacts with an air molecule in the atmosphere. The secondary particles produced during this interaction go on to further interact with other molecules in the atmosphere, producing a cascade of secondary particles along the axis of the primary particle's motion. The leading edge of this cascade (known as the shower front) is a thin disc-like structure which travels along the shower axis at near the speed of light, and spreads out laterally as a result of the particle interactions and Coulomb scattering. The number of cascade particles (shower size) increases rapidly following the initial interaction and continues to increase until a critical point is reached at which individual particle energies become too low for further particle production to occur, and

the rate of secondary particles being created drops below the rate of energy loss to the surrounding environment [20].

The longitudinal development of an EAS is dependent on the local atmospheric density and, consequently, the development of an EAS is generally measured in a unit which takes into account both atmospheric density and length. The atmospheric depth of a shower X (g.cm^2) is the integral of the atmospheric density between a height h and the top of the atmosphere (taken to be infinite) along the axis of shower propagation:

$$X = \int_h^\infty \rho(l).dl \tag{1.4.1}$$

The point at which the maximum shower size (shower maximum) is reached can then be expressed at an atmospheric depth, the depth of shower maximum X_{max}. In general, the size of a shower can be described as a function of atmospheric depth using a parameterisation of the average longitudinal development known as the Gaisser-Hillas profile [21, 22, 23]:

$$N_e(X) = N_e^{max} \left(\frac{X - X_0}{X_{max} - X_0} \right)^{\frac{X_{max} - X_0}{\lambda}} e^{-\frac{X - X_{max}}{\lambda}} \tag{1.4.2}$$

where X_0 and λ are shape parameters and N_e^{max} is the number of electrons at X_{max}.

An EAS can generally be considered to consist of three main components: a hadronic core as well as an electromagnetic and a muonic component. Each of the components are described below and depicted in Figure 1.4.1. The density of secondary particles decreases with lateral distance from the shower core with the spreading being dominated by Coulomb scattering of the electromagnetic component and the production angles of the muon component. The scale of this lateral spread of the electromagnetic component can be characterised by the Molière radius r_M which, for low energy electrons at sea level, is approximately 80 m [20].

1.4.1 Hadronic Core

The hadronic core begins with the initial interaction between a hadronic cosmic ray particle and the molecules in the atmosphere. The majority of particles produced in this interaction are pions with the addition of some kaons and heavier hadrons. The decay of these pions feeds the other components of the shower. That is, neutral pions decay into γ-ray photons and feed the electromagnetic component while the

charged pions decay into muons and neutrinos.

$$\begin{aligned} \pi^+ &\rightarrow \mu^+ + \nu_\mu \\ \pi^- &\rightarrow \mu^- + \bar{\nu}_\mu \\ \pi^0 &\rightarrow 2\gamma \end{aligned} \tag{1.4.3}$$

As a result of their very small interaction cross-section, neutrinos do not contribute any further to shower development. Kaons may either interact or decay producing more pions, muons, electrons or neutrinos. The remnants of the primary cosmic ray particle continue down through the atmosphere further interacting with atmospheric nuclei and so, although the hadronic core makes up only a very small part of the total shower, it provides a continuous feed of energy and particles into the other two components.

The hadronic core has only very small lateral spread from the shower axis (direction of shower propagation) with the majority of those particles reaching ground level being found within only a few metres of the shower core.

1.4.2 Electromagnetic Component

The electromagnetic component is by far the largest component of an EAS, containing around 90% of the particles[3]. It is initiated by the γ-ray photons produced by the decay of neutral pions. If the energy of these photons is above 1.02 MeV, then pair production may occur whereby a γ-ray photon decays into an electron positron pair in the field of an atmospheric nucleus N:

$$\gamma + N \rightarrow e^+ + e^- + N \tag{1.4.4}$$

These electrons and positrons may then produce further γ-ray photons via the process of Bremsstrahlung:

$$e + N \rightarrow e + N + \gamma \tag{1.4.5}$$

which can in turn undergo pair production again provided they are of sufficient energy.

This repeating cycle of pair production and Bremsstrahlung continues in a cascading process, increasing the number of particles, until the rate at which particles are created falls below the rate at which they are lost due to ionisation processes. For electrons and positrons, this happens at a critical energy E_{crit} ~80 MeV. For the γ-ray photons, E_{crit} ~20 MeV below which Coulomb scattering, then photoelectric absorption, progressively take over from pair production [24].

Heitler modeled the electromagnetic cascade development in 1938 by the following method [24]. He assumed that a γ-ray photon would interact in the atmosphere after

traveling a distance λ_{em} and produce two new particles each with half the energy of the initial particle. These two new particles would then interact at a distance λ_{em} from their production point. This would continue and so, after n generations, the shower would contain $2n$ particles. This could then be expressed as a function of depth X:

$$N(X) = 2^{X/\lambda_{em}} \tag{1.4.6}$$

Continuing this process until the energy of the secondary processes fell below the critical energy for further particle production, this then gives the number of particles at shower maximum to be:

$$N_{max} = E_0/E_{crit} \tag{1.4.7}$$

where E_0 is the energy of the primary γ-ray photon. The depth of shower maximum in this scenario would then be:

$$X_{max} = \lambda_{em}.\log_2\left(\frac{E_0}{E_{crit}}\right) \tag{1.4.8}$$

While this model is an oversimplification of the electromagnetic cascade process, it clearly highlights two main features of the shower development. These are, that the number of particles at shower maximum is directly proportional to the energy of the primary particle, and that the depth of shower maximum increases logarithmically with the energy of the primary particle. These relationships are often used to crudely approximate those of all cosmic ray showers[24, 25].

1.4.3 Muonic Component

The muonic component of an EAS is primarily produced by the decay of charged pions and kaons. The half-life of a muon is only around 2.2 x 10^{-6} s in its rest frame. However, because of relativistic time dilation, those muons produced with a Lorenz factor above around 20 are able to survive until sea-level. The less energetic muons decay in flight producing electrons or positrons, adding to the electromagnetic component.

$$\begin{aligned} \mu^+ &\rightarrow e^+ + \nu_e + \bar{\nu}_\mu \\ \mu^- &\rightarrow e^- + \nu_\mu + \bar{\nu}_e \end{aligned} \tag{1.4.9}$$

The dominant energy loss mechanism for muons is ionisation with a loss rate of around 2 MeV per g.cm^{-2} of atmosphere [20]. This leads to an attenuation length of around 1,000 g.cm^{-2}, which is around 5 times that of the electromagnetic component. Consequently, for low energy showers, often the muonic component is the only part of the shower to reach ground level. These are known as unaccompanied muons and

make up the vast majority of the background flux at sea level, with a particle density of around 1 particle per cm^2 per minute.

Since the muon attenuation length is approximately the thickness of the atmosphere, it follows that the muon flux at sea level is effectively a measure of the integral of the muon production over the lifetime of the shower.

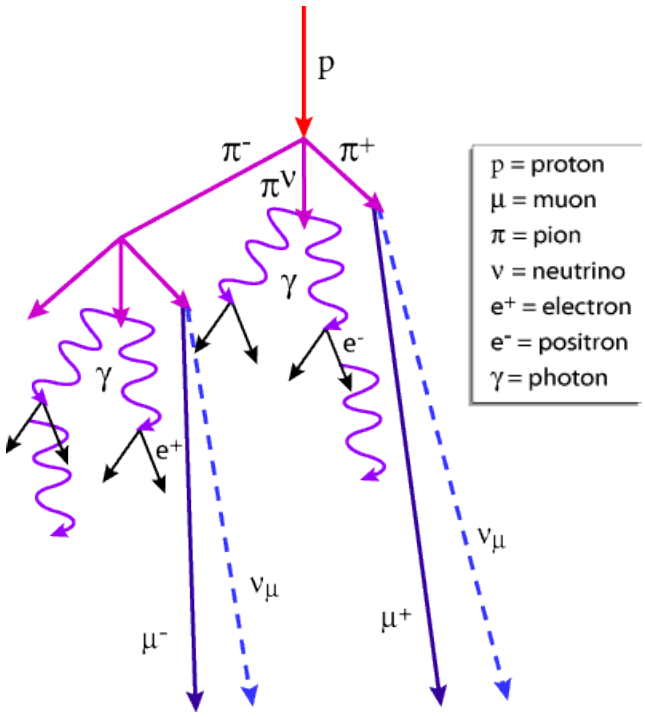

Figure 1.4.1: Example of cosmic ray primary particle interactions with atmospheric nuclei and the development of an extensive air shower. (taken from `http://www.hawc-observatory.org/science/cosmicrays.php`)

2: Extensive Air Shower Detection Methods and Experiments

As discussed in Section 1.1, it is impractical to directly measure cosmic rays above energies of around 10^{15} eV. Instead, various methods have been developed to measure the properties of the extensive air showers (EAS) produced as cosmic ray particles interact with the Earth's atmosphere. This chapter is divided into three main sections: the first describes some of the methods of extensive air shower detection, while the second section describes some of the historical cosmic ray experiments. The third section describes some of the more contemporary experiments, the results from which bear particular interest to the work presented in this thesis. The Pierre Auger Observatory is not discussed here but is described in detail in Chapter 3.

2.1 Detection Methods

Ground arrays have traditionally been the most common detectors of EAS. However, fluorescence detectors have become increasingly recognised as an important tool in cosmic ray research. These two detection methods are described below as well as methods utilising the detection of Cherenkov light and radio emission from EAS.

2.1.1 Ground Arrays

Ground arrays are typically a sparse array of either scintillator slabs or water-Cherenkov stations that measure the density of shower particles at ground level. The relative timing of the signals in each element of an array can be used to determine the orientation of the shower front. The shower direction, and hence the primary cosmic ray particle arrival direction, is then perpendicular to this shower front close to the shower core. In general, the timing resolution of ground arrays is of the order of a few nano-seconds.

The measurements of the shower densities at each array element are used to fit an appropriate lateral distribution function (LDF) which is described in more detail in Section 1.4. This fitted LDF is then used to determine the total number of shower particles and the position of the shower core. The energy and composition

of the primary particle must then be inferred indirectly from these reconstructed parameters.

The primary cosmic ray energy E_0 is most commonly estimated using the number of electrons and muons measured at ground level by relationships such as [26]:

$$\begin{aligned} E_0 &= 3.01 \text{ GeV}.A^{0.04}.N_e^{0.96} \\ E_0 &= 20 \text{ GeV}.A^{-0.11}.N_\mu^{1.11} \end{aligned} \tag{2.1.1}$$

where $N_e$and N_μ are the numbers of electrons and muons in the shower respectively and A is the mass number of the primary particle. From these relationships, it can be seen that an energy estimator is obtained that is almost independent on the mass of the primary particle.

The number of electrons and muons measured at ground level are also used to estimate the mass of the primary cosmic ray particle. Showers which develop higher in the atmosphere (heavier nuclei) will have a greater number of particles absorbed before reaching ground level. Conversely, more charged pion decays are likely to have occurred, thus producing a greater number of muons. That is, the electron to muon ratio may be used as an indicator of the height at which a shower develops and hence provide information about the mass composition of the primary particle. A Heitler model of hadronic showers gives the following relationship [26][15]:

$$\frac{N_e}{N_\mu} \approx 35.1 \left(\frac{E_0}{A.1 \text{ PeV}} \right)^{0.15} \tag{2.1.2}$$

There are systematic uncertainties in these estimations due to attenuation as showers with higher zenith angles have passed through a greater amount of atmosphere before reaching ground level than those with low zenith angles. These uncertainties are strongly dependent on the shower modeling.

Different types of ground array are sensitive to different components of an EAS. Scintillator arrays are most sensitive to the electromagnetic component of a shower whereas water-Cherenkov stations have a greater sensitivity to the muonic component. The sensitivity of scintillation detectors to other components of an EAS may be improved by the addition of shielding to reduce the signal produced by the electromagnetic component..

Water-Cherenkov stations detect cosmic ray particles by measuring the Cherenkov radiation they emit as they pass through the water in the station. The water tanks are considerably deeper than scintillator slabs, having a depth of around 1 m compared with only a few cm. This depth improves their response to showers with large zenith angles when compared to scintillators. This means that an array of water-Cherenkov stations has a greater sky coverage than a scintillator array of the same

size.

In general, ground arrays are mostly independent of atmospheric weather conditions and can be run continuously. This means that they have a fairly constant exposure in right ascension.

2.1.2 Fluorescence Detection

Fluorescence detectors have become increasingly favoured as a detection technique for air showers originating from high energy cosmic rays (above 10^{17} eV). They consist of grids of photomultipliers constituting cameras that view the sky and measure the fluorescence light emitted as nitrogen molecules in the atmosphere are excited by the charged particles of an EAS. The amount of light produced is close to proportional to the energy of the primary cosmic ray and so fluorescence detectors can perform calorimetric measurements of the energy deposited in the atmosphere by an EAS. They also have the advantage of being able to directly measure the longitudinal development profile of a shower. The light track image seen from a single fluorescence detector telescope gives the "shower-detector" plane. The orientation of the shower within this plane is then determined from the timing sequence of each of the signals making up the track. The angular uncertainty in this shower axis then depends on the resolution of the fluorescence camera as well as the length of the track image and the incident direction of the shower.

The accuracy of shower reconstruction is improved significantly by using a second fluorescence detector and operating the two together in stereo. Since fluorescence light is emitted isotropically, it is possible to view the same shower from two different angles. The shower axis can then be resolved as the intersection of the two shower detector planes. This can improve the accuracy of the reconstructed shower axis from around only 4.5° for a monocular configuration to around 0.6° for stereo configurations [3].

Because they can directly measure the longitudinal profile of an EAS, fluorescence detectors can estimate the mass composition of the primary cosmic ray particle in a different manner to ground arrays. Cosmic ray air showers develop quite differently depending on the composition of the primary particle and the depth at which shower maximum X_{max} occurs is commonly used as a composition estimator. This is dependent on the mass of the primary particle by the following relationship [26]:

$$X^A_{max} = X^p_{max} - X_0 \ln A \tag{2.1.3}$$

where A is the mass of the primary cosmic ray particle and X^p_{max} is the depth of shower maximum in g.cm^{-2} for a proton induced shower.

Unlike ground arrays that run continuously, fluorescence detectors can only be

operated on dark, moonless, nights. This restricts them to a duty cycle of around only 10%. Fluorescence detection is also strongly weather dependent with the fluorescence yield depending on the gas mixture of the atmosphere in addition to other atmospheric conditions.

Other modern detectors, such as the Pierre Auger Observatory, are hybrid detectors using a combination of ground array and fluorescence detection techniques to maximise the benefits of both in the study of the highest energy cosmic rays.

2.1.3 Cherenkov Light Detection

The particles in an EAS travel through the atmosphere at relativistic speeds. Those charged particles with sufficient energy (above 21 MeV at sea-level for electrons and positrons) may emit Cherenkov radiation. This light is radiated in the forward direction in a cone with an opening angle of around 1.3° at sea-level [3].

There are two main techniques for detecting this Cherenkov light at ground level. The first is the use of integrating detectors which consist of arrays of photomultipliers inside light collecting cones (Winston cones) looking upwards. The second is the use of imaging detectors such as H.E.S.S. [27] which consist of large area collection mirrors and photomultiplier cameras with segmented readout.

Like fluorescence detectors, Cherenkov light detectors can only be operated on dark, moonless, nights and so also have a duty cycle of around only 10%.

2.1.4 Radio Emission Detection

Coherent radio emission from EAS was first theoretically predicted in 1961 by Askaryan [28]. In 1965 it was experimentally verified by Jelley at a frequency of 44 MHz [29]. Early studies into radio emission met with limited success. Modern experiments aim to continue these studies using modern techniques. It is currently understood that there are two competing mechanisms for radio emission. The first is the coherent Cherenkov radiation of charge excess in the shower, which is stronger in dense media. The second is geosychrotron radiation from charged particles being deflected in the Earth's magnetic field. Further study is ongoing to understand the interrelation between these two mechanisms [3].

2.2 Pioneering Experiments

2.2.1 Haverah Park

The Haverah Park array was in operation for 25 years from 1962 to 1987. It was located near Leeds University in the United Kingdom (54°N, 1.6°W) and was one of the earliest experiments to use the water-Cherenkov tank cosmic ray detection

technique. Each water-Cherenkov tank had an area of 2.29 m^2 and was 1.2 m deep [30]. The Cherenkov light produced as charged particles passed through the water in each tank was collected by a single 5" photomultiplier tube. Detector elements were formed by grouping these stations together to form large detection areas that were able to detect relatively small secondary particle fluxes.

In the centre of the array, four detector huts named A1 to A4 were used for triggering the rest of the detector. Each hut contained 16 water-Cherenkov stations as shown in Figure 2.2.1 C). The use of 15 of these stations gave a total collecting area of 34 $m^2$for each hut [31]. The charge produced in a hut by the passage of a vertical equivalent muon (VEM) was used to calibrate the signals between the huts. In order to trigger, the signal in hut A1 and at least two of hut A2, 3 and 4 had to exceed 0.3 VEM/m^2 [32]. The orientation and relative heights of the "A" detector huts are shown in Figure 2.2.1 B).

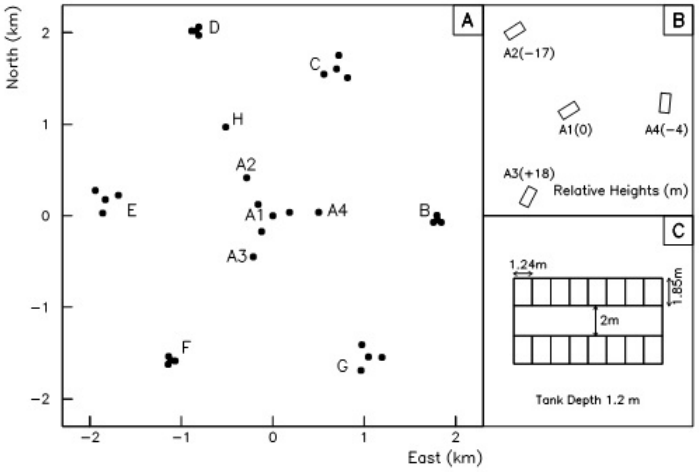

Figure 2.2.1: The layout of the Haverah Park cosmic ray detector displaying A) the whole array, B) the orientation and relative heights of each of the four central detector huts A1 to A4, and C) the layout of the water-Cherenkov stations within one of the main detector huts [32].

Six groups of stations were spaced around the central "A" huts to help constrain the core position in large showers. Also, an infill of thirty small 1 m^2 stations with a spacing of 150 m was in operation for several years in the space between the "A" stations.[30] The layout of the whole Haverah Park experiment prior to the infill is shown in Figure 2.2.1 A).

2.2.2 Volcano Ranch

Volcano Ranch was constructed by Linsley, Scarsi and Rossi and operated from 1959 until 1963 [33]. During this time it measured one of the highest ever recorded cosmic

ray events, with a reconstructed primary energy above 10^{20} eV [5]. It was the first of the giant ground arrays and was located at Volcano Ranch, near Albuquerque in New Mexico.

The Volcano Ranch experiment consisted of nineteen 3.3 m^2 plastic scintillation counters spaced out in an array that covered and area of 8.1 km^2. The layout of the array is shown in Figure 2.2.2 along with the relative signals as seen by each detector unit during the extremely high energy event. Each unit was viewed with a 5" photomultiplier and measurements made of the pulse amplitudes and relative arrival time of each signal. An additional 3.3 m^2 unit was shielded by 10 cm of lead in order to measure the muon density for muons with energy greater than 220 MeV.

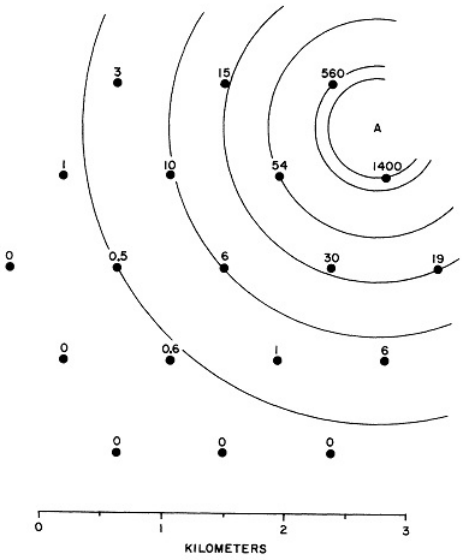

Figure 2.2.2: The layout of the Volcano Ranch array showing the signal measured (particles/m^2) at each detector unit for the event above 10^{20} eV as well as its estimated core location [5].

Measurements made at Volcano Ranch provided the first measurements of the cosmic ray energy spectrum above 10^{18} eV and hinted at the presence of the flattening of the spectrum now known as the "ankle" (see Section 1.1). It was also the first experiment to investigate the arrival direction distribution of cosmic ray events above 10^{18} eV [33].

2.2.3 Yakutsk

The Yakutsk cosmic ray detector in Siberia (61.7°N, 129.4°S) is currently one of the longest running cosmic ray experiments, operating continuously since 1970.

It consists of three nested scintillator arrays. The central array is a small hexagonal array of scintillation counters spaced at 62 m and covering an area of 0.026 km^2.

Each scintillation counter in this array has an area of only 0.25 m^2. This central array is surrounded by two more widely spaced triangular arrays of 2 m^2 scintillation counters with spacings of 500 m and 1 km. Prior to 1990, the configuration of these two triangular arrays was such that there were 19 counters at 500 m spacing and 29 counters at the 1 km spacing. The triggering for these arrays required all three counters on the corner of a triangle to fire in coincidence. This gave 24 triggering triangles with a total area of 2.5 km^2 in the 500 m array and 40 triangles in the 1 km array covering 16 km^2. This configuration was rearranged between 1990 and 1992 adding 18 counters to the 500 m array and removing 10 counters from the 1 km array [32].

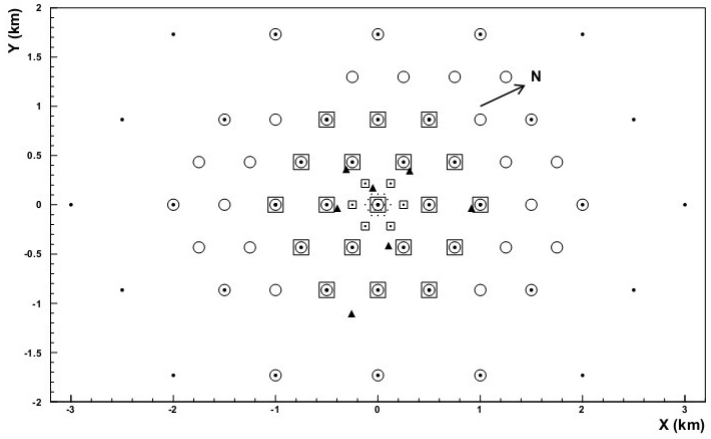

Figure 2.2.3: The layout of the Yakutsk cosmic ray detector [32].

In addition, the Yakutsk experiment also contains an array of air Cherenkov detectors consisting of large photomultipliers collecting Cherenkov light from air showers directly. These photomultipliers have areas of 176 cm^2 and 530 cm^2.

2.2.4 Fly's Eye

The Fly's Eye detector in Utah was the first working fluorescence detector. It consisted of two sites: Fly's Eye I and Fly's Eye II. Fly's Eye I began operation in 1981 at the Dugway Proving Grounds (40.2°N, 112.8°S) and consisted of 67 x 1.5 m spherical mirrors collecting fluorescence light. Each mirror had 12 or 14 photomultipliers at its focus and each of these 880 photomultiplier tubes viewed a hexagonal region of the sky around 5.5° in diameter. This gave Fly's Eye I full sky coverage [34][35]. The arrangement of these hexagonal pixels is shown in Figure 2.2.4 as a projection onto the dome of the sky. A cosmic ray event appears as a track across the sky and is shown superimposed on the projection [32].

The second site, Fly's Eye II, started full operation in 1986 and was situated

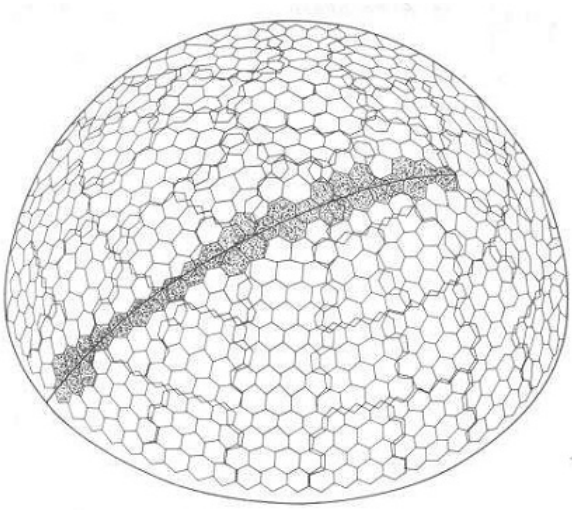

Figure 2.2.4: The arrangement of Fly's Eye I pixels as projected onto the dome of the sky. The track of an event is superimposed [32].

34 km away from Fly's Eye I.[34] It consisted of 36 mirrors of the same design as the first site with a total of 464 photomultiplier tubes. It only viewed half the sky but had full elevation coverage. The two sites could be operated independently or together in stereo. They continued operation until 1992.

2.2.5 HiRes prototype (CASA-MIA hybrid)

The High Resolution Fly's Eye (HiRes) prototype was developed using the experience and knowledge of the Fly's Eye experiment and was developed as a test of concept before the full HiRes experiment (described in Section 2.2.6). The HiRes prototype 1 was constructed in 1991 at the location of the original Fly's Eye I detector (see Section 2.2.4). Initially containing only two mirrors, these were oriented to overlook the Fly's Eye II site and the CASA-MIA (Chicago Air Shower Array - Michigan Muon Array) ground array. It commenced full operation in August 1993 and contained 14 mirrors arranged in 5 elevation bands. These covered elevation angles between 3° to 70° overlooking CASA-MIA [36]. The fields of view of the HiRes 1 prototype are shown in the right panel of Figure 2.2.5.

The HiRes prototype 2 began operation in September 1994 and was located 12.6 km to the southwest. It contained only 4 mirrors and these were oriented in elevation bands to overlap the fields of view of the HiRes 1 prototype and also overlooked CASA-MIA [36].

CASA-MIA was a multi-component EAS array. The CASA component consisted of an array of 1089 surface scintillators for the detection of the electromagnetic component, while the MIA component comprised 1024 scintillators (grouped into 16

patches) buried 3 metres below ground for the detection of the muonic component [32]. In total the CASA-MIA array covered an area of 0.23 km^2, with the layout shown in the left panel of Figure 2.2.5.

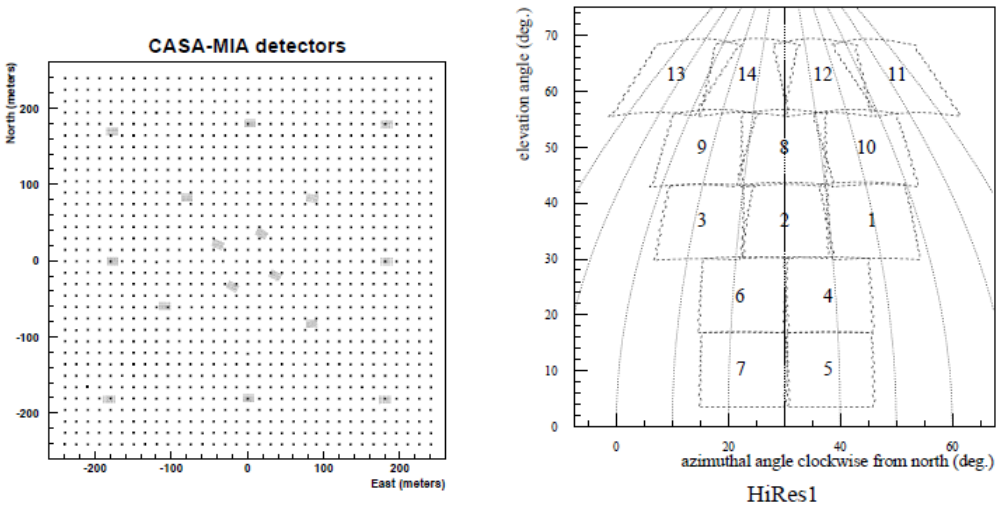

Figure 2.2.5: Layout of the CASA-MIA ground array (left) and the field of view of the 14 HiRes 1 prototype mirrors (right).[32][36]

The experiment involved some fortuitous timing as the CASA-MIA ground array was nearing decommission [32]. However, this allowed the HiRes prototype to be the first cosmic ray detector to combine the use of both fluorescence and ground array detection techniques. The HiRes prototype ceased operation in November 1996 [36] but paved the way for future hybrid experiments such as the Pierre Auger Observatory.

2.2.6 HiRes

The experience gained from the Fly's Eye and HiRes prototype (see Sections 2.2.4 and 2.2.5) led to the design and development of the High Resolution Fly's Eye (HiRes) experiment. Like its predecessors, it was located at the Dugway Proving Grounds in Utah. The experiment operated from May 1997 until April 2006 and investigated cosmic ray air shower events in the energy range 10^{18} to 10^{21} eV. This increased energy range required the detector to be able to see much more distant showers; up to 60 km away [37]. To achieve this, the mirror size of each telescope was increased to a 4 m^2 effective area. Each mirror was viewed by a 256 pixel camera located at the focal plane that was instrumented with a 16x16 array of hexagonal photomultiplier tubes. Each pixel viewed an approximately 1° region of sky.

The HiRes experiment was located at two sites separated by 13 km. HiRes I was located on the same hill as the original Fly's Eye I and operated alone until the end of

1999. It contained 22 telescope mirrors in a single ring that covered elevation angles between 3° and 17°. HiRes II began operation in December 1999 and contained 42 mirrors arranged in two rings that viewed elevation angles from 3° to 31° [38]. The arrangement of the mirrors in HiRes I and HiRes II are shown in Figure 2.2.6.

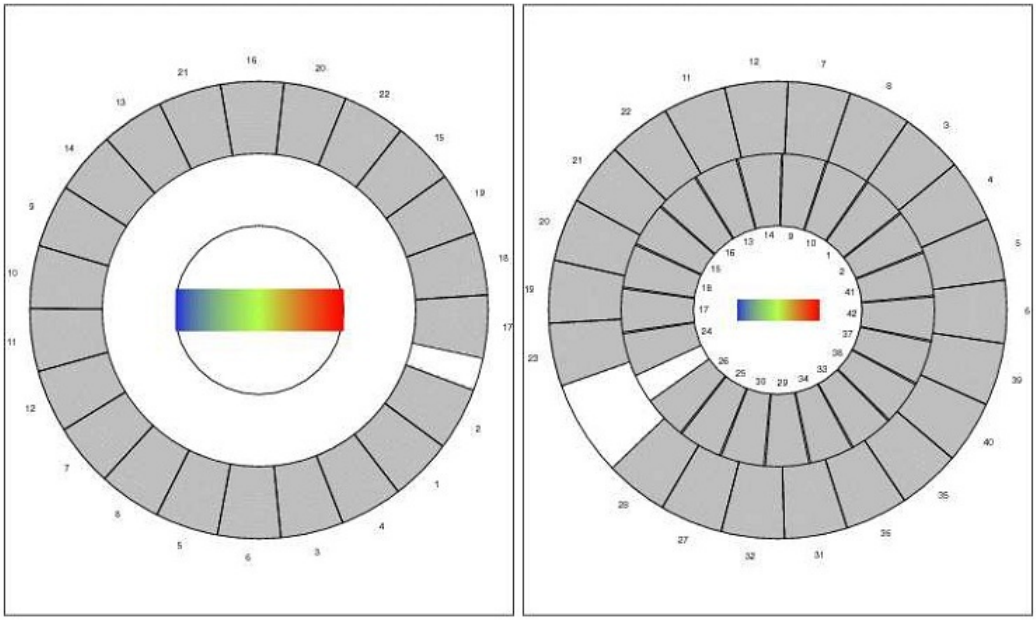

Figure 2.2.6: Configuration of the mirrors HiRes I (left) and HiRes II (right). The outer ring covers elevation angles between 3° and 17° while the inner ring covers 17° to 31° [32].

The HiRes fluorescence detector design has been incorporated into the design of the Telescope Array (described in Section 2.3.5).

2.2.7 SUGAR

The Sydney University Giant Air-shower Recorder (SUGAR) was the first of the major high energy cosmic ray experiments to be situated in the southern hemisphere. It was situated at 30.5°S, 149.61°E and operated from 1968 until 1979. SUGAR consisted of a 1600 m square grid with 50 spacing of pairs of buried liquid scintillator tank, each operating autonomously with an effective area of 6.0 m^2 [32, 39]. The layout of the SUGAR array is shown in Figure 2.2.7.

2.2.8 AGASA

The Akeno Giant Air Shower Array (AGASA) grew from the Akeno 1 km^2 array [40] located near the Akeno Observatory in Japan at 35.8° N, 138.5° E. It was a very large ground array covering a total area of around 100 km^2 with a square grid of 111

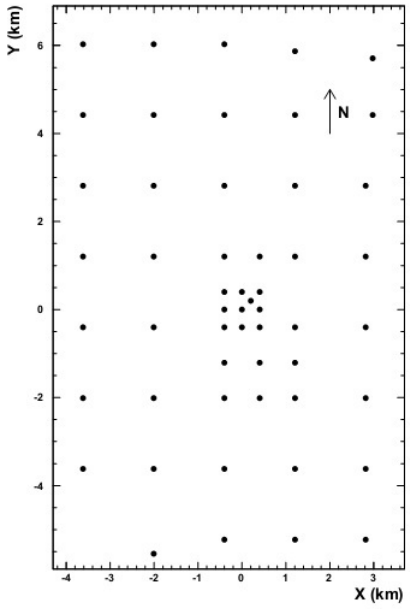

Figure 2.2.7: The layout of the SUGAR array [32].

scintillation counters, each with a 2.2 m^2 area. Figure 2.2.8 shows the configuration of the scintillator array. Operating from the mid 1980s until 2004, it was the first cosmic ray detector to have significant exposure in the region of the theorised GZK cutoff (at $\sim 6 \times 10^{19}$ eV).

2.2.9 EAS-TOP

EAS-TOP was a multi-component Extensive Air Shower array located at Campo Imperatore, on top of the underground Gran Sasso Laboratory in central Italy, at an altitude of 2005 m above sea level. It was designed to detect the secondary particles originating from primary energies between $10^{13} - 10^{16}$ eV (spanning the "knee" of the cosmic ray energy spectrum, see Section 1.1), and was in operation between 1989 and 2000. It is comprised several detectors tuned to the detection of different EAS components [42, 43, 44]:

- a surface array of 35 scintillator modules to detect the electromagnetic component, with a triggering system that required the coincidence of four neighbouring modules and resulted in an event rate of ≈ 25 Hz,
- a 1000 g/cm^3 thick calorimeter made of lead and iron, and viewed by streamer tubes operating in either limited streamer mode (for μ tracking) or quasi-proportional mode (for hadron calorimetry),

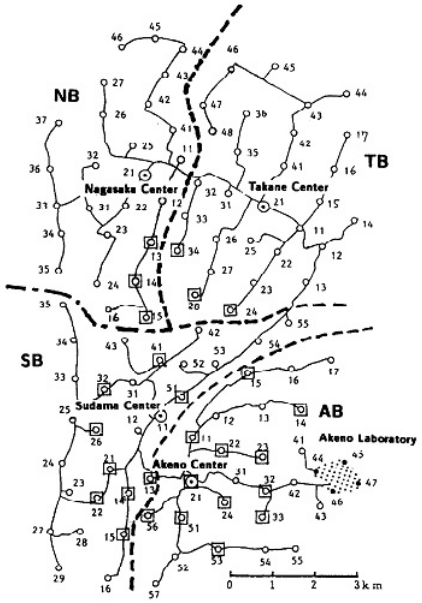

Figure 2.2.8: The layout of the AGASA experiment. Open circles and squares represent the surface detectors and shielded detectors respectively. The solid lines show the optical fibre routes of AGASA's data communication network [41].

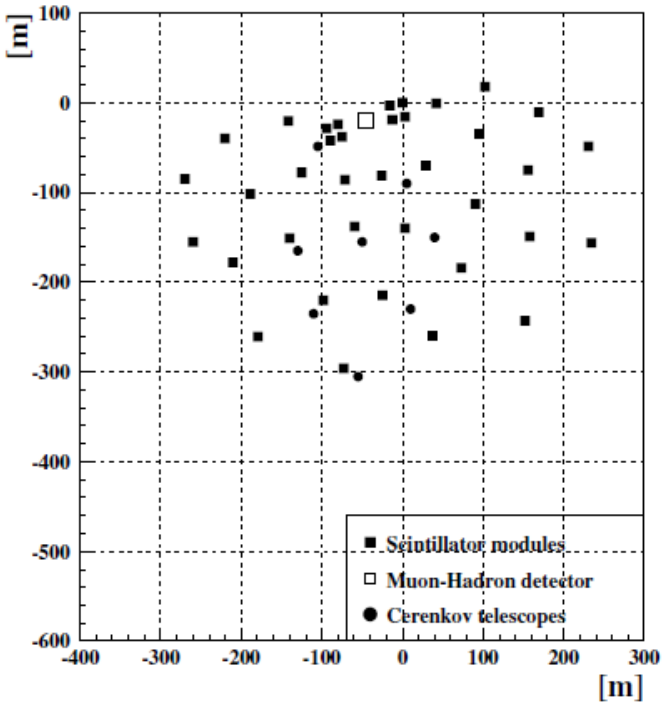

Figure 2.2.9: The layout of the EAS-TOP experiment, showing the 35 scintillator modules for the detection of the electromagnetic component, the muon-hadron detector as well as the 8 Cherenkov light telescopes [42].

- a Cherenkov light detector comprising 8 steerable telescopes enclosed in remote controlled domes, located about 60 m apart, as well as
- three radio antennas for detection of EAS radio emission. with a triggering system that required the coincidence of four neighbouring modules and resulted in an event rate of ≈ 25 Hz.

2.2.10 Nagoya

Muon telescopes, such as the Multi-Directional Cosmic-Ray Muon Telescope at Nagoya, span still lower cosmic ray energies. The Nagoya muon telescope was constructed during the late 1960's with continuous observation of cosmic ray intensities begun in October 1970. The telescope is located in Nagoya (Japan) at 35º N, 137º E at an altitude of 77 metres above sea level and detects cosmic rays with a median primary energy of around 60 GeV [45, 46].

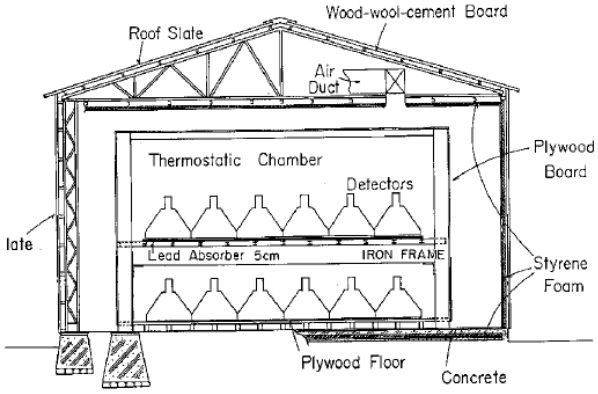

Figure 2.2.10: The layout of the Nagoya Multi-Directional Cosmic Ray Muon Telescope, showing the two layers of 36 detectors separated by an iron frame and 5 cm thick lead absorber which act to absorb the electromagnetic component of an EAS [45].

The Nagoya muon telescope consists of 2 layers of 36 detectors, separated by iron frames and 5 cm thick lead blocks which act to absorb the soft (electromagnetic) component of an EAS. Each individual detector comprises a 1 m^2 plastic scintillator of 5 cm thickness, set at the base of a 1.6 mm thick iron plate box and viewed by a 5" phototube [45]. This setup is shown in Figure 2.2.10.

Other early low energy cosmic ray detectors include the underground muon telescopes at Sakashita (Japan) and Hobart (Australia) which observed cosmic rays with median primary energies of around 350 GeV and 180 GeV respectively [46], as well

as the air shower array at Mt Norikura (Japan) which observed particles originating from cosmic rays with a median energy of around 1.5×10^4 GeV (15 TeV) [46].

2.2.11 AMANDA

The Antarctic Muon And Neutrino Detection Array (AMANDA) was the precursor to the IceCube array (described in Section 2.3.4). It was one of several first generation high energy neutrino detectors and was located at the South Pole. Unlike the other neutrino detectors of that time such as the NT200 detector at Lake Baikal [47] and ANTARES in the Mediterranean [48] that used deep water as their target and detection medium, AMANDA used the 3 km thick South Pole ice layer. The use of ice rather than water meant a larger absorption length as well as a much smaller photomultiplier noise rate since there is an absence of the background K^{40} decays and bio-luminescence that is present in lakes and oceans. It was completed in 2000 and consisted of 19 strings equipped with 677 optical modules suspended in the ice at depths between 1500 m and 2000 m [49]. The AMANDA experiment is now incorporated into IceCube.

2.3 Contemporary Detectors

2.3.1 Tibet Air Shower Array

The Tibet Air Shower Array is located at Yangbajing (90.522° E, 30.102° N), 4300 m above sea level in Tibet. It was designed to detect both hadron and gamma-ray induced air showers with primary energies above a few TeV and covering a wide range of particle densities. It has been upgraded significantly since Tibet I began operation in 1990 with only 65 plastic scintillators placed in a lattice with 15 m spacing.

The full Tibet III array has been operational since 2003 and contains 761 fast timing (FT) counters arrayed in a 7.5 m spaced lattice. This FT counter array is surrounded by 28 density (D) counters. The layout of the final Tibet III configuration is shown in Figure 2.3.1.

Each of the scintillation detectors has a cross-sectional area of 0.5 m^2 and is shielded with a 0.5 cm thick lead plate to increase detector sensitivity. The FT detectors are equipped with fast timing photomultiplier tubes (FT-PMT) that can measure up to 15 particles. In addition, 249 of the FT detectors are also equipped with a density PMT (D-PMT) that can measure to a density of 5000 particles, which increases the accuracy of observations of cosmic ray showers above 10^{15} eV. These are marked on Figure 2.3.1 as dark squares while those FT detectors equipped only with an FT-PMT are shown as pale squares. Both the charge and time of signals measured using the FT detectors is recorded. The D detectors (shown as circles in

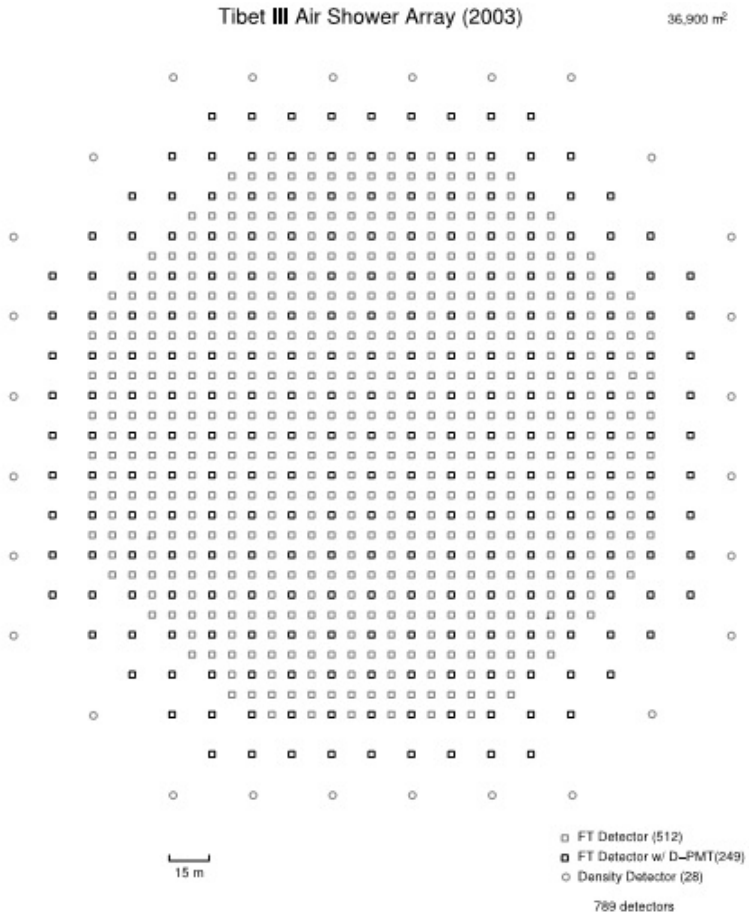

Figure 2.3.1: The final configuration of the Tibet III Air Shower Array showing each of the three different detector types [50].

Figure 2.3.1) also contain both PMT types but only the charge is recorded rather than any timing information [50, 51]. A proposed further expansion of the Tibet III experiment includes the addition of underground water-Cherenkov muon detectors [52].

The triggering condition for the array involves a 4-fold coincidence of the FT detectors with a threshold of 0.6 particles. This gives a triggering rate of around 680 Hz for showers of a few TeV. As with most ground arrays, the number of shower particles is calculated by fitting a suitable lateral distribution function to the measured particle densities. Tibet III uses a modified NKG function which is described in Amenomori et al (2008) [50]. The air shower direction is estimated to within 0.2° for cosmic ray energies above 10^{14} eV and is calibrated using the Moon's shadow.

2.3.2 Milagro

The Milagro observatory is located in the Jemez mountains in New Mexico (35.88° N, 106.68° W) at an altitude of 2630 m above sea level. It is a water-Cherenkov detector comprising a main single 8 m deep reservoir 80 x 60 m in size. This reservoir is filled with around 23 million litres of purified water and protected with a light-tight covering [53, 54].

Inside the reservoir there are two layers of photomultiplier tubes (PMTs). The top layer is positioned 1.4 m below the water surface and contains 450 PMTs. This layer detects the Cherenkov light from electrons produced in air showers, electrons Compton scattered by γ-rays, or γ-rays that have converted to electron-positron pairs in the reservoir. The bottom layer has 273 PMTs positioned at a depth of 6 m. This layer is primarily used to separate hadron and γ-ray initiated showers. Figure 2.3.2 shows a view of the interior of the reservoir with the two layers of PMTs. Using the relative timing of the PMTs triggered in the top layer of the reservoir to reconstruct the direction of an EAS, it is possible to achieve an angular resolution of less than 1°.

The large water-Cherenkov reservoir is surrounded by an array of 175 "outrigger" stations that covers a 200 m x 200 m area. These are cylindrical, polyethylene tanks with a 2.4 m diameter and a height of 1m. Each contains around 4000 litres of water. Cherenkov light produced by charged particles passing through a tank is measured by a single downward-facing PMT positioned at the top of the tank. The outrigger array is used to improve angular resolution and the accuracy of the estimation of primary energy. The full array has been in operation since 2003 [53].

The Milagro experiment operates in two modes: baseline mode and scaler mode. When operating in baseline mode, the detector is able to obtain both arrival rate and direction for hadron and γ-ray induced showers above about 300 GeV. However, in scaler mode it records the rate of PMT triggers from unaccompanied muons produced

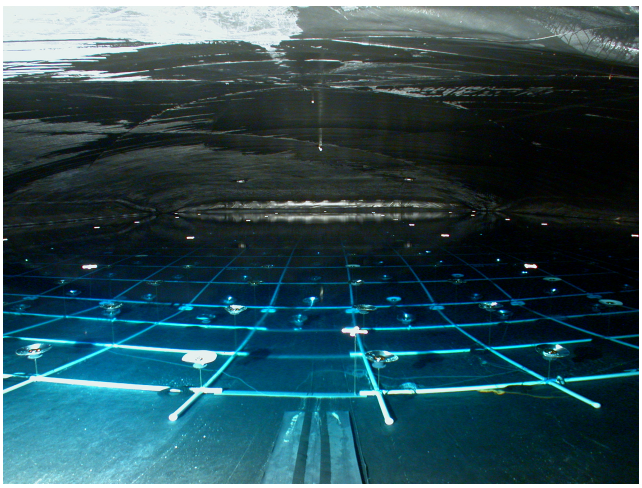

Figure 2.3.2: The interior of Milagro's water-Cherenkov detector reservoir showing the positioning of the PMTs. (taken from `http://physics.nyu.edu/experimentalparticle/milagro.html`)

from cosmic rays with a primary energy threshold of around 5 GeV. Unlike the baseline mode, no directional information is obtained and what is recorded is an integral measurement of the rate above a threshold. The scaler mode provides information somewhat similar to a neutron monitor and can be used to investigate transient solar phenomena. However, it is necessary to correct for pressure, temperature and other diurnal effects [55].

The Milagro experiment is succeeded by the HAWC observatory described below.

2.3.3 HAWC

The High Altitude Water Cherenkov (HAWC) observatory is currently under construction in Mexico and is the direct successor to the Milagro experiment described above. Located at an altitude of 4100 m above sea level at the Sierra Negra volcano in Puebla, Mexico (19^{o} N, 97^{o} W), it is designed to be sensitive to both transient and steady γ-ray emissions at TeV energies, and will improve on the sensitivity, angular resolution and background rejection of the Milagro experiment by an order of magnitude [56].

Unlike the Milagro experiment which comprised of a single deep water reservoir, when complete, the HAWC observatory will consist of an array of 300 water-Cherenkov stations as shown in Figure 2.3.3 a). The prototype to this experiment, VAMOS, has been operational since summer 2001 and consists of 6 water-Cherenkov stations as also shown in Figure 2.3.3 a) as green circles [56, 57].

Each of the stations consists of a light insulated 7.3 m diameter steel tank filled with water to a depth of 4.5 m. Four photomultiplier tubes (PMTs) are mounted at the base of the tank facing upwards as shown in Figure 2.3.3 b) with the central

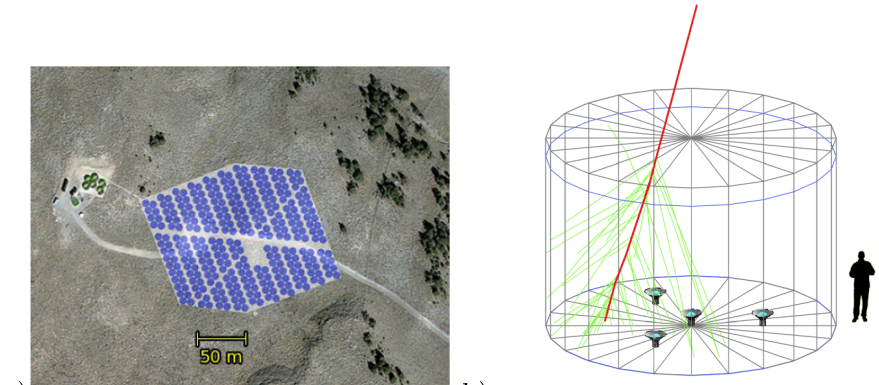

Figure 2.3.3: a) The layout of the planned 300 water-Cherenkov stations comprising the HAWC array (*blue circles*) as well as the 6 stations of the prototype VAMOS array (*green circles*), and b) a schematic of a HAWC water-Cherenkov station showing the positions of the four PMTs mounted at the base of the station, as well as a human silhouette for scale [56].

PMT of high quantum-efficiency. This is designed to improve the detector efficiency to low-energy showers [56].

2.3.4 IceCube

IceCube is a high energy neutrino detector located at the Amundsen-Scott South Pole Station in Antarctica [58]. It is based on work done in the earlier experiment, AMANDA, and incorporates the AMANDA hardware into its design. IceCube consists of two main components; a series of instrumented strings suspended deep within the polar ice-cap called InIce and an array of ice-Cherenkov stations on the surface called IceTop. The detector began full operation in May 2011 with the InIce system containing a total of 5160 sensors on 86 strings, as well as 324 sensors in 162 IceTop detectors [59]. The configuration of the full IceCube experiment is shown in Figure 2.3.4, including the original AMANDA experiment.

IceCube is also sensitive to downward-going muons produced by cosmic ray air showers and has accumulated the largest sample of TeV cosmic ray data every recorded in the Southern Hemisphere [60].

InIce

The InIce system observes the Cherenkov radiation emitted from secondary particles produced in neutrino interactions deep inside the Antarctic polar ice at energies from 100 GeV to a few EeV [58]. It consists of 80 strings of digital optical modules (DOMs) suspended at depths between 1450 and 2450 m. Each string contains 60 DOMs spaced at 17 m intervals and is arranged at the apex of 125 m sided equilat-

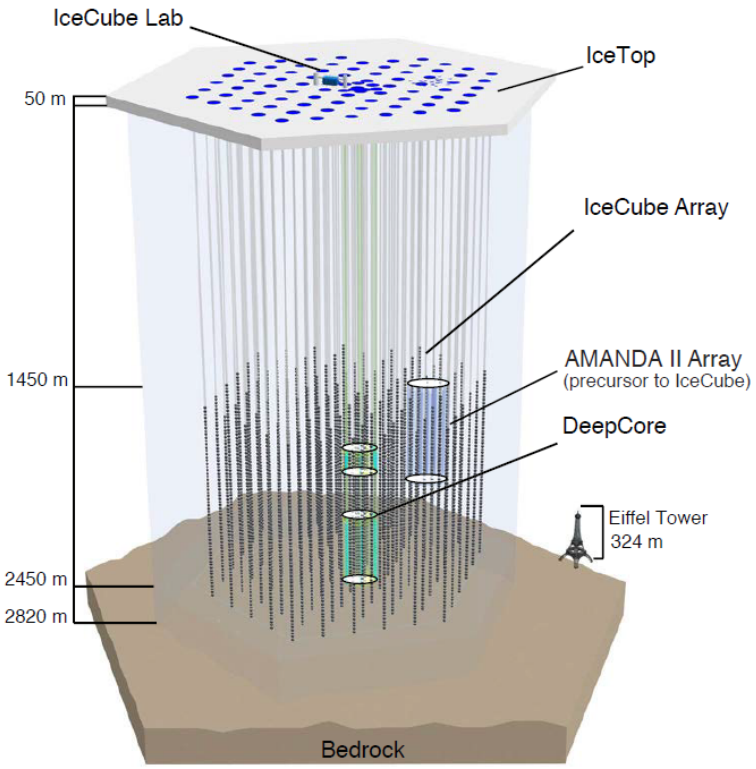

Figure 2.3.4: The IceCube detector at the South Pole showing the strings of detectors in the polar ice-cap comprising the InIce detector as well as ice-Cherenkov array (IceTop) situated at the surface. The original experiment AMANDA as well as the additional DeepCore modules are also shown. The Eiffel tower gives an indication of the scale of the experiment [59].

eral triangles. A DOM consists of a glass sphere containing a 10" photomultiplier and electronics board as shown in Figure 2.3.5. More detailed descriptions of the electronics of a DOM can be found in Abbasi (2009) [58]. Each DOM operates independently. Digitised signals from each DOM are sent to the surface and continuously collected by processors at the top of each string. The signals are then transmitted to the string processor and global event trigger for sorting into the Cherenkov patterns produced by secondary muon tracks. These patterns are used to determine the arrival direction of the primary neutrino [61].

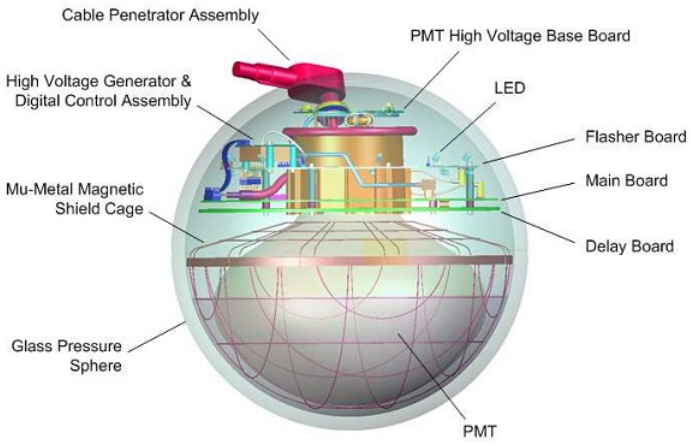

Figure 2.3.5: Schematic illustration of a digital optical module (DOM) used in the IceCube experiment [62].

In addition to the 80 strings, an infill of 6 strings with 60 DOMs is deployed in the bottom half of the detector. The high transparency of the ice at this depth allows the infill, known as DeepCore, to decrease the energy threshold of the detector to around 10 GeV [61]. The location of the DeepCore infill is also shown in Figure 2.3.4. The completed InIce detector contains a total of 5160 DOMs on 86 strings detecting high energy muons with a median energy of 20 TeV [63].

IceTop

In addition to performing cosmic ray research, IceTop's purpose is to complement the InIce installation in assisting with the determination of relative and absolute pointing directions. Also, it helps to distinguish between signals from high energy cosmic ray showers and high energy neutrinos. The completed IceTop array measures the cosmic ray energy spectrum and composition at energies between 10^{14} eV and 10^{18} eV [64].

The completed IceTop array consists of 81 pairs of ice-Cherenkov stations placed approximately 25 m from the top of each of the InIce strings and about 10 m from

each other. Each tank has a radius of 1 m, an ice depth of 90 cm and is protected with a black layer and tank cover. Each tank is equipped with two DOMs, identical to those used in the InIce strings, frozen into the top of the ice in the tank. One of these is set to high gain while the other is set to low gain, which increases the dynamic range of the tank. The triggering of IceTop requires 6 DOMs to trigger simultaneously [64].

2.3.5 The Telescope Array

The Telescope Array is a hybrid detector located in Millard County, Utah, and uses detection techniques previously tested in the AGASA and HiRes experiments (see Sections 2.2.8 and 2.2.6). It was designed with the aim of studying the properties of ultra-high energy cosmic rays above 10^{19} eV and consists of a surface detector array (SD) of scintillation counters overlooked by three fluorescence detector (FD) sites. A map of the overall layout of the Telescope Array experiment is shown in Figure 2.3.6.

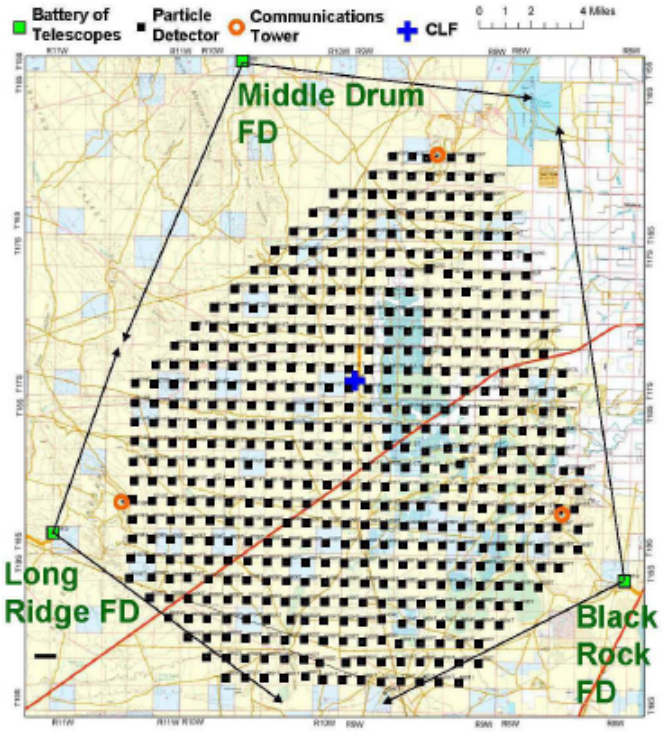

Figure 2.3.6: Configuration of the Telescope Array showing the surface detector array overlooked by the three fluorescence detector stations [65].

The SD is comprised of 507 scintillation detectors arrayed on a square grid with 1.2 km separation. The full SD covers an area of around 730 km^2. Each detector unit

contains two slabs of double-layered plastic scintillator with an overall collection area of 3 m^2 and the light produced in both layers is measured by a single photomultiplier tube. Each unit is powered by its own solar panel and battery system which can continue running for up to a week in complete darkness. The SD units are self-calibrated to the signal produced by vertical equivalent muons (VEM). The triggering of the SD requires at least three adjacent detector units to each register a signal above 3 VEM [66, 65].

The FD sites contain 12 telescopes each and are separated by around 35 km. The field of view of each telescope is centred on the central laser facility that is located equidistantly from each FD site in the centre of the SD array. Each detector site has a total field of view of 3° to 33° in elevation and about 108° in azimuth. The telescope mirrors are based on the design used in the HiRes experiment but on a slightly larger scale (6.8 m^2 compared with the 4 m^2 effective area used in HiRes). As in the HiRes experiment, each of the telescopes contains a 256 pixel camera, positioned at the focal plane of the mirror, in which each pixel is instrumented with a hexagonal photomultiplier tube that views around 1° of sky [66, 65].

3: The Pierre Auger Observatory

The Pierre Auger Observatory is a hybrid cosmic ray detector designed to study the properties of ultra high energy cosmic rays above 10^{18} eV (1 EeV). It comprises a surface detector made up of an array of water-Cherenkov stations overlooked by four fluorescence detector sites. It is located in the high plains of Argentina, at 35° S and 69° W, in a site that was chosen for the following properties:

- an average altitude of 1420 m allows the properties of cosmic ray air showers to be measured at ground level, just past the point of shower maximum;
- a large flat area allowing good wireless network coverage over the full area covered by the detector;
- dry semi-desert conditions with minimal atmospheric aerosol content are ideal for operation of the fluorescence detector; and
- near the town of Malargüe which provides infrastructure.

The location of the Pierre Auger Observatory within Argentina is shown in Figure 3.0.1. The inset depicts the layout of the surface detector with the positioning and fields of view of the four fluorescence detector sites as well as the Observatory's location with respect to the town of Malargüe. This chapter describes each of the major components of the Pierre Auger Observatory as well as briefly discussing recent enhancements.

3.1 Surface Detector

The original surface detector (SD) of the Pierre Auger Observatory consists of 1600 water-Cherenkov stations spaced 1.5 km apart in a triangular grid forming an array that covers an area of around 3000 km^2. A recent enhancement to the surface detector (AMIGA) has added another 60 water-Cherenkov stations as a smaller infill array, bringing the total number of water-Cherenkov stations to 1660. The AMIGA enhancement is described in more detail in Section 3.4.1.

The tanks measure Cherenkov light produced as charged particles from cosmic ray air showers pass through the water of the tank, with the resulting signals then

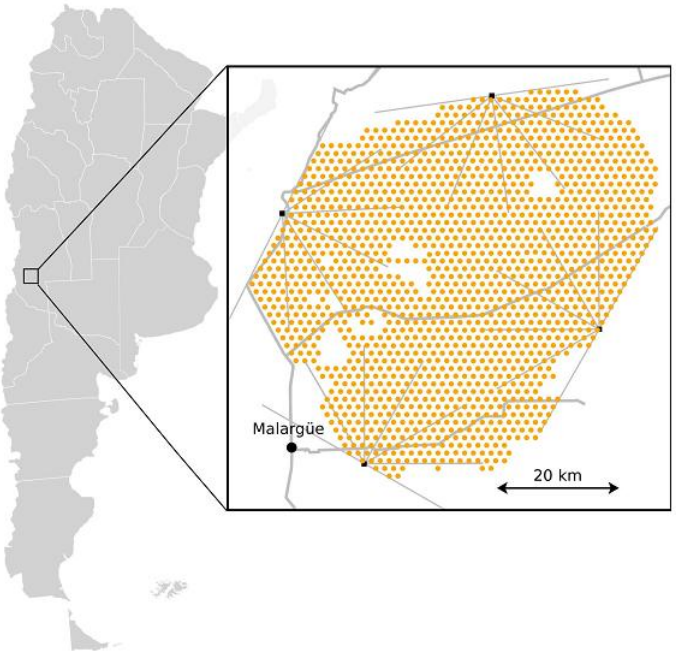

Figure 3.0.1: The Pierre Auger Observatory is located near the town of Malargüe in Argentina. The layout of the surface detector array, overlooked by the four sites of the fluorescence detector, is shown in the inset [67].

processed through a hierarchical triggering system that starts at the local tank level and progresses to array-wide conditions to identify and isolate cosmic ray air shower data. This section describes the design and operation of the surface detector water-Cherenkov stations as well as the triggering system and operation of the whole array.

3.1.1 Water-Cherenkov Tank Design

The design of the water-Cherenkov stations that make up the surface detector of the Pierre Auger Observatory is very important. The Observatory is planned to operate for more than 20 years and, consequently, the stations must be able to operate in a stable manner for this extended period of time. They must also be able to withstand the local environmental conditions as well as be able to be repaired and maintained with minimal disturbance to their operation.

The water tanks are cylindrical in shape with a 3.6 m diameter and 1.6 m in height. They are molded from high density polyethylene in a pale beige colour so as to minimise visual pollution of the landscape. Figure 3.1.1 shows a water-Cherenkov tank deployed in location with labels showing its various components. The tanks contain a sealed Tyvek® liner with a reflective inner surface to diffusively reflect any Cherenkov light produced by charged particles passing through the water. Both the liner and the tank itself are totally opaque. The 12,000 litres of purified water which

fills the liner has a depth of 1.2 m. It is viewed by three 9" photomultiplier tubes (PMTs) located symmetrically 1.2 m from the centre of the tank. These view the water through clear windows of polyethylene which allows replacement of the PMTs without exposing the water to the environment. In addition to these three PMT windows, the liner also has five fill ports with screw caps which are hermetically sealed to the liner. These ports are used for filling and emptying the tank as well as for allowing light from an LED flasher into the tank when performing tests of PMT operation.

Each water-Cherenkov station is self-contained and operates autonomously. It has its own electronics and communications systems which are powered by a solar panel oriented to face the north at an inclination of 55°. This maximises the light collected in the winter months. The battery box is secured to the south side of the tank so that it is protected from direct sunlight by the tank's shadow. Keeping the battery's temperature as low as possible prolongs the battery life. All external components of the surface detector station are designed to withstand winds of up to 160 kmph.

The electronics for each tank are mounted directly on the hatch cover. This minimises the length of cabling, the number of connections and the number of feedthroughs required. The two antenna cables and the solar panel cable are the only cables that are exposed to the external environment [68].

The signals measured by each of the three PMTs are processed by the local electronics which include an 80 MHz processor as well as six 40 MHz flash analogue to digital converters (FADCs). These FADCs digitise the signals from the anode and last dynode of each of the PMTs. The signal from the last dynode is also amplified and inverted to produce a signal approximately 32 times that of the anode. This provides enough dynamic range for measurement of the particle flux both near the core ($\sim$1,000 particles μs^{-1}) and at large distances from the core ($\sim$1 particle μs^{-1}) . The signal is recorded in units of FADC channels (ch) with a range of 0-1023. Each FADC time bin corresponds to 25 ns [68, 69].

3.1.2 Calibration

Because of the limited bandwidth available for communication between each station and the central data acquisition system (CDAS), calibration of each SD station is performed locally. In order to do this, a calibration unit is needed which is common for all stations across the array and can also be used in SD station simulations. The triggering system also requires such a common, yet station independent, unit for its threshold definitions. The charge deposited in a PMT by the Cherenkov light produced by the passage of a single central, vertical and through-going muon through a tank provides such a unit. This unit is known as a vertical equivalent muon (or

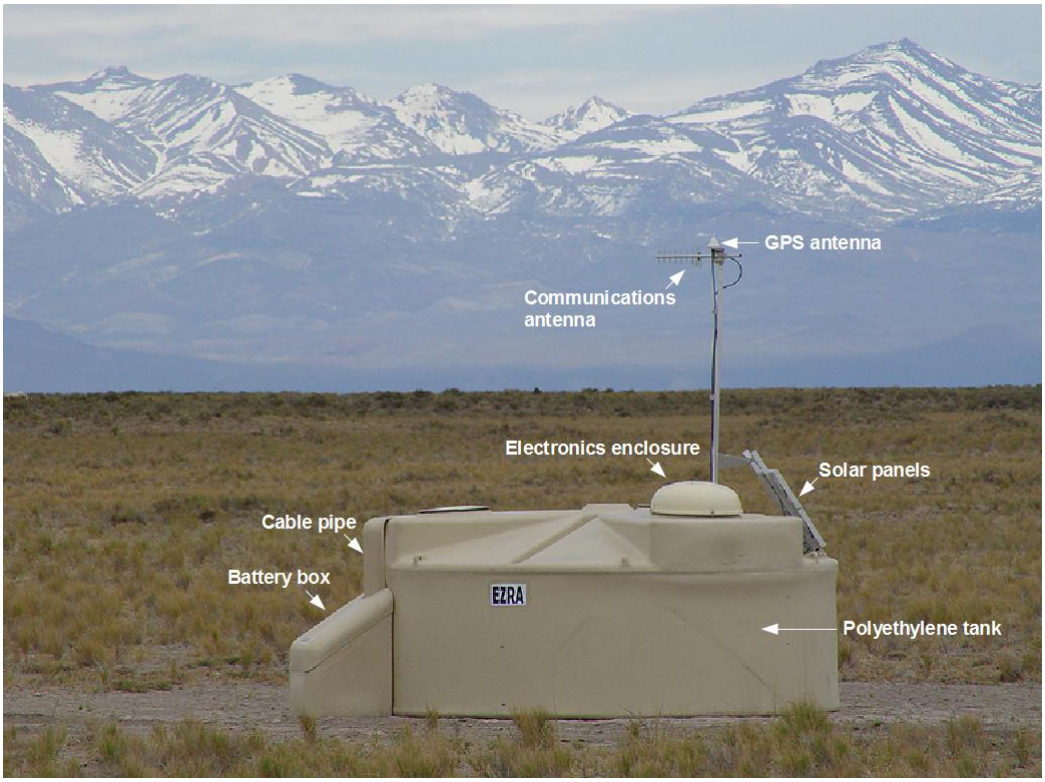

Figure 3.1.1: Photograph of a water-Cherenkov tank deployed in location at the Pierre Auger Observatory with labels showing the various components.

VEM).

The distribution of signal charges measured at each PMT shows a peak corresponding to the Cherenkov light produced by atmospheric muons (Q_{VEM}^{peak}). Tests performed in which a muon telescope triggered only vertical muons have shown that, for a single PMT, $Q_{VEM}^{peak} = 1.03 \pm 0.02$ VEM, while for the sum of all 3 PMTs $Q_{VEM}^{peak} = 1.09$ VEM. The distribution of pulse heights measured by each PMT shows a similar peak (I_{VEM}^{peak}). This value is used as the station independent unit for the local triggering thresholds (described in the Section 3.1.3). Examples of the charge and pulse height distributions for the sum of all 3 PMTs overlayed with the corresponding distribution of charge and pulse heights produced by vertical muons are shown in Figure 3.1.2.

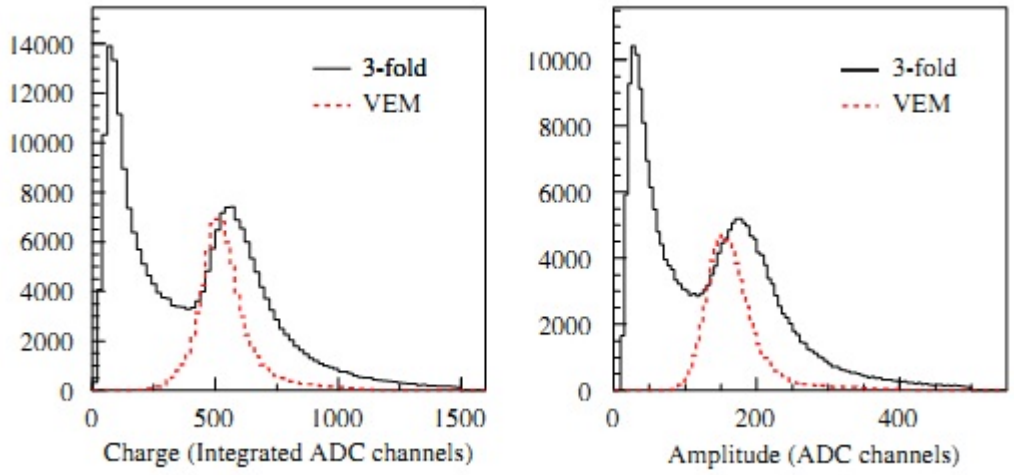

Figure 3.1.2: Example charge and pulse height histograms of the sum of the 3 PMTs. Also shown is the corresponding charge and pulse height distribution produced by only vertical, central and through-going muons (VEM) [69].

Initially the end-to-end gains for each individual PMT are set such that I_{VEM}^{peak}= 50 ch (note that Figure 3.1.2 show the charge and pulse height histograms produced for the sum of the 3 PMTs and so I_{VEM}^{peak}(3 PMTs) $\approx$ 150 ch). This value of I_{VEM}^{peak} (in channels) is then calibrated continuously to compensate for any drifting that may occur over time. This is very important since the electronics trigger levels are set with respect to I_{VEM}^{peak}. Finally, the value of Q_{VEM}^{peak} (in channels) is determined using a quadratic fit to the charge histogram. The conversions described above are then used to obtain this value of Q_{VEM}^{peak} in units of VEM. That is, the signal from any PMT from any SD station can now be expressed in terms of this common, station independent, unit of VEM [69].

3.1.3 Array Triggering and Operation

Data from each surface detector station are transmitted wirelessly to the central data acquisition system (CDAS). Because of the limitations inherent in transmitting and receiving data from ∼1600 stations spread over 3000 km^2, one of the primary functions of the triggering system is to reduce the event data from each individual station to a rate manageable by the communications system. This is approximately one event per detector station per hour. In order to achieve this, a hierarchical triggering system is in operation in which the initial two triggers (T1 and T2) are at the local station level. The third level trigger (T3) and above (T4 and T5) are array-wide triggers.

T1

The first level trigger consists of two conditions, either of which may be met. The first is a simple threshold trigger (Th) requiring a 3-fold coincidence of all the PMTs in the tank, each measuring a signal above $1.75 I_{VEM}^{peak}$. This trigger is designed to detect short, strong signals and is used to reduce the background rate of detection at each station from around 3 kHz to approximately 100 Hz. It is useful in the detection of very inclined showers which have traversed large amounts of atmosphere, resulting in primarily muons reaching ground level.

The second trigger condition is a time-over-threshold trigger (ToT) designed to detect signals that are spread over time. It requires at least 13 bins in a 120 FADC bin sliding window to be above $0.2 I_{VEM}^{peak}$. Since each FADC bin is 25 ns, this condition corresponds to a signal above the threshold of $0.2 I_{VEM}^{peak}$ for more than 325 ns out of a 3 μs window. At least two of the three PMTs are required to satisfy the ToT triggering condition. This trigger is optimised for the detection of low energy showers in which the core falls near the tank or for distant, high energy showers and is very efficient at eliminating the background muon signal. In comparison to the average T1-Th triggering rate of around 100 Hz, the average T1-ToT triggering rate at each station is less than 2 Hz; with the majority of this rate being the case in which two or more muons arrive within the 3 μs window [70, 71].

T2

The second level trigger is very similar to the T1 triggering conditions with both a simple threshold and time-over-threshold trigger. It is applied in the station controller and has the purpose of reducing the event rate at each station further, down to approximately 20 Hz. All events that satisfy the T1-ToT triggering condition are promoted to T2-ToT triggers. However those events which satisfy the T1-Th triggering condition must pass a further threshold cut in order to trigger as T2-Th

events. That is, there must be a three-fold coincidence of all the PMTs in the station measuring a signal above $3.2I_{VEM}^{peak}$ [70, 71].

T3

The third level trigger is the first trigger which involves the whole array. The central data acquisition system (CDAS) forms this trigger based on the spatial and temporal distribution of T2 triggers across the array. If an event satisfies the T3 trigger, data from all the T2 triggered stations involved in the T3 event are sent to CDAS. In addition, data from all T1s that triggered within 30 μs of the T3 are also sent to CDAS.

Like the T1 and T2 triggers, the T3 trigger has two different trigger modes. The first T3 trigger type requires at least three stations that have triggered as T2-ToT and that satisfy a minimum compactness requirement. That is, the three stations include one closest neighbour and one second closest neighbour. The left panel of Figure 3.1.3 shows an example of this 3-fold T3 triggering geometry. Additionally, the three stations must satisfy the timing criteria whereby each of the three T2-ToT triggered stations must have triggered within $(6 + 5C_n)$ μs of the first triggered station, where C_n is the number of neighbours distant from the first triggered station [70]. Because of the low background in the ToT trigger, the T3 triggers of this type are mostly physics events. The full array triggers this type of T3 event around 1600 times per day.

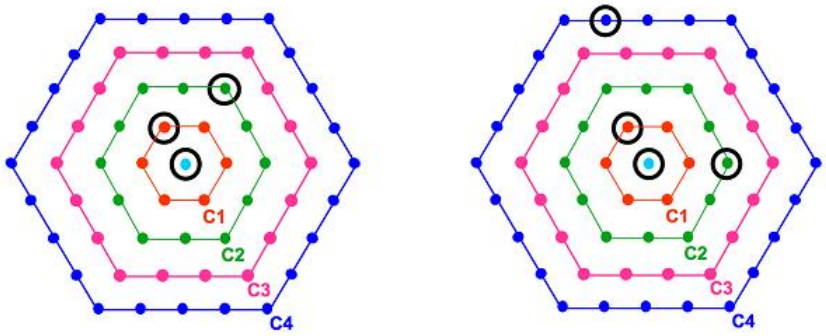

Figure 3.1.3: Examples of the two T3 triggering types. The first (left panel) is the 3-fold triggering configuration in which at least 3 stations must have satisfied the T2-ToT and the minimum compactness condition. The second (right panel) is the 4-fold triggering configuration where at least 4 stations have satisfied any T2 condition as well as the moderate compactness requirement. (See text for more details). C1, C2, C3 and C4 are the first, second, third and fourth sets of neighbours to the central station respectively [70].

The second T3 triggering type is less exclusive than the first. It requires a 4-fold coincidence of any T2 type triggers that satisfy the moderate compactness

requirement. That is, of the four stations, at least two must be within the first two closest set of neighbours of the first station while the remaining station only has to be within the first four closest set of neighbours. An example of this 4-fold T3 triggering geometry is shown in the right panel of Figure 3.1.3. The timing requirement is the same for both T3 triggering types. This second type is efficient for the detection of horizontal showers since the component reaching the ground in this case is primarily muonic and so has a narrow time spread but a large ground area coverage. Of the events selected using the second type of T3 trigger, however, only around 10% are real showers (compared with around 90% for the first T3 trigger type) [70, 71].

Higher Triggers

The triggers T1 to T3 are all applied during the data acquisition process. Further selection from the T3 events is needed to separate real events from accidental coincidences. The first of these selection processes is the T4 trigger.

The T4 trigger is a physics trigger which is performed following the data acquisition process to select real showers from the set of stored T3 event data. There are two different types of T4 trigger: 3ToT and 4C1. The 3ToT trigger requires three nearby stations in a triangle to have passed the T2-ToT condition. This triggering criterion results in a subset of T3 events of which more than 99% are real showers with a median energy of around $6\text{x}10^{17}$ eV. The second T4 type trigger requires four nearby stations to have passed the T2 trigger of any type. This triggering criterion has an efficiency of around 100% for identifying real showers with zenith angles below 60^{o} and results in a subset with a median energy of about $3\text{x}10^{18}$ eV.

In order to identify and remove any stations which have coincidentally triggered but are not part of the CR event a "seed" of three neighbouring stations in a triangular configuration is used. All three stations must match the type of T4 condition applied (i.e. if the T4 trigger is a 3ToT type, then all three seed stations must have satisfied the T2-ToT condition). The arrival direction of the shower is then estimated by fitting the timing of each of the signals from these three stations to a plane shower front moving at the speed of light. The remaining stations which have triggered are then investigated to determine whether or not they fall within the time window for that shower. The combination of these T4 selection criteria produces a subset of events in which 99.9% may be successfully reconstructed.

The final triggering condition (T5) is designed to remove events in which the shower falls close to the edge of the array. In these cases, the event is often misreconstructed since some portions of the shower may be missing. The T5 trigger requires that the station registering the highest signal is surrounded by a full hexagon of working stations at the time of the event. It is applied *a priori* in order to remain independent of the reconstruction process. This is a highly efficient triggering

condition but one which also reduces the effective area of the surface detector by around 10% [70, 71].

3.1.4 Event Reconstruction

The geometry of a cosmic ray air shower that triggers the SD is determined by the position and triggering times of the SD stations involved in the event. A parabolic shower front model is fitted to the arrival times of the first shower particle measured by each of the triggered stations. From this fit, the arrival direction of the shower can be determined. A parabolic shower front has been shown to be an adequate timing model and does not contribute significantly to the uncertainty in the arrival direction determination [72]. The main contributions to this uncertainty come from the precision of the clock used in each SD station to measure the particle arrival times and from the natural event-to-event fluctuations in the arrival times of the first shower particle.

Since the SD only samples the shower front at a limited number of points that differs on an event by event basis, a standard observable that may be used to represent the shower size is required. The signal that would have been measured in a station positioned 1000 m from the shower core ($S(1000)$) is used for this purpose. The relative fluctuations in the value of $S(1000)$ as a function of zenith angle have been shown to be energy independent and are generally found to be $\sim$10%. The value of $S(1000)$ is determined for each event by fitting the measured signals and tank positions to the following lateral distribution function (LDF) [73]:

$$S(r) = S(1000)\left(\frac{r}{1000}\right)^{-\beta}\left(\frac{r+700}{1700}\right)^{-\beta} \tag{3.1.1}$$

where r is the distance from the triggered tank to the shower core in the plane of the shower front and $S(r)$ is the signal measured at tank distance r. The "slope" parameterβ of the LDF is derived from a parameterisation $\beta = \beta(\theta, S_{1000})$. Uncertainties in the value of $S(1000)$ determined in this manner include fitting errors due to uncertainties in the individual station signal measurements and errors due to the lack of a precise knowledge of the LDF form for an individual event.

To be used as an energy parameter, the value of $S(1000)$ must be corrected for zenith angle dependent attenuation. This is done by converting $S(1000)$ to the signal the shower would have produced in a tank 1000 m from the core if the shower had an arrival direction of 38° (S_{38°). The angle of 38° is the median zenith angle of the measured cosmic ray arrival directions. A calibration curve derived from a subset of high quality hybrid events is then used to convert the signal value S_{38° to a measurement of the primary cosmic ray particle energy [74, 75].

3.1.5 Scaler Mode

The scaler mode of the Pierre Auger Observatory surface detector was designed with the purpose of researching transient effects such as gamma-ray bursts (GRBs) and solar flares. It is also a very useful tool for studying and monitoring the long term stability of the SD.

The scaler mode records very low threshold rates from each station of the array. These rates are measured every second and transmitted to the CDAS for storage. Transient effects are expected to appear as distinct, short-term changes in these rates from their expected values.

There have been two implementations of the scaler mode. The initial implementation, in March of 2005, recorded all signals above 3 FADC channels and resulted in a counting rate of around 38,000 counts per second at each SD station. The second implementation, in September 2005, placed an upper limit on the recorded signal in order to remove the background signal from muons. This new implementation recorded all signals between 3 and 20 FADC channels and resulted in a new counting rate of only around 2000 counts per second at each station. This second implementation continues to operate on all SD stations [67].

3.2 Fluorescence Detector

The original fluorescence detector (FD) consists of 24 telescopes located at four sites (Los Leones, Los Morados, Loma Amarilla and Coihueco). A recent enhancement to these telescopes (HEAT) has increased the number of telescopes to 27 and is described in Section 3.4.2. The FD sites are positioned on small elevations at the perimeter of the surface detector, overlooking the array. The telescopes at each of the four sites detect UHECR air showers by measuring the UV fluorescence light emitted as the particles in an air shower excite nitrogen molecules in the atmosphere. As with other detectors that use the fluorescence detection technique, the FD is only able to be operated during dark moonless nights. This section briefly describes the design and operation of the fluorescence detector of the Pierre Auger Observatory.

3.2.1 Detector Design

Each FD site contains six telescopes which each have a field of view covering 30° x 30° in azimuth and elevation. The telescopes are housed in a clean, climate-controlled building and oriented such that their combined fields of view span a continuous 180° in azimuth. The layout of the building housing the six telescopes at a fluorescence detector site is shown in Figure 3.2.1.

Fluorescence light enters each telescope bay through large windows that contain

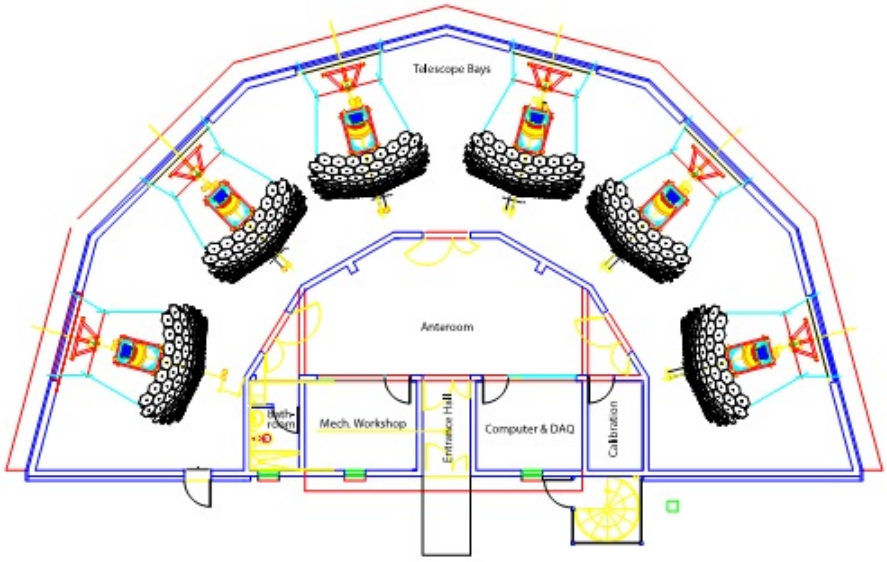

Figure 3.2.1: The layout of a fluorescence detector site showing the six telescopes and their relative orientation [76].

a filter which allows only UV light to pass through plus a Schmidt optics corrector ring. The windows also contain heavy shutters to completely protect the system from over exposure to light when not in use. This light is focussed onto a 440 pixel camera by a 10 m^2 spherical mirror made up of segmented mirrors. Each pixel in the camera is instrumented with PMT light sensors which measure the light pulses in the 1.5° diameter hexagonal area of sky seen by each pixel. These light pulses are digitised and processed using a hierarchical triggering system [76]. The layout of a telescope bay is shown in Figure 3.2.2.

3.2.2 Triggering System

The triggering system of the FD of the Pierre Auger Observatory is hierarchical with three levels. There is also a hybrid trigger following the third level trigger (TLT) in which those events that pass the TLT also form an external trigger for the surface detector. This is described in more detail in Section 3.3.

First Level Trigger (FLT)

The first level trigger (FLT) looks for signals in each pixel above a threshold. Each telescope contains 20 FLT boards that each monitor a column of 22 PMTs. The signal from each PMT is digitised using a 12-bit analogue to digital converter (ADC) at 10 MHz. The pixel trigger monitors a moving sum of the last $n = 10$ ADC samples (this value of n has the capacity to be varied from 5 to 16) and compares this sum to

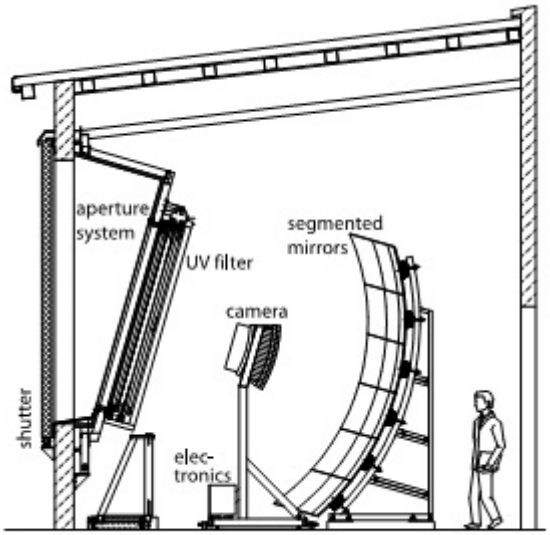

Figure 3.2.2: Schematic view of a single telescope bay. Fluorescence light enters the bay through the large window and aperture system and is focussed onto the camera by the 10 m^2 segmented spherical mirror [76].

a 14-bit threshold. The value of this threshold is continuously adjusted to maintain a triggering rate of 100 Hz for each pixel. Using a sum rather than individual ADC samples improves the signal to noise ratio significantly [76].

Second Level Trigger (SLT)

The purpose of the second level trigger (SLT) is to identify patterns in the triggered pixels that correspond to straight tracks. It reads in the triggered pixels from all 20 FLT boards and scans for tracks at least 5 pixels in length that match a set of recognised patterns. The five basic patterns are shown in Figure 3.2.3. The SLT also looks for those patterns produced by rotations and reflections of these basic patterns. The triggering rate of the SLT is 0.1 to 10 Hz per telescope [76].

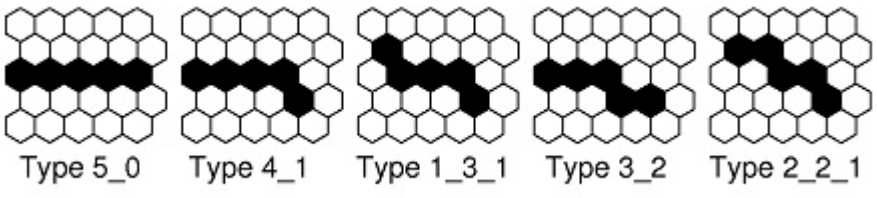

Figure 3.2.3: The five basic patterns of triggered pixels that are recognised as straight track segments [76].

Third Level Trigger (TLT)

The third level trigger (TLT) is a software trigger and is performed at the MirrorPC computer of each telescope. The TLT goes through the tracks that have been identified by the SLT and removes noise events. That is, it identifies and rejects those triggers produced by lightning events, muon impacts on the camera or by randomly triggered pixels. The decision time of the TLT is very fast (within 50 μs) and also very efficient. It removes around 99% of lightning events while losing less than 0.7% of the true showers. Following the TLT, the triggering rate at each telescope is around 0.01 Hz. Events that pass the TLT are sent to the EyePC of that FD site where an event builder merges coincident events from adjacent telescopes [76].

3.2.3 Event Reconstruction

Figure 3.2.4 shows a cosmic ray event detected using the FD. The sequence of triggered pixels in a straight track as well as the signal amplitudes measured in these triggered pixels are shown. The positioning and timing of these triggered pixels are used to reconstruct the shower geometry (shown in Figure 3.2.5), with the quantity of measured light then used to estimate the energy deposited in the atmosphere and, hence, the energy of the primary cosmic ray particle.

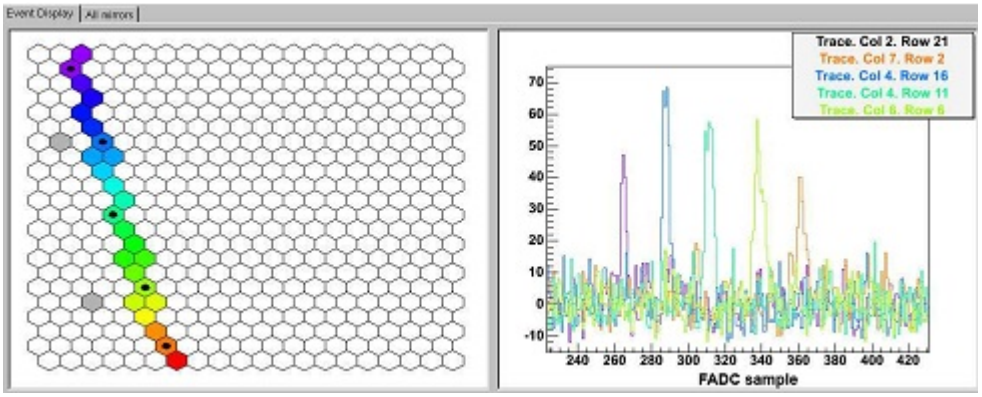

Figure 3.2.4: A example of a cosmic ray event as seen by the fluorescence detector [76].

The shower detector plane (SDP) is first determined from the geometry of the triggered pixels, and includes both the FD site and the line of the shower axis. The timing information from each pixel is then used to identify the shower axis within the SDP. The shower axis can be characterised by two parameters: the perpendicular distance from the fluorescence camera to the shower track (R_p) and the angle between the track and the horizontal (χ_0). Each of the pixels that view the shower track has a pointing direction that makes an angle with the horizontal (χ_i). If t_0 is the time at which the shower front passes the point closest to the camera (R_p) then light will

arrive at the ith pixel at time [76]:

$$t_i = t_0 + \frac{R_p}{c} \tan\left[(\chi_0 - \chi_i)/2\right] \tag{3.2.1}$$

The shower parameters R_p and χ_0 can be determined by fitting the measured data points to this function.

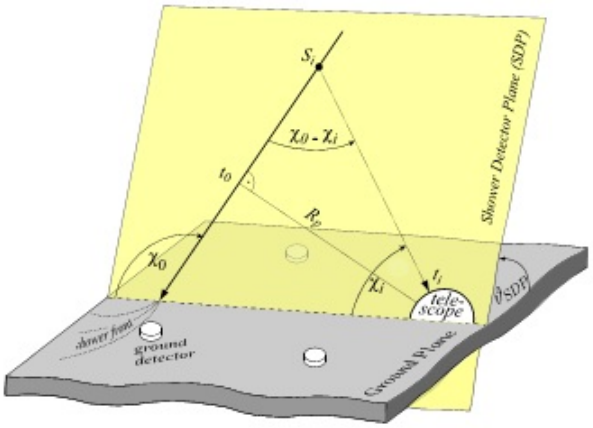

Figure 3.2.5: Shower geometry showing the shower detector plane (SDP) containing both the FD telescope and the shower axis. The shower axis can be parameterised by the perpendicular distance R_p between the camera and the shower track and the angle χ_0 that the track makes with the horizontal [76].

The accuracy of this geometrical reconstruction technique can be checked by reconstructing tracks with known geometries such as those produced by the laser shots from the central laser facility (CLF) [77].

Once the geometry of a cosmic ray air shower has been reconstructed, the amount of light collected at the telescope can be converted into a measure of the amount of energy deposited by the shower as a function of its slant depth. For this conversion to be accurate, it is necessary to estimate the amount of attenuation that occurs between the shower and the telescope. The different light source contributions must also be identified and isolated. In addition to the fluorescence light, these include direct and scattered Cherenkov light as well as fluorescence light that has undergone multiple scattering.[76] In order to correctly account for these contributions, it is important to have precise knowledge of the atmospheric conditions at the time of the event. The cloud cover, temperature, pressure, aerosol content and other atmospheric conditions are regularly monitored and used to update models for the expected atmospheric conditions between measurements [78].

Since the amount of fluorescence light emitted is directly proportional to the total energy deposited by the air shower as described in Section 2.1.2, the atmosphere can

be used as a calorimeter. By fitting a Gaisser-Hillas profile (described in Section 1.4, Equation 1.4.2) to the reconstructed energy deposition profile, the total energy deposited by the electromagnetic component of the shower is then estimated by taking the the integral of this fit over the atmospheric depth. The energy of the primary cosmic ray particle is then derived by correcting for the energy carried by neutrinos and high energy muons that are not measurable using the fluorescence technique. This is known as "invisible energy". Following these corrections and quality cuts, the energy resolution achievable by the fluorescence detector is within 10% [76].

3.3 Hybrid Operation

Hybrid cosmic ray events are those which are simultaneously detected by both the fluorescence detector and surface detector. In the case that a cosmic ray air shower independently fully triggers both the SD and FD, that hybrid event is tagged as a "golden hybrid". Such events may be reconstructed in either detection mode or their data may be combined to produce a more precise event reconstruction than is achievable independently.

The fluorescence detector has a lower triggering energy threshold than the surface detector. When an event satisfies the FD triggering requirements (see Section 3.2.2), a hybrid trigger is also transmitted to the CDAS. This provides an external T3 trigger which can promote sub-threshold triggers in the SD by matching their timing and location even though they may not satisfy the SD's T3 triggering requirements (see Section 3.1.3). This hybrid trigger is very powerful since it allows an extension of the hybrid measurement of the energy spectrum into a region in which the SD is not fully efficient.

In a hybrid event, the shower geometry is reconstructed via the same method used by the FD (as described in Section 3.2.3) but is supplemented by data from the triggered SD stations. These data provide information on the arrival time of the shower at the ground, effectively extending the measurements of the shower track and so allowing the precision of the shower geometry to be greatly improved. The shower core impact position and direction may be determined by this method to within 50 m and 0.6° respectively [79].

Once the shower geometry has been determined, the energy of the primary cosmic ray particle is estimated using the same technique as used by the FD. That is, the energy deposited by the electromagnetic component of the shower is estimated by fitting a Gaisser-Hillas profile to the reconstructed deposited energy profile and integrating over the atmospheric depth. The total energy deposited by the shower is then estimated by correcting for the invisible energy carried by neutrinos and high

energy muons which do not contribute to fluorescence production [79].

3.4 Enhancements

This section briefly describes the various enhancements that have been made to the Pierre Auger Observatory beyond the original fluorescence and surface detectors.

3.4.1 AMIGA

The surface detector of the Pierre Auger Observatory is fully efficient above $3x10^{18}$ eV. The Auger Muons and Infill for the Ground Array (AMIGA) is an enhancement to the surface detector which aims to lower this energy threshold to around 10^{17} eV via an infill of the surface detector.

AMIGA comprises both an infill of 60 water-Cherenkov stations into the array, spaced 750 m apart and covering an area of 23.5 km^2, as well as an array of muon counters to be buried alongside the detectors in the infill. The muon counters are 30 m^2 scintillators and are buried to a depth of 2.3 m which will allow the muon content of an air shower to be determined for muons with energies $\geq$ 1 GeV. The muon counters are currently deployed only in a small engineering array known as the Unitary Cell consisting of 7 scintillators deployed in a hexagon and a central counter. Figure 3.4.1 shows the current layout of the AMIGA infill array of 60 water-Cherenkov stations as well as the Unitary Cell [80].

A second infill is also planned, which will cover a smaller area (5.9 km^2) with a 433 m triangular grid. Once complete, this second infill will lower the energy threshold over the infill area to 10^{17} eV [81].

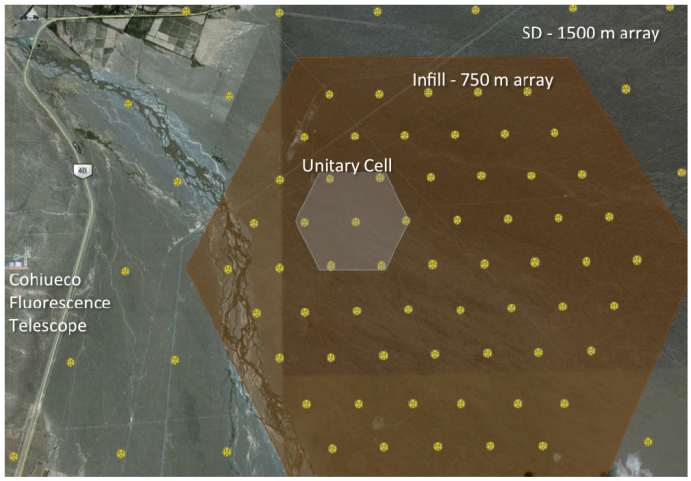

Figure 3.4.1: The layout of the AMIGA array located near the the Coihueco FD site. The grey area marks the Unitary Cell in which the first seven muon detectors are being deployed [80].

3.4.2 HEAT

The High Elevation Auger Telescope (HEAT) is an enhancement to the existing fluorescence detector that has been operating since September 2009. It consists of three telescopes of a similar design to the existing FD telescopes (described in Section 3.2.1) but with the ability to be tilted to an angle of 29° in order to have a field of view covering the elevation range 30° to 58°. The HEAT telescopes are located 180 m to the north of the Coihueco FD building overlooking the new AMIGA infill array. The location and fields of view of HEAT are shown in Figure 3.4.2.

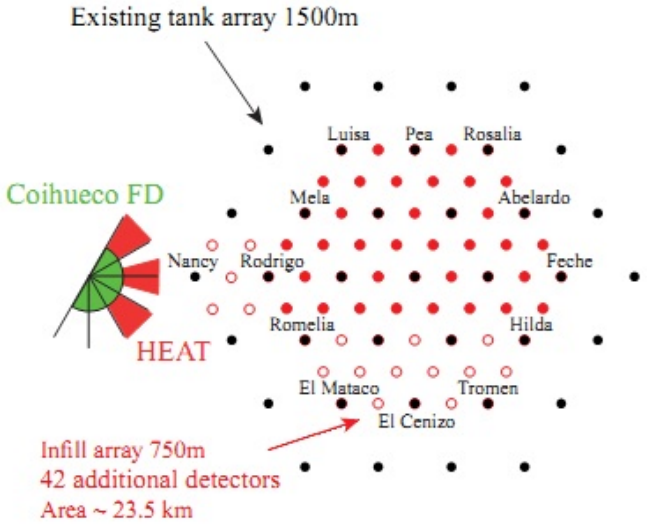

Figure 3.4.2: The location and field of view of the HEAT enhancement to the existing fluorescence detector. The AMIGA infill array is also shown [82].

Unlike the existing FD telescopes, which are housed in a single solid building at each FD site, the HEAT telescopes are installed in individual buildings that are pivot mounted, allowing each telescope to be raised or lowered independently. The operation of the HEAT telescopes follows the same principle as that of the FD telescopes but with modernised and updated electronics. The HEAT installation effectively operates as a fifth FD site [82].

3.4.3 AERA

The Auger Engineering Radio Array (AERA) is an extension of the Pierre Auger Observatory used to study the emission of radio waves from extensive air showers. It operates in the 30-80 MHz frequency range and was recently expanded to 124 radio stations covering an area of approximately 6 km^2, with an additional 36 stations planned which will extend the area to over 10 km^2. AERA co-located with the AMIGA infill within the fields of view of both the HEAT and Coihueco fluorescence

telescopes in order to facilitate calibration of the radio signal [83, 84].

The initial phase of AERA began operation in April 2011, consisting of 24 stations with logarithmic periodic dipole antennae (LDPA), deployed on a triangular grid with a spacing of 125 m over an area of 0.5 km^2. This initial array was extended during 2013 by the addition of 100 additional stations of a different design and antenna type. The new stations use two butterfly antennae rather than the LDPA due to economic and performance factors [84]. Figure 3.4.3 a) shows an example of the new station deployed in this second phase, while Figure 3.4.3 b) shows the position and layout of the current and planned AERA units.

a)

b)

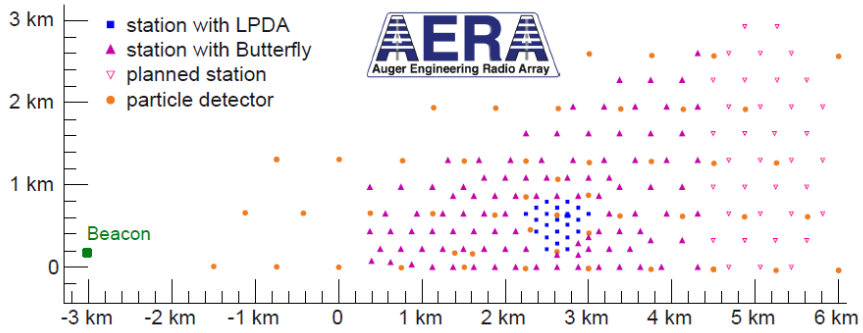

Figure 3.4.3: The AERA enhancement of the Pierre Auger Observatory showing a) a radio station of phase 2, and b) the position and layout of the current and planned AERA units [84].

3.4.4 AMBER, MIDAS and EASIER

The most recent enhancement of the Pierre Auger Observatory is the installation of detectors to detect cosmic rays in the microwave frequencies. This enhancement comprises three detectors, which each have a different setup and will be described briefly. The AMBER and MIDAS detectors are both imaging telescopes, whereas EASIER is more similar to a radio telescope and is embedded in the surface detector array. The location and layout of the three detectors within the Pierre Auger

Observatory is shown in Figure 3.4.4.

AMBER and MIDAS

AMBER (Air shower Microwave Bremsstrahlung Experimental Radiometer) is a radio telescope consisting of a 2.4 m parabolic dish which images a 14^{o} x 14^{o} area of sky with 16 pixels at an elevation of 30^{o}. It is now installed at the Coihueco FD site, overlooking the AMIGA infill array [85].

The MIDAS (Microwave Detection of Air Showers) telescope consists of a 5 m^2 parabolic dish with a 53 pixel camera positioned at its focal plane. Each pixel views an approximately 1.3^{o} x 1.3^{o} area of sky, giving a total field of view of $\sim 20^{o}$ x 10^{o}. MIDAS is currently installed at the Los Leones FD site [85]. Figure 3.4.5 shows photographs of the a) AMBER and b) MIDAS telescopes.

EASIER

Unlike AMBER and MIDAS, EASIER (Extensive Air Shower Identification with Electron Radiometer) is a radio detector array, embedded in the existing surface detector array. Each individual detector consists of a C-band horn antenna, positioned 3 m above the ground and oriented towards the zenith, covering a wide field of view. Each EASIER detector is also linked to the corresponding water-Cherenkov detector such that, whenever an air shower triggers the SD, the corresponding radio trace is automatically recorded in the same data stream [85]. Figure 3.4.5 c) shows an EASIER detector installation at a surface detector.

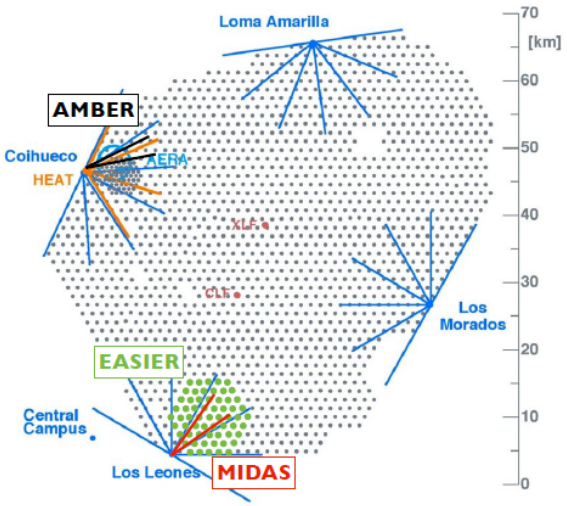

Figure 3.4.4: The location and layout of the three microwave detectors AMBER, MIDAS and EASIER, showing the fields of view of the AMBER and MIDAS telescopes [85].

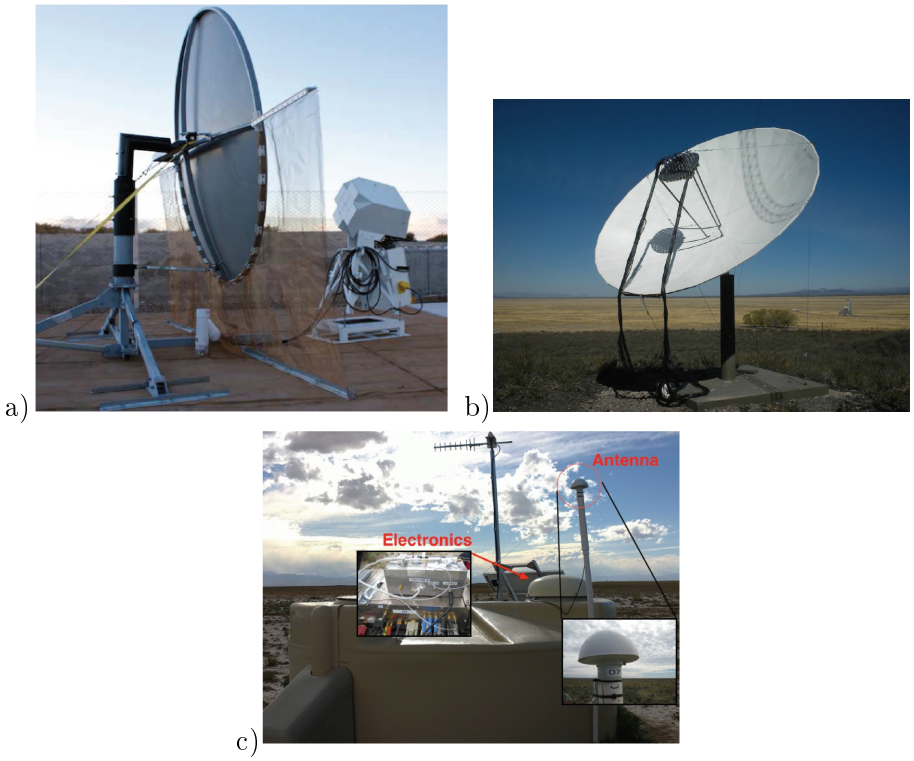

Figure 3.4.5: The two imaging microwave telescopes a) AMBER and b) MIDAS located at the Coihueco and Los Leones FD sites respectively, and c) an EASIER detector installed at a water-Cherenkov tank [85].

4: Cosmic Ray Anisotropies

As described in Chapter 1, cosmic rays are predominantly charged particles. As such, their motion is influenced by the various magnetic fields that permeate the interstellar and intergalactic media. A relativistic particle with energy E (eV) and charge Z moving through a uniform magnetic field B (µG) will be deflected in such a way as to follow a curved path around the magnetic field lines. The radius of this curvature is known as the Larmor radius R_L (parsecs) and is described by the following relationship:

$$R_L = 1.08 \times 10^{-15} \frac{E}{ZB} \sin\theta \tag{4.0.1}$$

where θ is the pitch angle of the particle's motion (i.e. the angle between the particle's motion and the B field lines).

It can be seen from this relationship that the amount of deflection is highly energy dependent, so that the higher the energy of the particle, the greater the value of the Larmor radius. This means that, as cosmic rays propagate through the interstellar medium, they spiral around the magnetic field lines and are scattered by irregularities in the field so that, by the time they reach the Earth, their arrival directions bear little resemblance to those of their origins.

As a result of this directional scrambling, very little information about the source direction is available. What can be studied instead is the overall directionality of these particles, or their deviation from an isotropic flux. The quantity used to indicate the directional properties of the cosmic ray flux is known as its anisotropy, given by:

$$\delta = \frac{I_{max} - I_{min}}{I_{max} + I_{min}} \tag{4.0.2}$$

where I_{max} and I_{min} are the maximum and minimum observed cosmic ray flux intensities respectively. Studies of the anisotropy of the cosmic ray flux at different energies can provide information about the properties of the interstellar medium.

The exception to this restriction is in the case of the very highest energy cosmic rays ($E > 10^{18.5}$ eV), in which R_L is large enough as to make their trajectories approximate straight lines. Research is currently ongoing at detectors such as the

Pierre Auger Observatory investigating the possible sources of these ultra-high energy cosmic rays (UHECR). However, the work presented in this thesis focuses, instead, on much lower energy particles and so we will only touch briefly on this field.

4.1 Sources of Anisotropy

While, as described above, very little information about the cosmic ray source direction is retained during the directional scrambling that the cosmic rays undergo in their propagation through the interstellar medium, the distribution of cosmic ray sources does influence the broad-scale anisotropy of the cosmic ray flux.

As described in Section 1.2, it is understood that galactic cosmic rays are accelerated via the diffusive shock acceleration process in supernova blast waves and, hence, supernova remnants are the primary candidate for cosmic rays of galactic origin. The magnitude of the broad-scale anisotropy observed at Earth contains a contribution from the spatial distribution of these cosmic ray sources within the Galaxy, as well as from the fluctuations in the cosmic ray flux produced by random nearby and/or recent supernova events [86, 87, 88, 89]. Models of the cosmic ray propagation through the Galaxy have shown that the relative magnitude of each of these contributions depends on the spatial distribution of the modelled sources as well as on the size of the modelled magnetised galactic halo. Blasi et al [86] find that it is only when the modelled halo (H) is greater than ~ 4 kpc, does the anisotropy cosmic ray flux due to inhomogeneity in the source distribution become the dominant effect over the small-scale fluctuations due to nearby sources.

There are several additional, more local, extra-terrestrial effects which may contribute towards an anisotropy measurement. Often, these would be considered spurious and be corrected for. However, at the very low energies which are the subject of this research, such effects are of particular interest. The majority of these effects are due to the motion of the Earth with respect to the cosmic ray gas (the Compton-Getting effect), as well as to solar effects such as coronal mass ejections.

4.1.1 Solar Modulation

At the energies investigated in this research, the cosmic ray flux is heavily modulated by heliospheric effects which are controlled by solar activity. The sun undergoes an 11 year activity cycle as well as a 22 year magnetic cycle during which time there are changes in the overall structure and polarity of the heliomagnetosphere. The galactic cosmic ray particles are scattered by irregularities in the interplanetary magnetic field, as well as undergoing adiabatic deceleration as they encounter the expanding solar wind. The heliomagnetosphere itself also affects the gradient and curvature of the galactic cosmic ray flux [67, 90].

Since all these processes are related to the solar activity, the intensity (and integrity) of the galactic cosmic ray flux is inversely correlated with the solar activity cycle. Transient effects such as coronal mass ejections are also more frequent during times of increased solar activity and produce significant disruptions to the galactic cosmic ray flux. To investigate the lowest energy galactic cosmic rays, it is necessary to choose data periods that span the more inactive period in the solar cycle (solar minimum). However, this same cosmic ray flux can also be used to investigate solar phenomena such as Forbush decreases.

Coronal Mass Ejections and Forbush Decreases

Coronal mass ejections (CMEs) are eruptions from the solar atmosphere, expelling plasma from large regions of the corona into the interplanetary medium. The ejected plasma (ejecta) and associated shock may disrupt the cosmic ray flux both locally and at some distance away. A good summary of the present understanding of the characteristics of CMEs is presented by Hundhausen [91].

Decreases in the cosmic ray flux at the Earth's surface were first noted by Forbush [92] and Hess and Demmelmair [93] in the 1930's using ionisation chambers, but it was not until the 1950's [94] that these decreases were shown to originate in the interplanetary medium. The decreases (known as Forbush decreases) are characterised by a sharp drop in the background cosmic ray flux, followed by a slow return to the original intensity over a period of several days. It is now understood that this sharp drop is due to the shock and ejected plasma following a CME [95]. Figure 4.1.1 shows an example of a "classical" Forbush decrease where data from three neutron monitors at Deep River, Kerguelen and Mt Wellington are averaged to show the isotropic intensity (thick black line) as well as the individual station data (thin lines) [95].

4.1.2 Compton-Getting Effect

The other main extra-terrestrial effect on the cosmic ray flux which may give spurious anisotropy results is the Compton-Getting effect, where the motion of the Earth through space produces small Doppler shifts in the cosmic ray particle spectrum in both the approaching and receding directions [96]. If we consider the cosmic ray "gas" to be in equilibrium then, due to the Earth's motion, we will observe an excess in the direction of motion and, likewise, a deficit in the diametrically opposite direction. If we then consider cosmic ray gas to have a streaming velocity (v) with respect to the Earth, the resulting observed anisotropy (δ) as defined in Equation 4.0.2 will be:

$$\delta = (2 + \gamma)\,\frac{v}{c} \tag{4.1.1}$$

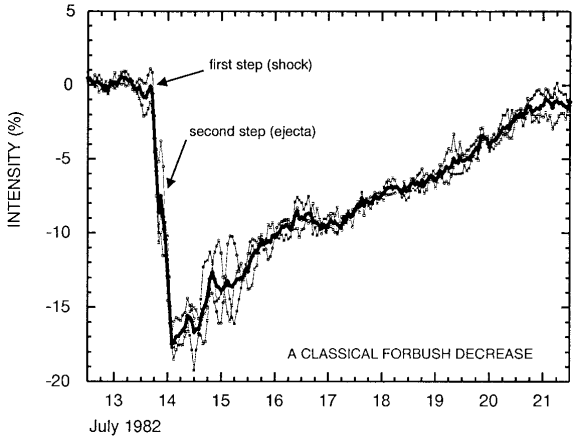

Figure 4.1.1: An example of a "classical" Forbush decreases as observed at three neutron monitor stations (Deep River, Mt Wellington and Kerguelen) [95]. The thick black line indicates the average count rate of the three stations, approximating the isotropic intensity. The characteristic sharp drop in cosmic ray intensity is followed by a slow return to its original level over a period of several days.

where γ is the exponent of the differential rigidity spectrum [97].

There are at least three main motions which may produce such spurious anisotropy results. The first is known as the co-rotation anisotropy [98] and refers to the anisotropy resulting from the motion of the solar magnetic field with respect to the Earth. This anisotropy is rigidity independent up to $\sim 10^{11}$ eV/nucleon with an amplitude of 0.6% and a phase of 18 hours in local solar time. Beyond 10^{11} eV/nucleon, this anisotropy falls to zero [98, 97].

The second effect results from the Earth's orbital motion around the Sun. The Earth's orbital velocity (v) is ~ 30 km.s^{-1} which, considering a differential cosmic ray flux spectrum with $\gamma = 2.7$, would result in an anisotropy of $\sim 0.047\%$ with a phase of 06 hours in local solar time and observable at all energies. However, since this anisotropy has no annual amplitude modulation, it would carry no spurious signal into sidereal time if averaged over a full year [98].

The solar system is also moving through the interstellar medium. This results in a third Compton-Getting anisotropy as the Earth experiences an "interstellar wind" which (in the Earth's reference frame) has a velocity of ~ 21.6 km.s^{-1} from a direction of ~ 16.8 hours in right ascension and -15^{o} declination. Considering the cosmic ray flux in the energy range 10^{13}-10^{14} eV, this would result in an observed anisotropy of 0.033% with a phase of 16.8 hours in local sidereal time [99, 97].

4.2 Analysis Techniques

Depending on the configuration of a cosmic ray detector, there are two main methods of anisotropy analysis which may be performed. Many cosmic ray air shower detectors (such as the Pierre Auger Observatory described in Chapter 3) are large arrays that scan the sky in right ascension. This means that over long periods (provided there are no interruptions in the array's function) the exposure within a given declination band is uniform.

The simplest anisotropy analysis method is to look for variations in the cosmic ray flux as a function of either solar or sidereal time (i.e. a harmonic analysis). In this case the anisotropy is generally described in terms of a Fourier amplitude and phase averaged over the declination band visible to the detector. This method lends itself well to studies of the lower energy cosmic ray flux where there is generally very little directional information available. In particular, the research presented in this thesis will be focusing on this method. In this method it is comparatively simple to test for spurious periodic variations in the flux and there is also the additional benefit that results obtained using this method can be directly compared with results from much earlier cosmic ray experiments. Unfortunately, because the Fourier amplitudes and phases are averaged over the declination band visible to the detector, any resolution of anisotropy as a function of declination is lost [97].

In cases where directional information is available (i.e. the ability to resolve the cosmic ray arrival directions into both right ascension and declination) it is possible to subdivide data sets into declination bands. While this will have the effect of reducing the data in each subset, and hence poorer statistics, over large data sets it is possible to gain a greater understanding of any declination dependency. Such analysis techniques have become more standard in contemporary experiments.

In these studies, it may be advantageous to investigate the anisotropy in coordinate systems other than the standard equatorial coordinates. For example, in the case of anisotropies resulting from the CR's motion through the Milky Way, one may be better served examining the anisotropy in Galactic Coordinates (in which the Galactic Plane is inclined at 62.6 degrees to the Celestial Equator). Since an air shower detector's exposure in declination is non-uniform (variation in detector response as a function of zenith angle), the conversion to Galactic Coordinates results in a complex and non-uniform exposure. The more common technique used in anisotropy analyses in Galactic Coordinates involves the air shower data being binned into uniform bins in Galactic latitude and longitude and a comparison being made of the resulting fluxes with the expected background obtained from the same treatment of a purely isotropic flux.

4.2.1 Harmonic Analysis

In the case of cosmic ray studies, the statistics are similar to the solution of a two-dimensional random walk with equal step lengths and random angles. This problem was first analysed by Lord Rayleigh [100] in relation to sound waves, then further developed by Chapman and Bartels [101] for uses in geomagnetism. Linsley [102] later summarised the application of this technique to the analysis of cosmic ray anisotropies in 1975. The analysis is treated differently in the case of uniform exposure compared with the case of non-uniform exposure.

Uniform Exposure

For a sample of N measurements with phase ψ_1, ψ_2 to ψ_N (where $0 \leq \psi_i < 2\pi$), the relative amplitude r_m and phase θ_m of the m^{th} harmonic of the resultant vector can be calculated by:

$$r_m = \sqrt{a_m^2 + b_m^2} \tag{4.2.1}$$
$$\theta_m = \frac{1}{m} \arctan\left(\frac{b_m}{a_m}\right)$$

where

$$a_m = \frac{2}{N} \sum_{i=1}^{N} \cos(m\psi_i) \tag{4.2.2}$$
$$b_m = \frac{2}{N} \sum_{i=1}^{N} \sin(m\psi_i)$$

The statistical significance of the resultant vector can then be determined by a comparison with that expected from a uniformly distributed series of vectors. As $N \to \infty$, the probability distribution function for the total displacement vector R resulting from N unit steps with randomly distributed angles ψ_i is given by:

$$P(R) = \frac{R}{2N} \exp\left(\frac{-R^2}{4N}\right) \tag{4.2.3}$$

and the probability of obtaining an amplitude greater than or equal to R by a purely random distribution is then found by taking the integral of Equation 4.2.3:

$$P(\geq R) = \exp\left(\frac{-R^2}{4N}\right) \tag{4.2.4}$$

In terms of the relative amplitude $r = R/N$, equations 4.2.3 and 4.2.4 become:

$$P(r) = \frac{r}{2N} \exp\left(\frac{-Nr^2}{4}\right) \tag{4.2.5}$$
$$P(\geq r) = \exp\left(\frac{-Nr^2}{4}\right)$$

Letting $k_0 = \frac{Nr^2}{4}$, the "noise amplitude" can then be defined as the root mean squared amplitude expected from N random steps, which for $k_0 = 1$ becomes:

$$r_{rms} = \frac{2}{\sqrt{N}} \tag{4.2.6}$$

This would seem to suggest that Fourier amplitudes obtained with values above this r_{rms} "noise" level are then statistically significant. However, it must be emphasised that the distribution involved here is broad, and hence there remains a probability that 37% of the amplitudes above r_{rms} may still occur in purely random data [97]. There are also several effects that may contribute towards an apparently significantly high Fourier amplitude, some of which must be considered spurious and removed, or corrected for, before continued analysis. These effects are described in more detail in Section 4.3.

Non-uniform Exposure

In the case of an experiment with non-uniform exposure, in which data have been binned into H time intervals, the Fourier components from Equation 4.2.2 become:

$$a_m = \frac{2}{H} \sum_{i=1}^{H} \frac{n_i}{t_i} \cos(m\psi_i) \tag{4.2.7}$$
$$b_m = \frac{2}{H} \sum_{i=1}^{H} \frac{n_i}{t_i} \sin(m\psi_i)$$

with the resulting amplitude:

$$r_m = \frac{\sqrt{a_m^2 + b_m^2}}{\langle n_i/t_i \rangle} \tag{4.2.8}$$

Letting $w(u, v)$ be the probability per unit area that the end point of a random walk of N steps will lie in the neighbourhood of a point (u, v) in the (a, b) plane, the contours of constant probability become ellipses when the exposure times are non-uniform [97], as opposed to uniform exposure times in which the contours of constant probability are circular. In this case, the probability of obtaining an amplitude greater than or equal to r by a purely random distribution can be approximated

with sufficient accuracy by:

$$P(> r) = \exp\left(\frac{-N(a^2 + b^2)}{4\left\langle n_i^2/t_i^2\right\rangle}\right) \tag{4.2.9}$$

4.3 Spurious Effects and Corrections

In addition to the contributions to the observed anisotropy in the cosmic ray flux described above in Section 4.1, there are also several spurious contributions which must be corrected for. These are generally atmospheric properties which affect the development and propagation of extensive air showers through the atmosphere, as well as those which affect the detector instrument response. The atmospheric modulation of the observed cosmic ray flux is described below, as well as a correction method for the removal of a spurious solar frequency signal from the sidereal frequency.

4.3.1 Atmospheric Modulation

As described in Section 1.4, as cosmic ray particles reach the Earth's atmosphere, they interact with the particles in the atmosphere producing a cascade of secondary particles known as an extensive air shower (EAS). The Earth's atmosphere can be considered to be an absorber with variable thickness which affects the development and attenuation of EASs. On average, the atmosphere has a thickness of around 1000 $\mathrm{g.cm^{-2}}$, with a $\sec\theta$ increase in the mass absorption for showers inclined at zenith angle θ.

In general, variations in atmospheric pressure are irregular over the time scale of days and, hence, would mostly average out for observations made over sufficient time periods. However, there are two main periodic variations in the atmospheric pressure which must be corrected for.

The first is a diurnal variation that results from the heating of the atmosphere. The dominant harmonic in this variation is the second harmonic, producing a twice diurnal variation in atmospheric pressure of around 2 hPa per day.

The second variation is the seasonal variation in atmospheric pressure. In summer, the sub-tropical ridge of high pressure moves further towards the pole and so, at the latitude of the Pierre Auger Observatory (see Chapter 3), the atmospheric pressure will be higher on average in summer than in winter, when the ridge moves further towards the equator.

The temperature of the upper atmosphere also affects air shower development since it affects the atmospheric density. However, since there are very few measurements of this upper temperature, it is not usually corrected for.

However, the temperature fluctuations at ground level can also affect the detector's instrumental response to incident air showers. While this effect may be very small when compared with that of the pressure variations, it may still produce a significant modulation which should be corrected for.

While all these variations occur on the solar time scale (either diurnal or annual), they may also produce spurious anisotropies in sidereal time. This will be described in further detail in the next Section, along with correction methods. In order to reliably correct for these modulations, an integral multiple of a full solar year of data is required.

4.3.2 Corrections

Antisidereal Analysis

Farley and Storey developed the method of using antisidereal time to correct for spurious solar effects in the sidereal component in 1954[103]. The method assumes that variations in the cosmic ray flux have only two frequency components: a solar component containing atmospheric temperature and pressure effects, and a sidereal component representing the true cosmic ray anisotropy. The observed cosmic ray flux intensity can then be expressed as the sum of these components:

$$I(t) = \bar{I} + I_0 \cos 2\pi \left(Nt - \phi_0\right) + I_1 \cos 2\pi \left[(N+1)t - \phi_1\right] \tag{4.3.1}$$

where $\bar{I}$ is the mean intensity, I_0 and ϕ_0 are the solar amplitude and phase respectively, and I_1 and ϕ_1 are the sidereal amplitude and phase. N is the number of solar days in a year, so it then follows that there are $(N+1)$ sidereal days in a year.

If we consider an annual modulation in the solar flux intensity such that:

$$I_0 = I_0' \left[1 + A \cos 2\pi \left(t - \alpha\right)\right] \tag{4.3.2}$$

then, substituting this back into Equation 4.3.1, we get:

$$\begin{aligned} I(t) &= \bar{I} + I_0' \cos 2\pi \left(Nt - \phi_0\right) + I_0' A \cos 2\pi \left(t - \alpha\right) \cos 2\pi \left(Nt - \phi_0\right) \\ &\quad + I_1 \cos 2\pi \left((N+1)t - \phi_1\right) \\ &= \bar{I} + I_0' \cos 2\pi \left(Nt - \phi_0\right) + I_1 \cos 2\pi \left[(N+1)t - \phi_1\right] \\ &\quad + \frac{I_0' A}{2} \cos 2\pi \left[(N+1)\,t - \phi_0 - \alpha\right] \\ &\quad + \frac{I_0' A}{2} \cos 2\pi \left[(N-1)\,t - \phi_0 + \alpha\right] \end{aligned} \tag{4.3.3}$$

where we can see that a solar modulation produces two spurious components with

equal amplitude oriented symmetrically about the solar vector. One of the components corresponds to a spurious component in sidereal time, while the other component corresponds to a time frame in which a year has $(N-1)$ days, which is termed "antisidereal" time. Antisidereal time is a physically meaningless quantity (corresponding to the Earth traveling in the opposite direction around the Sun) and has a phase chosen so that, like sidereal time, it is equal to solar time at the September equinox.

From Equation 4.3.3 we see that the observed sidereal harmonic vector will then be a sum of both the "true" sidereal vector and the spurious component produced by the modulation in the solar flux intensity. If data from an integral number of full years are analysed, this spurious component may then be removed by reflecting the antisidereal component in the solar vector and subtracting it from the observed sidereal vector [103]. Figure 4.3.1 shows the various vector components displayed on a harmonic dial [97].

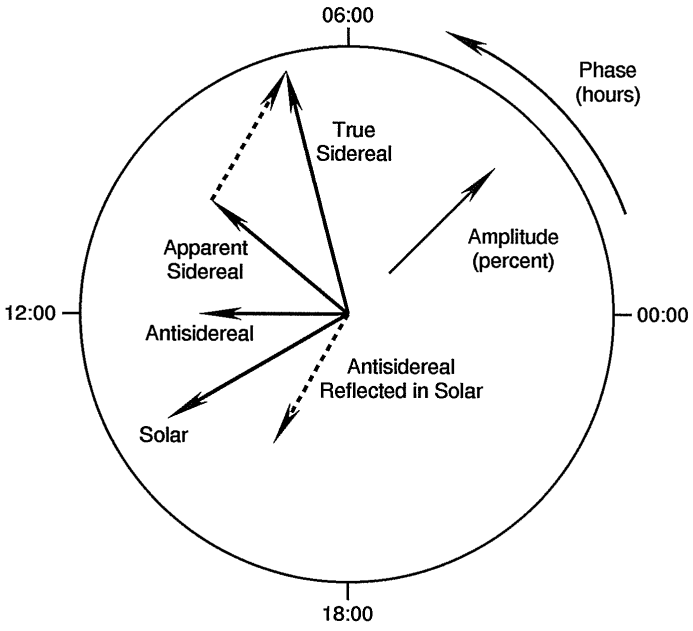

Figure 4.3.1: The various vector components described in Equation 4.3.3. The "true" sidereal component may be determined by reflecting the antisidereal component about the solar vector then subtracting it from the observed sidereal vector [97].

To this stage, it has been assumed that the solar component is only modulated in amplitude. However, if the solar component is also modulated in the phase, then this process becomes significantly more complex and the simple geometry described

above no longer holds. If we consider a solar phase modulation:

$$\phi_0 = \phi_0' \left[1 + B \cos 2\pi \left(t - \beta\right)\right] \tag{4.3.4}$$

then the resulting intensity has harmonic components at all frequencies $\omega_i = 2\pi \left(N + i\right)$, where $i \in \mathbb{Z}$ and can be expressed as [97]:

$$I(t) = \bar{I} + \sum_{i=-\infty}^{\infty} I_i \cos 2\pi \left[\left(N + i\right) t - \phi_i\right] \tag{4.3.5}$$

To determine whether or not an annual solar phase modulation is significant, the presence of other harmonic components can be tested for, such as components in the time frames corresponding to $i = \pm 2$ ("ultra-sidereal" or "ultra-antisidereal" time). Formulae for calculating sidereal, antisidereal, ultra-sidereal and ultra-antisidereal times are provided in Appendix A.

4.4 Measured Anisotropies

4.4.1 Low energy cosmic ray anisotropies

Below around 10^{11} eV, the cosmic ray flux is heavily modulated by solar activity (as described above in Section 4.1.1). The majority of low energy cosmic ray data are obtained from the penetrating muon component and measured by muon detectors beneath the Earth's surface, or by surface neutron monitors. Nagashima, Fujimoto and Jacklyn [46] summarise the results of underground muon detection experiments at Hobart and Sakashita, and a surface muon detection experiment at Nagoya in comparison with higher energy cosmic ray air shower results from Mt Norikura. Figure 4.4.1 shows the daily sidereal variation (in local sidereal time) at each of the locations, following a correction for the solar modulation, along with the median energy and the latitude of the central viewing direction.

From Figure 4.4.1 it can be seen that the sidereal daily variation contains relatively sharp peaks and/or deep troughs with centres at almost 6 and 12 hours respectively. The peaks become less defined in the northern telescopes while, likewise, the troughs become less defined in the southern telescopes. It is argued that these results indicate the superposition of two different modulations in arrival direction. The first is a galactic anisotropy with the same form as observed by small air showers with energies around 10^4 GeV and characterised by a deficit at around 12 hours local sidereal time at a declination of around 20° but confined in a cone with a half opening angle of $\sim 57°$, so mainly observable only in the northern hemisphere. As this "loss cone" anisotropy can be observed at even the lower energies (around 60 GeV),

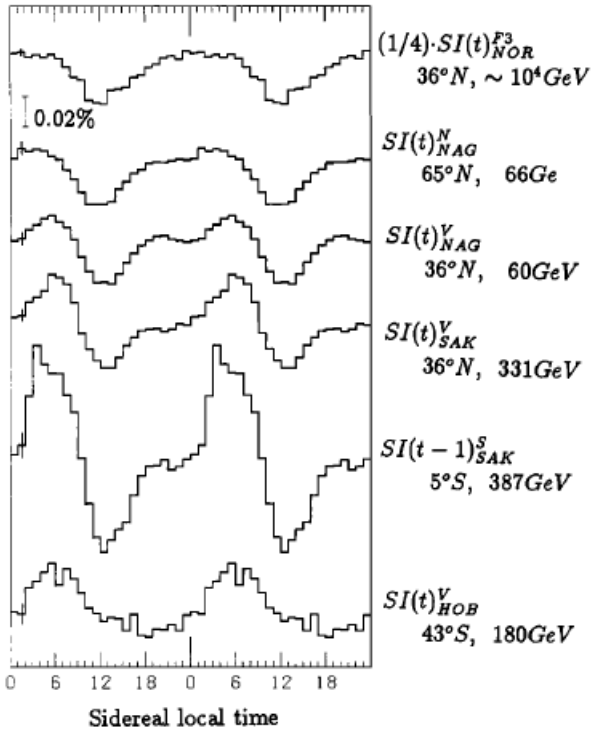

Figure 4.4.1: Shows the variation in local sidereal time from muon experiments conducted at Mt Norikura, Nagoya, Sakashita and Hobart. The median energy and latitude of the central viewing direction for each telescope are also shown [46].

this indicates that it undergoes negligible heliomagnetic modulation [46, 104, 105]. The second anisotropy is a directional excess at around 6 hours local sidereal time, declination around $-24°$ and confined to a cone with a half opening angle of $\sim 68°$. However, it is only observed in the energy region below $\sim 10^4$ GeV. As the direction of this second anisotropy appears to coincide with the direction of the heliomagnetotail ($\sim 68°$), it is known as the "tail-in" anisotropy. It is also then expected that this anisotropy would maximise near the December solstice, when the Earth is nearest to the heliomagnetotail [46].

4.4.2 Mid energy cosmic ray anisotropies

The Tibet Air Shower Array (Tibet ASγ), IceCube and Milagro (described in Section 2.3) detectors have reported anisotropies in the mid energy range.

The Tibet ASγ data, shown in Figure 4.4.2, show the tail-in and loss-cone anisotropies both still evident at a modal energy of 3 TeV. The data also show a third anisotropy component near the Cygnus region [106]. Figure 4.4.3 shows the same data plotted in solar time, with an excess evident at around 06 hours local solar time and a deficit approximately 12 hours opposite, which is consistent with the expected Compton-Getting anisotropy due to the Earth's motion around the Sun. The amplitude of this solar time fluctuation is of the order $\sim 0.04\%$.

The Milagro results display data from a comparable energy range to Tibet ASγ. Figure 4.4.4 a) shows a harmonic fit to the fractional difference from isotropy observed by Milagro over the period 2000-2007 with a median energy of 6 TeV. The position of the galactic equator and north pole are superimposed (black line and dot respectively). Figure 4.4.4 b) then shows the one-dimensional anisotropy analysis of the data from all declinations over the same time period. The sidereal, antisidereal and universal solar time anisotropies are plotted as well as the Compton-Getting anisotropy expected due to the Earth's motion around the Sun with a maximum at 06 hours in local solar time [53].

While both Milagro and Tibet ASγ observations span the Northern Hemisphere sky, the IceCube detector at the South Pole investigates the mid energy anisotropies over the Southern Hemisphere sky. Figure 4.4.5 a) shows the relative intensity of the cosmic ray flux observed by IceCube with a median energy of 20 TeV (slightly higher energy than Milagro and Tibet ASγ) while Figure 4.4.5 b) shows the one dimensional projection of the sidereal time anisotropy plotted in right ascension as well as the antisidereal modulation [63].

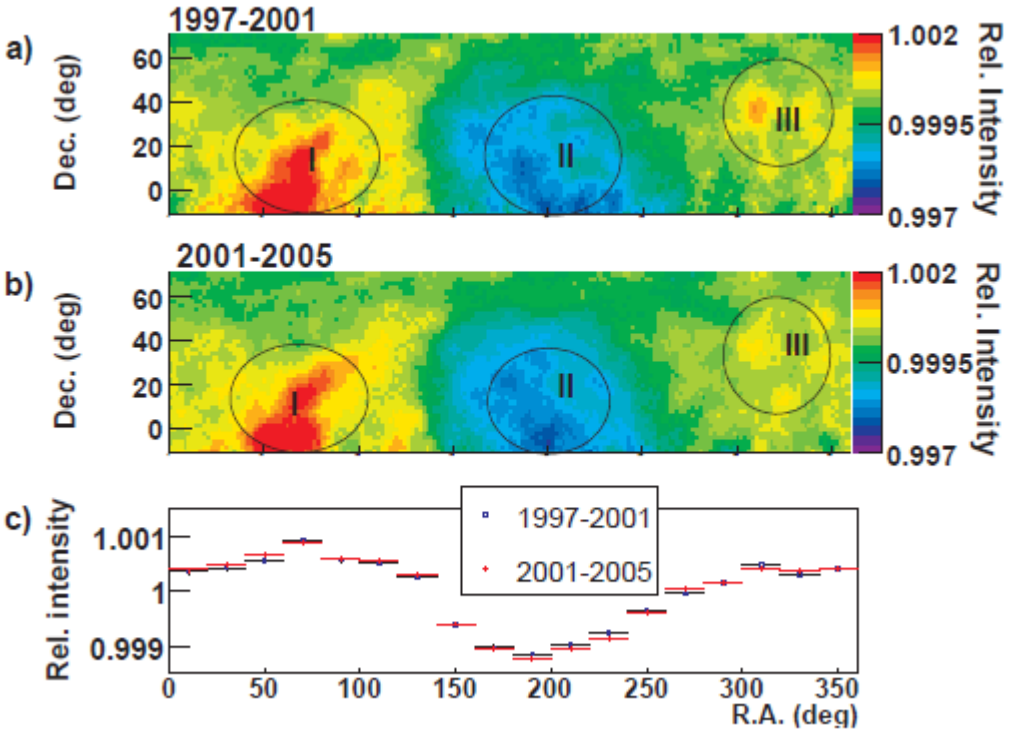

Figure 4.4.2: Relative intensity of the cosmic ray flux as observed by Tibet ASγ over the periods a) 1997 to 2001 and b) 2001 to 2005, with a modal energy of 3 TeV. Circles I and II show the tail-in and loss-cone anisotropy regions, while circle III indicates another anisotropy component near the Cygnus region. Panel c) shows the one-dimensional projection of the 2D maps in right ascension [106]. Note that right ascension is not plotted on the conventional reverse scale.

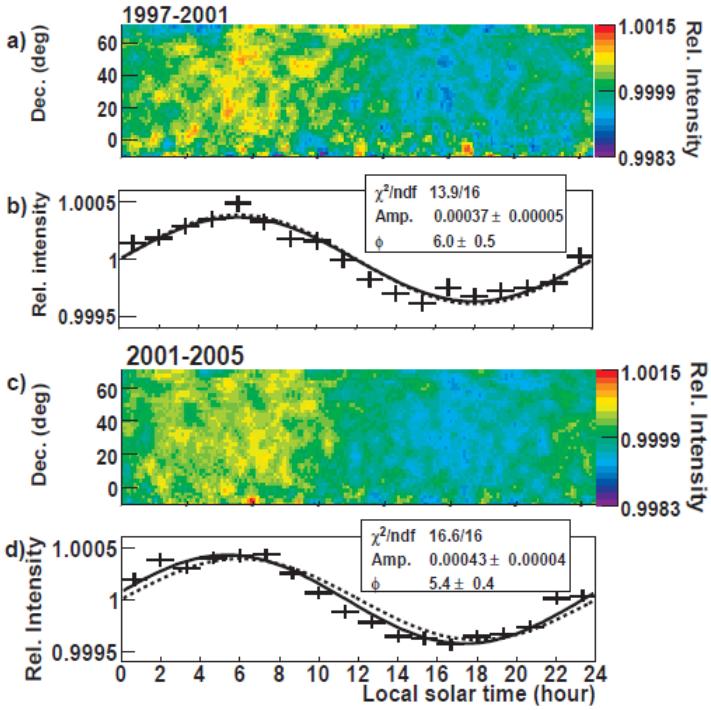

Figure 4.4.3: Relative intensity of the cosmic ray flux observed by Tibet ASγ as a function of declination in local solar time at a modal energy of 10 TeV for a) 1997 to 2001 and c) 2001 to 2005. Panels b) and d) display the one-dimensional projections of a) and c) respectively and show an excess evident at around 06 hours local solar time which is consistent with the expected Compton-Getting anisotropy resulting from the Earth's motion around the Sun [106].

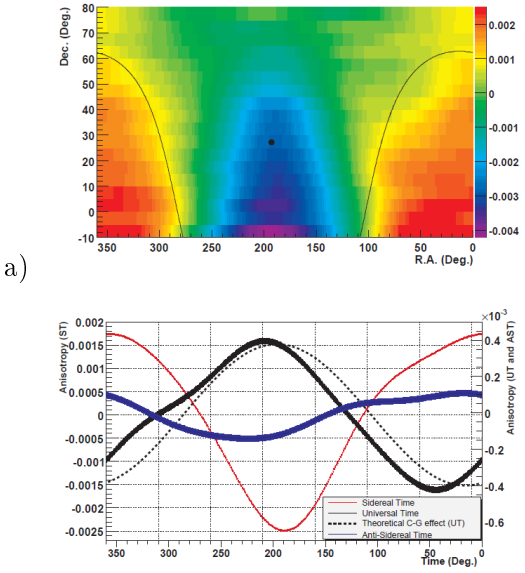

Figure 4.4.4: Shows a) a harmonic fit to the observed fractional intensity fluctuation from isotropy at Milagro over the years 2000-2007 with the position of the galactic equator and north pole superimposed (black line and dot respectively). The 1-dimensional projection of the analysed anisotropies are then plotted in b) in sidereal time (red) and universal solar time (black) as well as in antisidereal time (blue). The expected Compton-Getting anisotropy component in universal solar time arising from the Earth's motion around the Sun is also plotted (black dotted). The width of each of the curves indicates the magnitude of the statistical error [53].

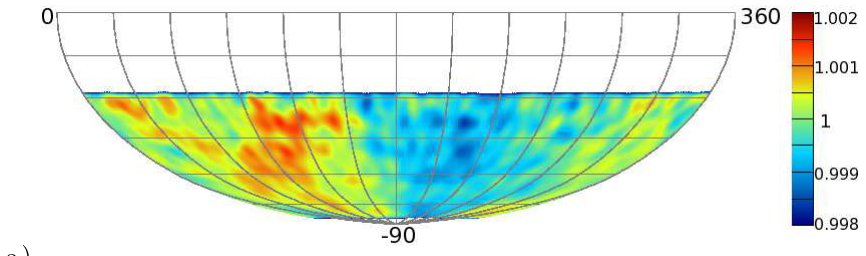

a)

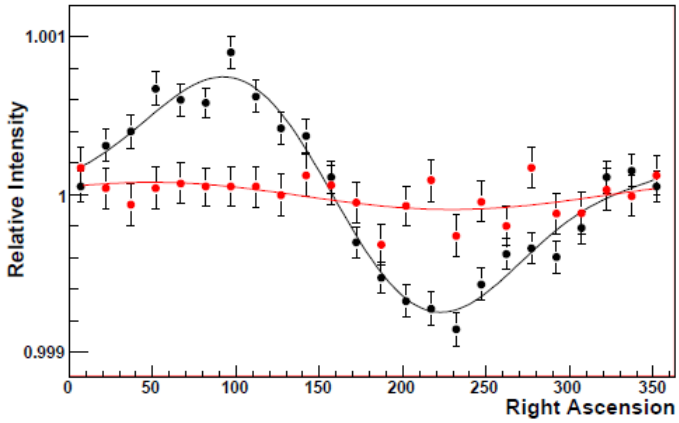

b)

Figure 4.4.5: Shows a) the relative intensity of the cosmic ray fluctuations observed at IceCube in equatorial coordinates with a median energy of 20 TeV, and b) the one-dimensional projection of the relative intensity in sidereal time (black) as well as the antisidereal modulation (red) [63]. Note that right ascension is not plotted on the conventional reverse scale.

4.4.3 High energy cosmic ray anisotropies

The EAS-TOP detector (described in Section 2.2.9) was sensitive to secondary particles originating from primary energies between $10^{13} - 10^{16}$ eV, spanning the "knee" of the cosmic ray energy spectrum. Aglietta et al [44] describe the broad scale anisotropies observed in the solar, sidereal and antisidereal frequencies at two mean energies: 110 TeV and 370 TeV. Figure 4.4.6 a) and b) show these anisotropies observed at 110 TeV and 370 TeV respectively. It can be seen that the solar modulation is comparable at each of the two energies, while the sidereal modulation increases in amplitude at the higher energy with a phase at around 13.5 hours rather than around 0.5 hour. The signal in the antisidereal frequency also shows an increased amplitude at the higher energy.

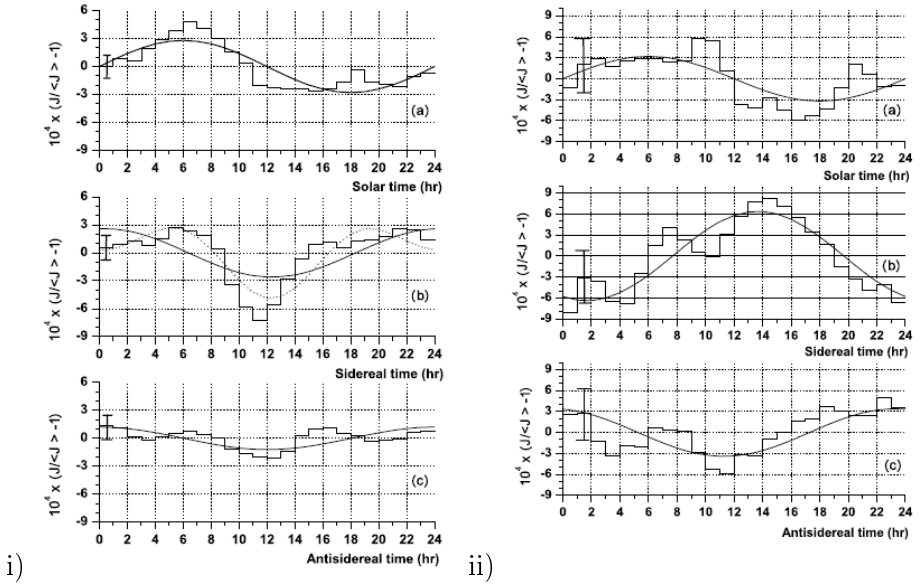

Figure 4.4.6: The anisotropy observed by the EAS-TOP detector in the a) solar, b) sidereal and c) antisidereal frequency at mean energies of i) 110 TeV and ii) 370 TeV with the fitted first harmonic curve (as well as the second harmonic in the sidereal time curve) superimposed. The statistical uncertainty is shown in the first time bin [44].

The IceTop detector (described in Section 2.3.4) is sensitive to yet higher energy cosmic ray events with energies ranging from 100 TeV to 1 EeV. Aarsten et al [107] describe the recent broad scale anisotropies observed by IceTop at two median energies: 400 TeV (low energy) and 2 PeV (high energy). Figure 4.4.7 a) shows the relative intensities observed in each energy range along with their statistical significance, while Figure 4.4.7 b) shows the one-dimensional projection of these relative intensities. It can be seen that the anisotropies observed in these results are significantly different to those at lower energies.

a)

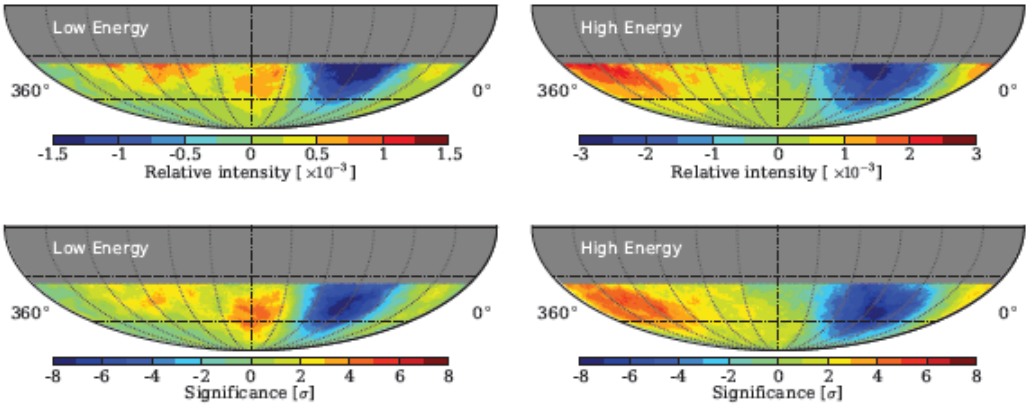

b)

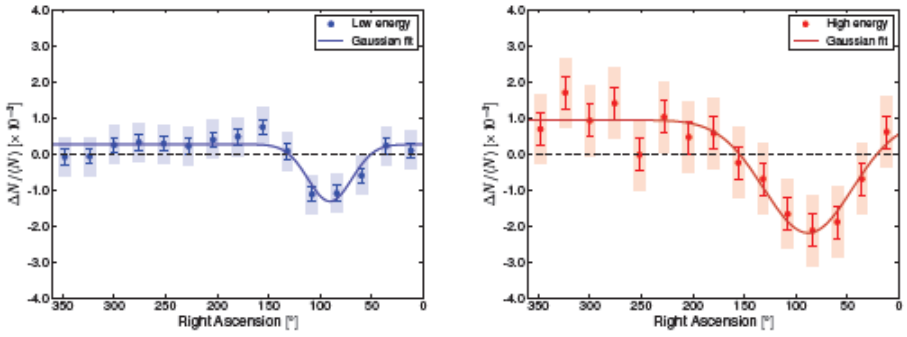

Figure 4.4.7: a) The relative intensity of the cosmic ray flux observed by the IceTop detector in the low and high energy data ranges (median energy 400 TeV and 2 PeV respectively) as well as the statistical significance. b) The one-dimensional projection of these relative intensities for the low and high energy data ranges [107].

At still higher energies ($E > 10^{18.5}$ eV), due to the increased radius of gyration R_L described at the start of this Chapter, it becomes possible to study the anisotropy of cosmic rays with respect to point sources (rather than the broad scale studies described in this Section). However, as this work focuses on the lower energies and broad scale anisotropies, this technique will not be described here.

5: Extraction of Low Energy Cosmic Ray Data

The Pierre Auger Observatory's surface detector (SD) consists of 1660 water-Cherenkov stations placed in a 1.5 km spaced triangular array covering an area of around 3000 km^2. Each of these stations is instrumented with 3 photomultiplier tubes (PMTs) that measure the Cherenkov light produced as charged particles from cosmic ray air showers pass through the water in the tank. The surface detector of the Pierre Auger Observatory is described in more detail in Section 3.1.

As part of the SD calibration procedure, histograms of the ungated pulse heights and charges measured at each PMT are produced for each SD station on a regular basis. This chapter describes the production of these histograms as part of the calibration process and how they are used in this research to investigate the properties of the cosmic ray flux at low energies.

5.1 Calibration Histograms

Upon the triggering of a T3 event in the Pierre Auger Observatory surface detector, all SD stations involved in the trigger transmit event and calibration data to the central data acquisition system (CDAS). Amongst the calibration data are histograms of the measured pulse heights and charges for each individual PMT as well as for the sum of all 3 PMTs. These histograms are regularly produced every 61 seconds but are only transmitted to CDAS in the event of the station being involved in a T3 trigger.

The pulse height and charge histograms present data measured in fast analogue to digital converter (FADC) channels and integrated FADC channels, and are limited to 250 bins and 1000 bins respectively. Neither histogram contains an overflow bin, although the addition of an overflow bin into the calibration data is currently being implemented for a subset of the stations. Examples of both the charge and pulse height histograms are shown in Figure 5.1.1 for PMT 1 of station 101 ("Lautaro").

The second peak of the charge histogram (at around channel 180) is used in the calibration procedure, as described in Section 3.1.2, to determine the charge produced by a vertical central and through-going muon, known as a "vertical equivalent muon" (VEM). The position of this peak Q_{VEM}^{peak} is related to the value of 1 VEM by the

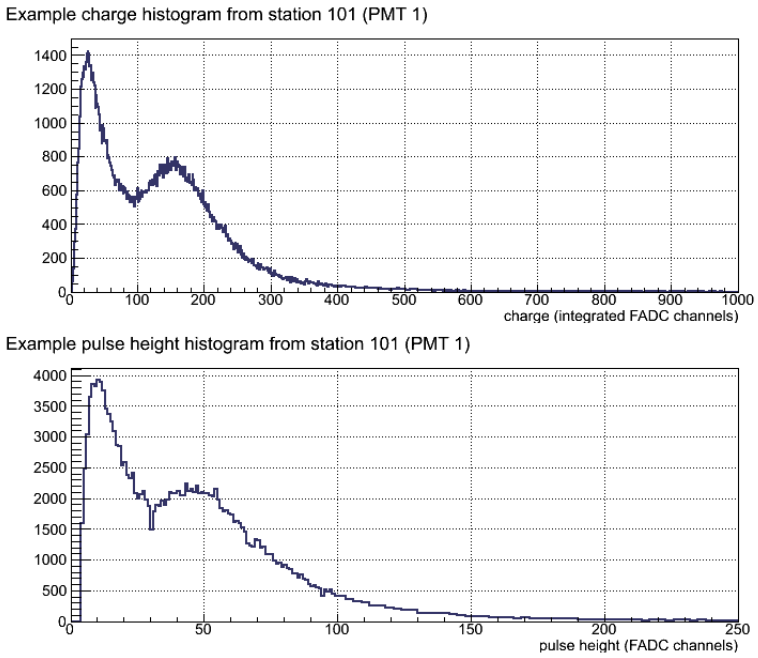

Figure 5.1.1: Example charge (top) and pulse height (bottom) histograms produced by PMT 1 of station 101 ("Lautaro"). The charge histograms span 1000 integrated FADC channels while the pulse height histograms span 250 FADC channels. It should be noted that neither histogram contains an overflow bin.

relationship $Q^{peak}_{VEM} = 1.03 \pm 0.02$ VEM *[69]*. The position of the corresponding peak in the pulse height histogram I^{peak}_{VEM} is used as the threshold unit in the local station trigger.

The current implementation of the scaler mode of the Pierre Auger Observatory measures the counting rate between FADC channels 3 and 20 (see Section 3.1.5). The research presented in this thesis aims to investigate the counting rate variation across the whole charge histogram; covering the region studied using scaler mode as well as those regions which include the unaccompanied muons and higher energy small showers. In order to pursue this study, the charge histograms must be calibrated such that they are comparable across all stations of the SD. Additionally, the energies of the primary cosmic ray particles contributing to the signals presented in the charge histograms must be determined. The simulations performed to investigate the various contributions to the charge histograms are described in the next chapter (Chapter 6).

5.2 Data Extraction and Cleaning

The raw calibration data are stored in a database amongst the raw SD event data; catalogued by year, month and date. The charge histogram data are extracted using

the Offline software framework which is described in detail in Argirò (2007)[108]. These raw histograms contain 1000 bins, each representing 1 integrated FADC channel.

In addition to the raw histogram data, the integration time, base and peak position are also output. The integration time is simply the difference between the start and end time recorded for each calibration period and the peak position is calculated within the Offline module through a quadratic fit to the second peak of the charge histogram.

5.2.1 Conversion from Integrated FADC channels to MeV

The relativistic muon energy loss can be approximated as 2 MeV per g/cm^2. Hence, given a water depth of 1.2 m in each water-Cherenkov tank of the SD (see Section 3.1.1), the energy deposited by a vertical, central and through-going muon (VEM) can be determined in units of MeV. That is, 1 VEM is taken to be equivalent to 240 MeV of deposited energy. The charge histograms may then be calibrated such that the bins are in units of MeV using the relationship between the peak position (in integrated FADC channels) and the energy deposited by 1 VEM.

This calibration was performed by re-binning the histogram data such that each bin now spanned 20 MeV of deposited energy. The bin contents were output as a counting rate (counts.s^{-1}) by dividing the total number of counts in each 20 MeV bin by the integration time. Figure 5.2.1 shows an example of the resultant charge histogram produced after the re-calibration process. By calibrating all the charge histograms in standard units of deposited energy (MeV), the data become comparable across the whole SD array.

The resulting histograms span deposited energies to 1500 MeV. However, due to the truncation of the raw histograms at 1000 integrated FADC channels, and the variation in gain of the various SD PMTs, these final bins contain much lower statistics than the remaining bins. The number of non-zero counting rates measured in each 20 MeV bin for January 2006 (all stations) is shown in Figure 5.2.2.

5.2.2 Cleaning

It was discovered early on that the histogram data do not contain exactly 61s of data. Rather, due to a bug in the local station software, the electronics instead store multiples of 61s. Figure 5.2.3 shows a superposition of all the charge histograms produced by PMT 1 of station 101 for January 2006 in which this multiple effect is clearly visible.

In order to identify those histograms belonging to multiples of the expected 61s time interval, the counting rate in the 20 MeV bin surrounding 240 MeV was anal-

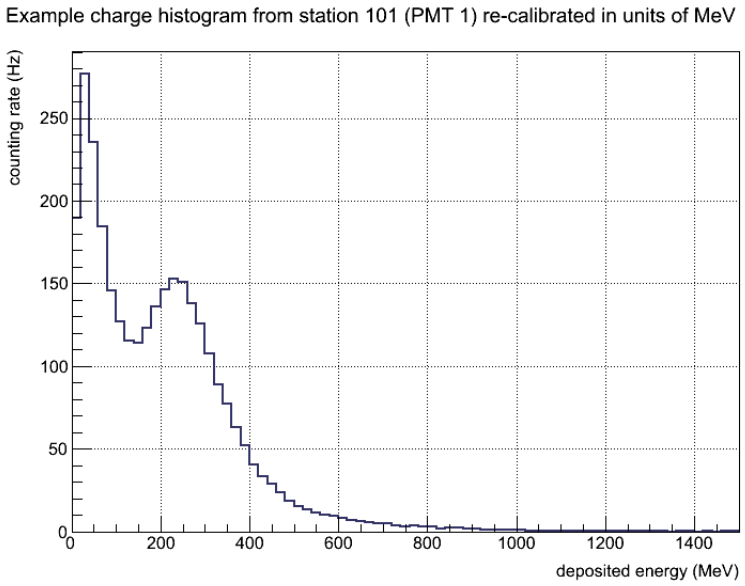

Figure 5.2.1: Example charge histogram following the re-calibration into units of deposited energy (in MeV). The resulting histograms span deposited energies to 1500 MeV in bins of 20 MeV.

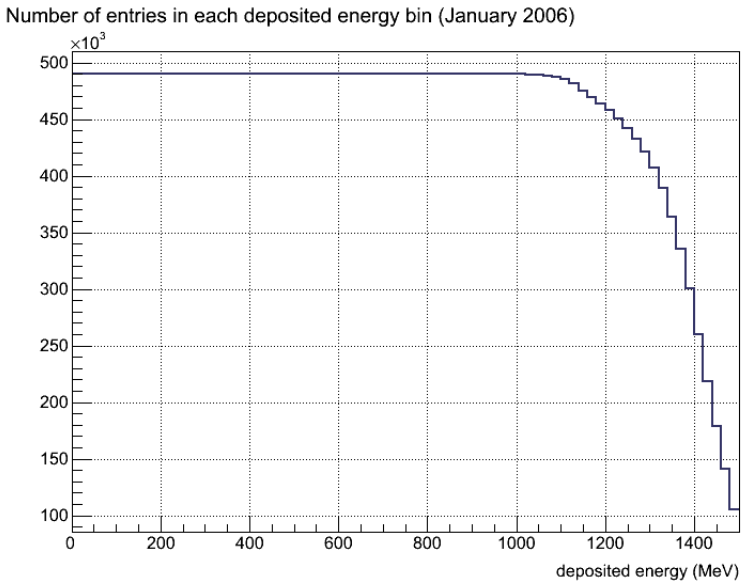

Figure 5.2.2: The number of non-zero counting rates measured in each 20 MeV bin over January 2006. The sharp drop in statistics above 1000 MeV is clearly visible.

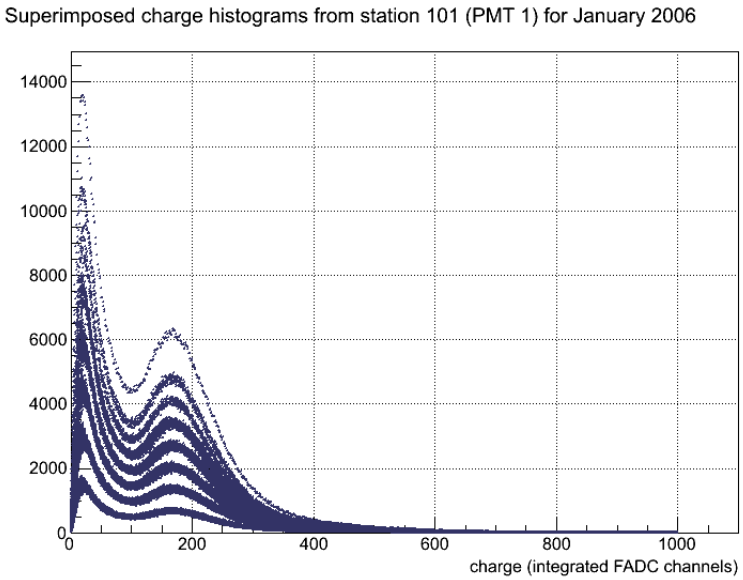

Figure 5.2.3: Superposition of all the charge histograms produced by PMT 1 of station 101 during January 2006. The clear banding is due to a bug in the local station software that randomly stores integer multiples of 61s of data.

ysed. In this deposited energy region, the separation between multiple time interval data is quite clear. Distributions of the counting rate in this bin were produced individually for each PMT of each SD station. An example of these distributions is shown in Figure 5.2.4 for PMT 1 of station 101 for the January 2006 period. This multiplication factor was determined by using the ratio between the mean positions of each peak, and was stored with the histogram data to allow either the inclusion or exclusion of histograms in which the time multiple is not equal to 1.

Checks were also performed of the integration time which identified cases in which the start and end times of the calibration period had been misrecorded. After identifying the relevant multiplication factor as described above, the distribution of the counting rates for each PMT of each station in the 20 MeV bin surrounding 240 MeV was analysed. A cut was made in which only stations which had a quoted integration time of 61 s were investigated. Another error in the local station software caused blocks of 5s intervals to be occasionally lost. These distributions of the counting rates were then used to identify histograms in which this was the case. All histograms with integration times less than 61 s were removed from further analysis.

5.2.3 Sub-array selection

Like the data obtained from the scaler mode, the charge histogram data are suitable to study transient solar effects such as Forbush Decreases (described in Section 4.1.1). However, since the Pierre Auger Observatory has been in operation since 2004, a long

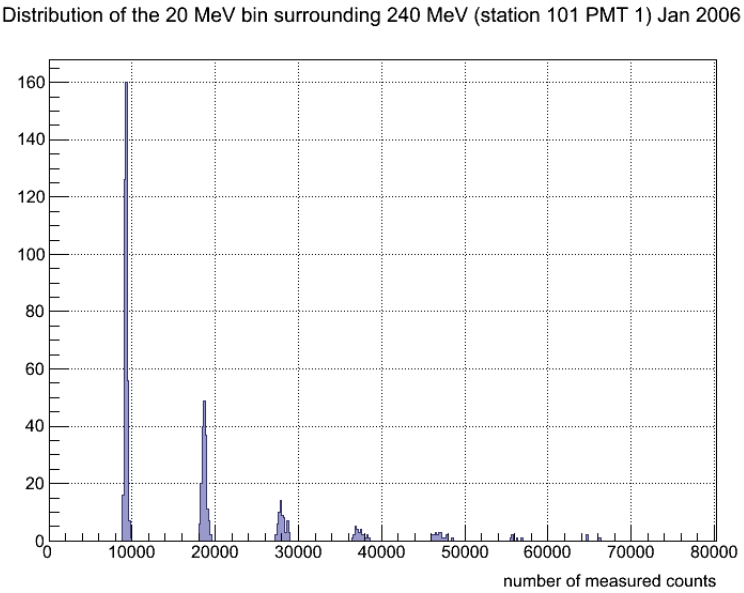

Figure 5.2.4: An example of the distribution of the 20 MeV deposition energy bin surrounding 240 MeV for station 101 (PMT 1) during January 2006. The clear peaks are used to identify the multiplication factor for the number of 61 s periods belonging to each individual histogram.

term study of the solar and sidereal anisotropies at the energies measurable by the charge histograms is also possible. Ideally, such a study would be conducted over a period of low solar activity to minimise spurious signals. The 2005 period contains relatively high solar activity, as does the end of 2010 and 2011. However, during the 2006 to 2009 period the Sun remained at relatively low activity levels. For this reason, a sub-array of the surface detector was selected that was in constant operation for the whole period of the start of 2006 to the end of 2010. The resulting sub-array satisfying this initial condition consisted of 583 SD stations and is shown in Figure 5.2.5a.

In addition to this first cut on the operation of each station, the behaviour of each of the operational stations during this period was also required to be stable. Distributions of the counting rates in the 20 MeV deposition energy bin surrounding 240 MeV were analysed and stations that showed an unusually high variance were cut from the selection. These cuts were quite harsh, removing any PMT with a standard error of 0.1 counts per second, which resulted in a sub-array of only 1178 PMTs (from 395 stations). This cut effectively removed all misbehaving stations, including those still undergoing their settling-in period in which the counting rates can fluctuate significantly, as well as any "raining" PMTs (described in [109, 110]). The final sub-array used in the analysis is shown in Figure 5.2.5b.

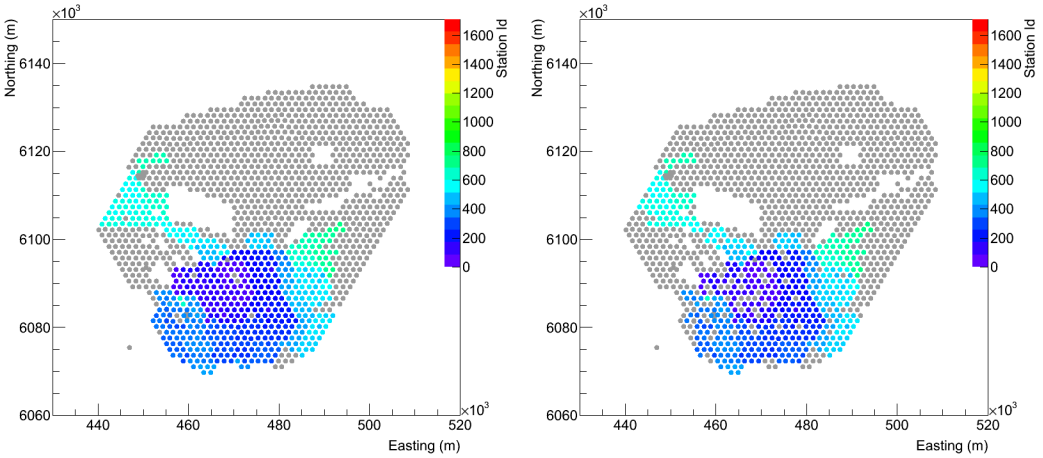

(a) **(b)**

Figure 5.2.5: The layout of the surface detector of the Pierre Auger Observatory showing the sub-arrays produced by cuts on a) the operational period, and b) PMT behaviour of those stations surviving cut a).

5.3 Atmospheric Corrections

As described in Section 4.3, atmospheric conditions can affect the development of cosmic ray air showers and, hence, produce spurious results in a subsequent anisotropy study. The atmospheric conditions of the Pierre Auger Observatory are constantly monitored by weather stations located at each of the four fluorescence detector sites and at the central laser facility (CLF). The correction of the charge histogram data to account for the atmospheric conditions was performed in two stages. The first stage corrected for the twice-diurnal rate variation due to atmospheric pressure fluctuations while the second corrected for temperature variations.

5.3.1 Weather Data

Data on the atmospheric conditions are collected at each of the four fluorescence detector sites (Los Leones, Los Morados, Loma Amarilla and Coihueco) and at the central laser facility (CLF). Information from the weather stations located at these sites is stored in a set of ASCII files (available at `https://web.ikp.kit.edu/keilhauer/DB_Ascii_tables/`) and contain the following data:

- time of measurement (this is given in both day, hour, minute format in UTC as well as the GPS start and end times of each measurement),
- the altitude of weather station (m),
- temperature (K),

- pressure (hPa),
- relative humidity,
- average wind speed (m/s),
- atmospheric depth (g/cm^2), and
- air density (kg/m^3).

In addition, atmospheric profile data of the variations with atmospheric height, obtained during weather balloon launches, are also stored in ASCII files at this location. The knowledge of the atmospheric conditions as a function of height is of extreme importance in the reconstruction of fluorescence detector events.

Only the pressure and temperature are used in the atmospheric corrections of the charge histogram data. A data set was created in which the average temperature and pressure values from each of the active weather stations are stored in half-hourly time intervals. Figure 5.3.1 shows the temperature and pressure fluctuations over January 2006. The diurnal variation in temperature as well as the twice diurnal variation in atmospheric pressure are clearly visible. This data set was then used to assign temperature and pressure values corresponding to each charge histogram during the atmospheric correction process.

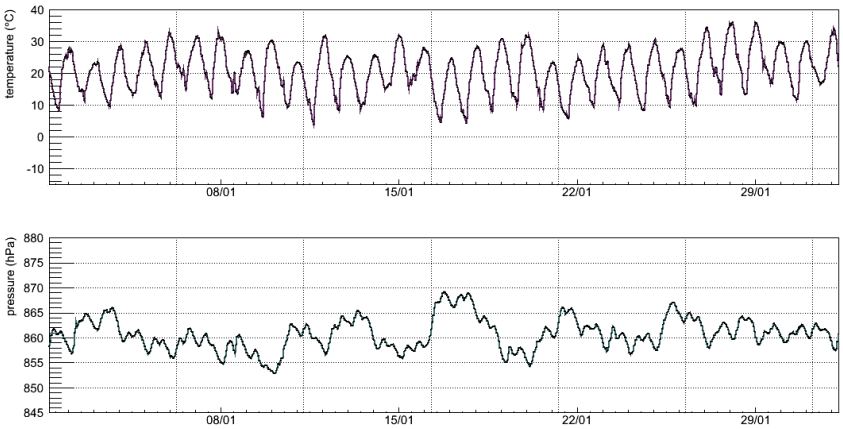

Figure 5.3.1: Atmospheric temperature and pressure measurements plotted over January 2006. The dates are given with respect to midnight on the 1st of January 2006 (UTC).

5.3.2 Barometric Correction

The atmospheric pressure has the greatest influence on the detector counting rate fluctuations. For low energy showers, increased atmospheric pressure results in cosmic ray air showers developing higher in the atmosphere and, hence, less particles

reaching ground level. The inverse correlation between atmospheric pressure and particle counting rate is shown in Figure 5.3.2 in which both the counting rate and corresponding pressure are plotted as a function of time (reversed axis for pressure).

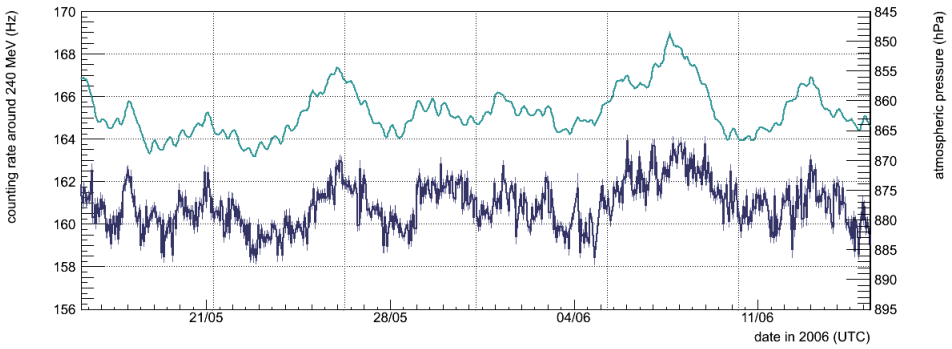

Figure 5.3.2: Timeseries of the counting rate in the 20 MeV bin around 240 MeV *(dark blue)* and atmospheric pressure *(green)*. The inverse correlation between these two values is clear. Note that the pressure is plotted on a reversed axis.

The magnitude of any barometric effect is expected to be dependent on the altitude of the measurement, since experiments located at higher altitudes are generally nearer the depth of shower maximum and hence measure a greater number of cascade particles. Experimental values of the barometric coefficient from various neutron monitor and muon detectors are provided by the Neutron Monitor Database (NMDB) (available at `http://www.nmdb.eu/?q=node/196`). From these results, at the altitude of the Pierre Auger Observatory (1420 m), we therefore expect the barometric coefficient for unaccompanied muons to be between ~ -0.15 % per hPa and ~ -0.24 % per hPa, being the coefficients measured from the Nor Amberd Sevan and the Yerevan SEVAN experiments at altitudes 1000 m and 2000 m respectively [111].

The barometric correction of the charge histogram data was performed individually at each deposition energy bin of each PMT of each SD station in the sub-array. A simple linear fit to the counting rate and pressure data was used to produce a barometric coefficient in counts.s^{-1} per hPa. Figure 5.3.3 shows an example of such a fit for PMT 1 of station 101 for the 2006 period in the bin surrounding 240 MeV (1 VEM). By converting these barometric coefficients for each energy deposition bin into units of % per hPa, the behaviour of the pressure coefficient values can then be compared over the full charge histogram energy range, and across the whole sub-array.

Figure 5.3.4 shows the average pressure coefficients in each energy bin calculated for 2006. It can be seen that that the barometric coefficient around 240 MeV is around-0.18 % per hPa, which is consistent with that of unaccompanied muons as

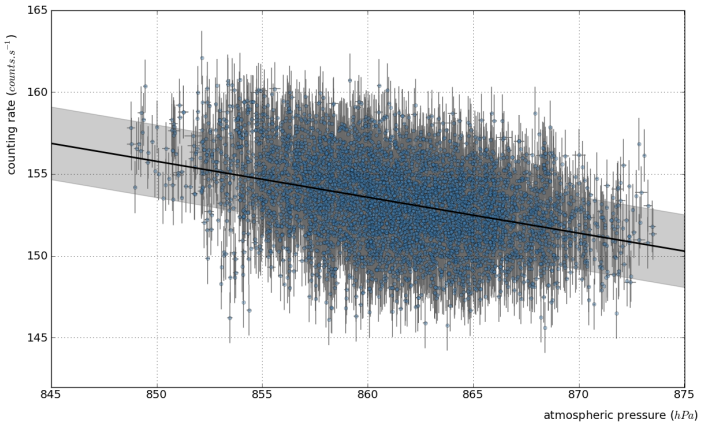

Figure 5.3.3: An example linear fit to the counting rate data and atmospheric pressure for the deposition energy bin surrounding 240 MeV. The data shown are for PMT 1 of station 101 and covers the whole period of 2006.

expected. However, the figure also clearly shows a change in pressure coefficient with deposited energy. This change in pressure coefficient may be indicative of a change in the energies of cosmic rays which contribute over the energy range of the charge histograms.

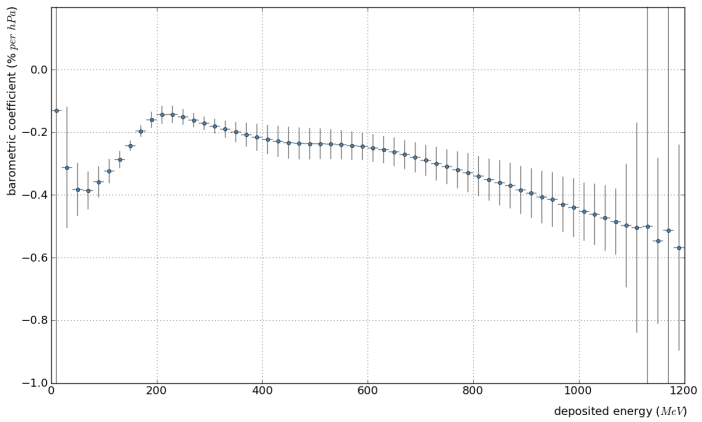

Figure 5.3.4: The average barometric coefficients calculated for each deposition energy bin over the sub-array of the surface detector for 2006. The change in the coefficient value with deposition energy may indicate a change in the energies of cosmic rays which contribute over the energy range of the charge histograms.

It is expected that the atmospheric pressure will affect shower development in a similar manner across the array since its linear dimensions of ~ 60 km are small compared to the dimensions of the synoptic scale meteorological processes. Consequently, the average pressure coefficients determined for each energy bin over the

sub-array are used to correct the data from each PMT of each station. The correction used is as follows:

$$r_c = r(1 - \bar{\alpha}\Delta P) \tag{5.3.1}$$

where r and r_c are the uncorrected and corrected counting rates (counts.s^{-1}) respectively, $\bar{\alpha}$ is the average fractional pressure coefficient (hPa^{-1}) averaged across all PMTs in the sub-array of stations surviving the quality cuts on operation and performance, and ΔP is the difference between the measured and mean pressure values (hPa).

Following the application of this pressure correction, a diagnostic test is performed in which the pressure coefficients are again calculated on the pressure corrected data. A successful pressure correction results in the test coefficients having values of approximately zero as can be seen in Figure 5.3.5. Figure 5.3.6 shows the matching plot to Figure 5.3.2 in which the pressure corrected counting rate and atmospheric pressure are plotted. The strong inverse correlation between the two data sets that was evident in Figure 5.3.2 is no longer present.

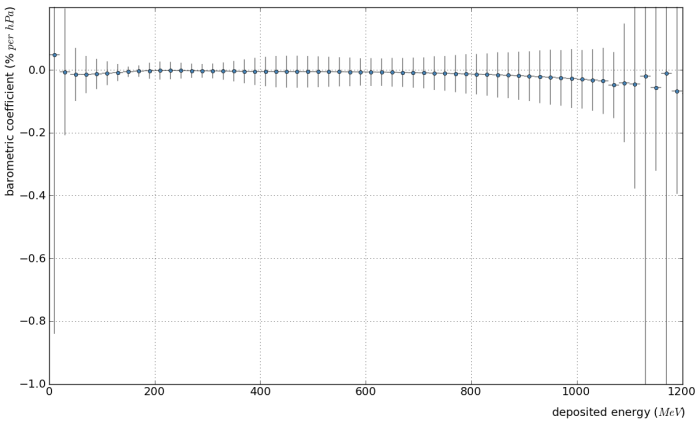

Figure 5.3.5: Average pressure coefficients calculated for each deposition energy bin over the sub-array of the surface detector for 2006 following the application of the pressure correction. As expected, the resulting coefficients are ≈ 0 in comparison with those shown in Figure 5.3.4 which were based on uncorrected data over the same time period.

5.3.3 Temperature Correction

Variations in the air temperature produced changes in the air density, and hence also affect the development of an EAS at high altitudes. The magnitude of this dependency is generally considered low in comparison with the magnitude of the barometric effect [112]. In the case of the Pierre Auger Observatory's SD stations, however, it was expected that there may also be a temperature dependence in the

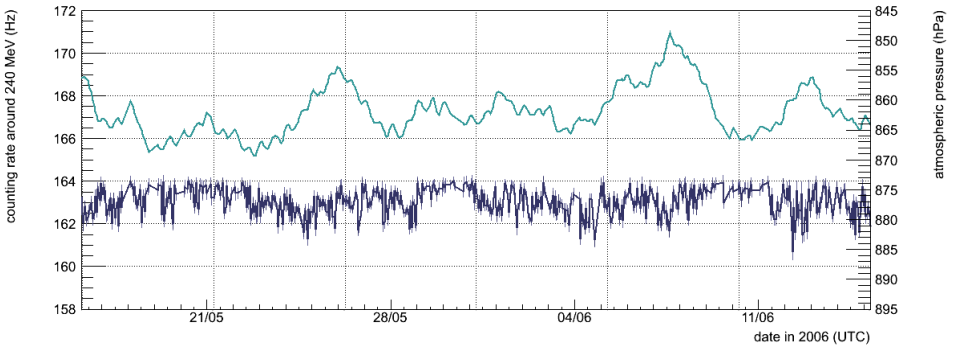

Figure 5.3.6: Timeseries of the now pressure corrected counting rate in the 20 MeV deposition energy bin surrounding 240 MeV *(dark blue)* and atmospheric pressure *(green)*. The correlation between counting rate and pressure that was clearly present in Figure 5.3.2 has been removed.

individual station electronics.

Correction for the fluctuations in air temperature was therefore performed in a similar manner to the barometric correction described above. Following the application of the barometric correction on the charge histogram data, the relationship between temperature and particle counting rate was, again, determined by a linear fit to the data. However, since the temperature coefficient was expected to vary slightly from station to station as a result of the temperature dependence of the individual station electronics, the temperature coefficients were calculated and applied individually for each PMT of each station in the sub-array. The correction used is then as follows:

$$r_{TPc} = r_{Pc}(1 - \beta\Delta T) \tag{5.3.2}$$

where r_{Pc} and r_{TPc} are the pressure corrected and temperature corrected counting rates (counts.s^{-1}) respectively, β is the fractional temperature coefficient (per ^{o}) calculated for each individual PMT in the sub-array of stations surviving the quality cuts on operation and performance, and ΔT is the difference between the measured and mean air temperature values (^{o}). An example of the temperature coefficients calculated for PMT 1 of station 101 during 2006 are shown in Figure 5.3.7. As with the barometric coefficients, a variation in the temperature coefficient value with deposited energy is evident which may indicate a change in the energies of cosmic rays which contribute over the energy range of the charge histograms.

5.4 Contributions to the Charge Histograms

As we have seen from the variation of both the barometric and temperature coefficients described above, it appears that particles contributing to the charge histogram

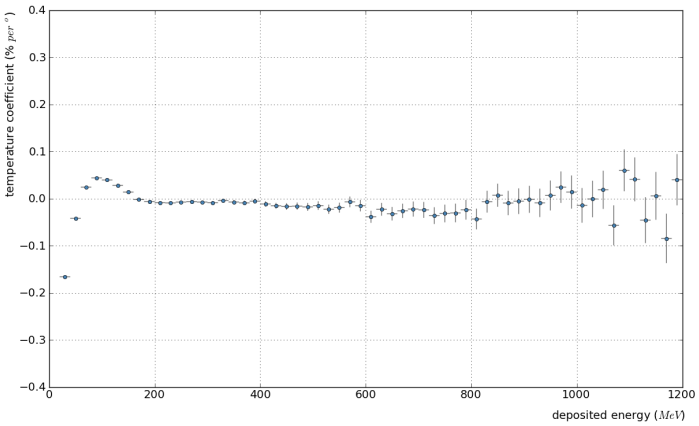

Figure 5.3.7: An example of the temperature coefficients for each deposition energy bin calculated for PMT 101 of Station 101 during 2006. The temperature coefficients are calculated following the application of the pressure correction and, as with the barometric coefficients (see Figure 5.3.4), show a variation with deposited energy.

may change over the deposition energy ranges spanned by the histograms.

The arrival rate of the background unaccompanied muons can be approximated to be 1 particle per cm^2 per minute so it follows that, in a single water-Cherenkov tank with a surface area of 10 m^2 and a water depth of 1.2 m, that this background muon flux becomes ∼3000 particles.s^{-1}. Given that a single FADC time bin spans 25 ns, the probability of a single unaccompanied muon arriving within a FADC time bin becomes $P(1) \approx 7.5 \times 10^{-5}$. The probabilities of a double or triple coincidence of unaccompanied muons occurring within a 25 ns FADC bin are then $P(2) \approx 5.6 \times 10^{-9}$ and $P(3) \approx 4.2 \times 10^{-13}$ respectively. In a charge histogram with an integration time of 61 s, these probabilities result in an expected number of entries corresponding to single unaccompanied muons of $E(1) \approx 183000$ per histogram. The expected number of entries corresponding to double and triple coincidences would then be $E(2) \approx 13.7$ and $E(3) \approx 0.001$ per histogram respectively.

Integrating over small regions around 240 MeV, 480 MeV and 720 MeV (1, 2 & 3 VEM) as shown in Figure 5.4.1 gives the following numbers of particles: $N(1\text{ VEM}) \approx 66000$, $N(2) \approx 9800$ and $N(3) \approx 1750$. These measured numbers around 2 and 3 VEM are significantly higher than those expected if the contributions were from double and triple coincidences of unaccompanied muons alone.

Further study of the possible contributions to the charge histograms requires simulation of the station response to cosmic ray air showers of various energies. A description and analysis of the simulations performed to investigate this are presented in Chapter 6 along with a discussion of the results obtained. These results then lead to the selection of the deposition energy range selections used in the anisotropy

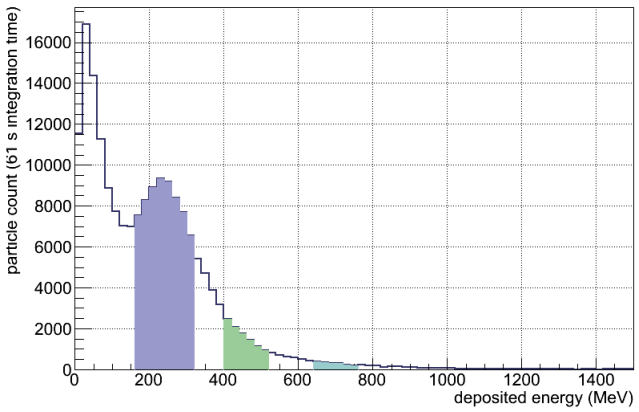

Figure 5.4.1: Small integration regions surrounding 240 MeV *(blue)*, 480 MeV *(green)* and 720 MeV *(light blue)* used to determine the approximate number of particles in these regions for an average 61 s charge histogram.

analysis described in Chapter 7.

6: Numerical Simulations

In order to establish the primary energy range of the cosmic ray showers contributing to the signals recorded in the charge histograms, it is necessary to simulate the SD tank response to the various secondary particle species. A simple simulation was therefore set up in which the propagation and development of an air shower was simulated using the AIRES (AIR-shower Extended Simulation) package. Data associated with all the particles reaching ground level were stored to a file and then fed into a second simulation. This second simulation used a series of modules in the Offline framework to model the tank response to the secondary particles produced in each simulated air shower. Each of these simulation processes are described within this chapter together with a discussion of the results obtained. At this stage, it should also be emphasised that these simulations were generated in order to allow an estimate of the component parts of the charge histograms and, as such, are not greatly detailed.

6.1 AIRES

The initial part of this simple simulation of the showers involved the simulation of the interactions of cosmic ray particles with the atmosphere. The AIRES system was chosen to simulate the propagation of cosmic ray air showers through the atmosphere, thus producing datasets of secondary particles that would be observed at the surface from showers initiated by different primary energies and species.

6.1.1 The AIRES system

The AIRES package is designed to simulate the cosmic ray air showers generated by primary particles with energy up to 10^{21} eV. The version used in this simulation experiment (2.8.4a) is an evolution of the original AIRES system which was strongly based on the MOCCA simulation package developed by Hillas [113]. It incorporates a modular design and contains features designed to allow for the very large number of secondary particles associated with high energy cosmic ray air showers. These features include sampling methods (such as the thinning algorithm developed by Hillas [114]) that aim to reduce the number of secondary particles that must be followed

in the shower. They also include the development of a computing environment that is suitable for the very long computational times involved in the simulation of high energy showers.

Table 6.1.1 lists the characteristics of the AIRES system; the primary particle species and energies as well as the environment variables which can be customised. A wide range of particles are taken into account in the simulations, with any propagated particles listed in Table 6.1.1 able to be set as the initiating primary particle. The primary particle may also be set to be a "special" primary defined by the user. The air shower interaction and decay processes that are simulated by AIRES are also listed in Table 6.1.1 and include the electrodynamic processes, unstable particle decays, hadronic interactions and charged particle propagation. The hadronic interaction package can be set to use either the SIBYLL [115, 116] or QGSJET [117, 118] model.

Shower simulations are steerable using the user input language *IDL* (input directive language) in which the initial settings for the shower are defined. That is, the primary cosmic ray particle species and energy, the arrival direction, the environment variables and the extent to which any thinning occurs. Many of these parameters may be input as a range. For example, showers may be generated over a range of zenith or azimuth angles.

6.1.2 Simulation Settings

The purpose of this simulation experiment was to investigate the characteristics of the cosmic ray air showers whose particles contribute to the signals in the charge histograms produced for each PMT of each SD station (described in Section 5.1). To this end, a series of low energy cosmic ray air showers were simulated with a range of primary particle species and energies.

Primary energies were generated following a power law spectrum with spectral index $\gamma = -1.71$. The primary particle species was determined by sampling from a list of composition flux ratios (as given in [121]). The flux ratios used are summarised in Appendix B. The cosmic ray air showers were simulated with arrival directions covering a uniform solid angle to 89^{o} from the zenith and the environment settings were chosen to match the conditions at the Pierre Auger Observatory site as much as possible. The "`el Nihuil`" site configuration was chosen as it simulates the altitude of the Pierre Auger Observatory. The atmosphere and geomagnetic field were also chosen to be as realistic as possible.

Since it was expected that those secondary particles contributing to the signals in the charge histograms would have very low energy, the thinning and energy cut levels were set to the minimum possible; these were a thinning value of 500 keV and energy cuts at 80 keV - 500 keV depending on the secondary particle species. Six primary energy ranges were simulated spanning half or full decades in energy.

propagated particles	Gamma-ray photons, leptons ($e^{\pm}$, $\mu^{\pm}$), baryons (π^0, $\pi^{\pm}$, η, $K^0_{L,S}$, $K^{\pm}$) and nuclei up to $Z = 36$. Neutrinos are generated and accounted for in energy but are not propagated.
primary particles	All propagated particles can be injected as primary particles. Multiple and/or "exotic" primaries can be injected using the *special primary* feature.
primary energy range	From 800 MeV to 1 ZeV (10^{21} eV).
geometry and the environment	Incidence angles from vertical to horizontal showers. The Earth's curvature is taken into account for all inclinations. Realistic atmosphere (Linsley model). Geomagnetic deflections: the geomagnetic field can be calculated using the IGRF model [119].
propagation (general)	Medium energy losses (ionisation). Scattering of all charged particles including corrections for finite nuclear size. Geomagnetic deflection.
propagation (electrons and gamma-ray photons)	Compton and photoelectric effects. Bremsstrahlung and e^+e^- pair production. Emission of knock-on electrons. Positron annihilations. Landau-Pomeranchuk-Migdal effect and dielectric suppression. Photonuclear reactions.
propagation (muons)	Bremsstrahlung and muonic pair production. Emission of knock-on electrons. Decay.
propagation (hadrons and nuclei)	Hadronic collisions using the EHSA [114] (low energy) and QGSJET [117] or SIBYLL [115] (high energy). Nucleus-nucleus collisions via QGSJET or SIBYLL or using a built-in nuclear fragmentation algorithm. Hadronic cross-sections are evaluated from fits to experimental data (low energy), or to QGSJET or SIBYLL predictions (high energy). Emission of knock-on electrons. Decay of unstable hadrons.
statistical sampling	Particles are sampled by means of the Hillas thinning algorithm [114], extended to allow control of maximum weights.
main observables	Longitudinal development of all particles recorded in up to 510 observing levels. Energy deposited in the atmosphere. Lateral, energy and time distributions at ground level. Detailed list of all particles reaching the ground and/or crossing predetermined observing levels.

Table 6.1.1: The main characteristics of the AIRES system. Taken directly from [120].

The simulations performed are listed in Table 6.1.2 which also shows the number of showers simulated for each simulated energy range. Figure 6.1.1 shows examples of the distributions of the primary cosmic ray particle settings for the simulated energy range 10^2 to $10^{2.5}$ GeV. The distributions of the primary particle species, energy and arrival direction are shown.

simulated energy range		*no. of simulated showers*
E_{min} (GeV)	E_{max} (GeV)	
10	10^2	100,000
10^2	$10^{2.5}$	100,000
$10^{2.5}$	10^3	100,000
10^3	$10^{3.5}$	100,000
$10^{3.5}$	10^4	100,000
10^4	10^5	10,000

Table 6.1.2: The number of simulated showers produced for each primary cosmic ray particle energy range.

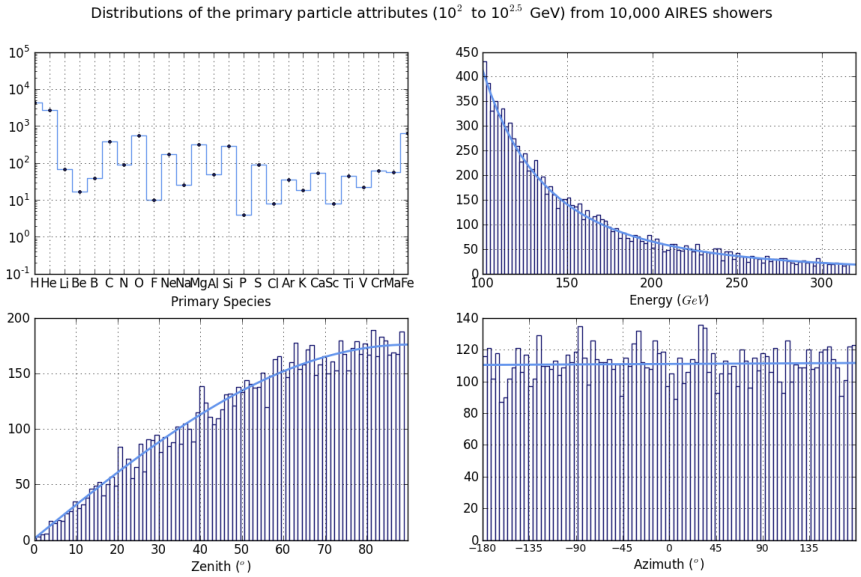

Figure 6.1.1: Diagnostic distributions of the primary cosmic ray particle attributes for the simulated energy range 10^2 to $10^{2.5}$ GeV (i.e. 100 GeV to 316 GeV) showing (clockwise from top left) the distributions of the primary particle species, primary particle energy, zenith angle, and azimuthal arrival direction angle.

The air shower simulations were performed using the AIRES runner system which allows multiple simulation tasks to be queued, run, paused and resumed as needed. The output of these simulations included summary files of the shower simulation as

well as compressed data files of the secondary shower particles that reached ground level. The data associated with the secondary particles reaching the ground were stored only for those particles landing within 2 km of the shower core.

6.1.3 Ground Particles

Following the simulation of the showers listed in Table 6.1.2, the data associated with those secondary particles that reached ground level and landed within 2 km from the shower core were stored. Initially those data were stored in the compressed output file produced by AIRES but were then checked and re-stored in a format that would be easier to read from in the tank simulation. The information stored in these files includes a record of the properties of the primary cosmic ray particle: its species, energy and arrival direction. In addition, the properties of each of the secondary particles were also recorded: their individual species, energy, position with respect to the shower core and their propagation direction.

Distributions of the energy and radial distance from the shower core for each of the secondary particle species are shown in Figures 6.1.3 and 6.1.4, while Figure 6.1.2 shows the distribution of the secondary species for a sample of 10,000 mixed composition AIRES showers with primary energies in the range 10^2 to $10^{2.5}$ GeV. From Figure 6.1.4, we can see that much of the secondary component falls a significant distance from the shower core. It is also evident that the electromagnetic component (γ-rays and e^+, e^-) far outnumbers the other species as expected.

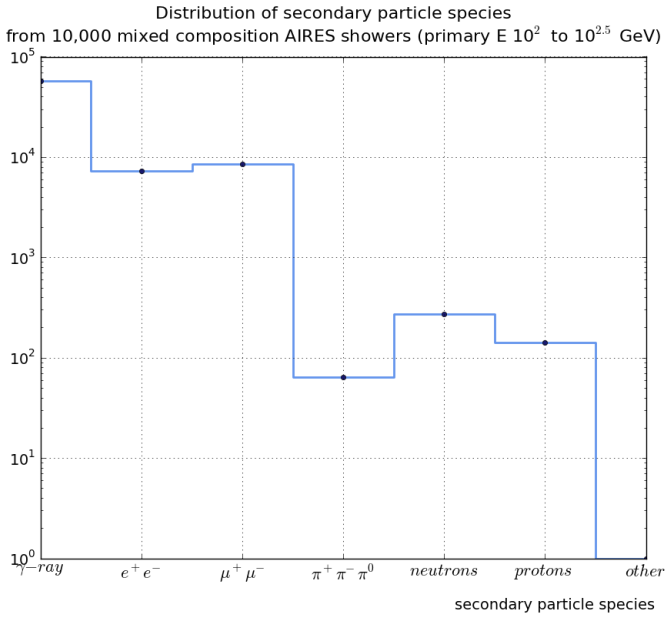

Figure 6.1.2: Distribution of the species of secondary particles reaching the ground, for a sample of 10,000 mixed composition AIRES showers with primary energies in the range 10^2 to $10^{2.5}$ GeV.

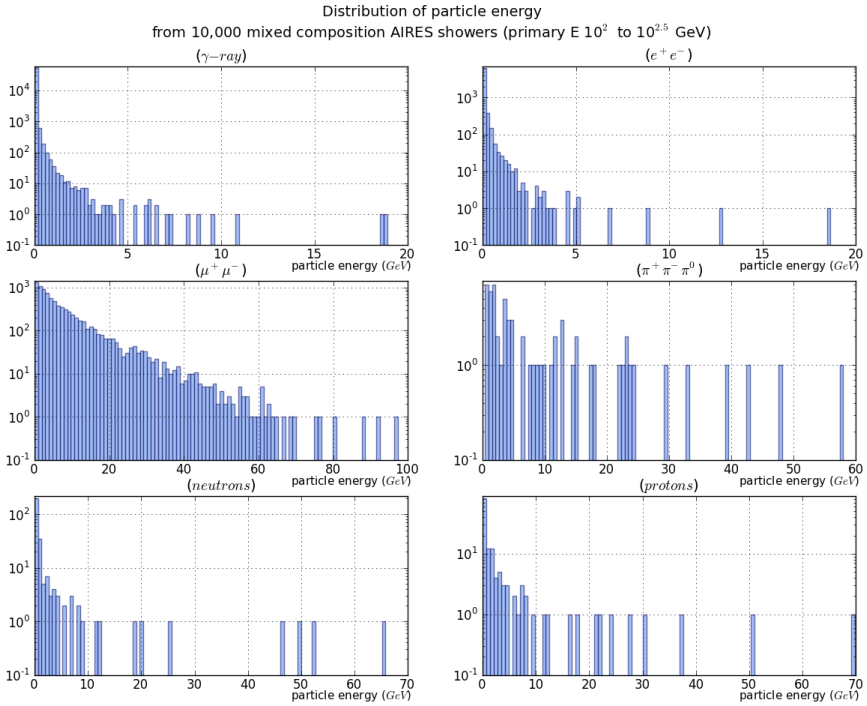

Figure 6.1.3: Distribution of the energy of each of the secondary particle species reaching the ground, for a sample of 10,000 mixed species AIRES showers with primary energies in the range 10^2 to $10^{2.5}$ GeV.

6.2 Tank Simulation

Following the simulation of the secondary particles that reach the surface using the AIRES package, the water-Cherenkov tank response to these particles was simulated using the $\overline{\text{Off}}\underline{\text{line}}$ framework. A detailed description of the $\overline{\text{Off}}\underline{\text{line}}$ framework can be found in Argirò et al [108].

.

6.2.1 $\overline{\text{Off}}\underline{\text{line}}$ Surface Detector Simulation

The tank response to secondary particles was simulated via a series of modules from the $\overline{\text{Off}}\underline{\text{line}}$ framework which simulated the geometry of the Auger water-Cherenkov tanks, the response of the 3 PMTs within each tank and the resulting output charge. These modules were implemented in the following sequence:

- ParticleInjectorNEU
- G4TankSimulatorOG
- SdPMTSimulatorOG

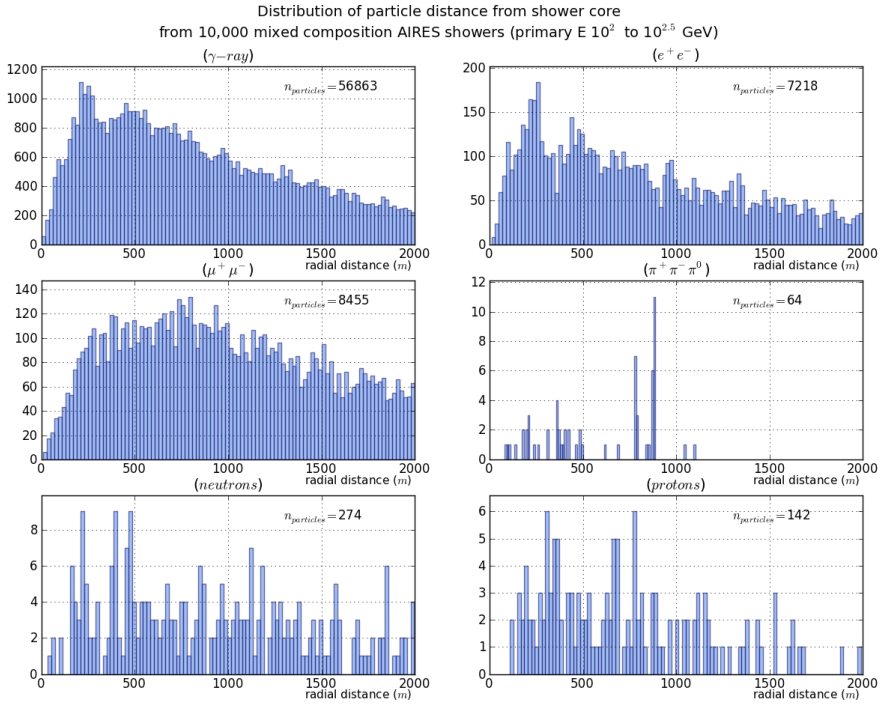

Figure 6.1.4: Distribution of the radial distance to the shower core of each of the secondary particle species reaching the ground, for a sample of 10,000 mixed species AIRES showers with primary energies in the range 10^2 to $10^{2.5}$ GeV.

- SdFilterFADCSimulatorMTU
- SdBaselineSimulatorOG, and
- SdSimulationCalibratorOG

The core of the simulated shower was randomly positioned within a 500 m x 500 m area with the simulated tank placed at the centre. Initially a short code was run to test whether any of these secondary particles fell within a short distance (arbitrarily 10 m) of the tank, and hence were more likely to pass through the tank producing a charge response. If this condition was met, the Offline modules were implemented and the particles injected into the tank with the total charge then output. Because the core was randomly positioned, it was possible to use the same shower set multiple times to generate a much vaster set of tank responses to the simulated showers. The effective number of showers is then the number of times a shower was placed within the 500 m x 500 m area surrounding the simulated tank (including any repeated showers). This effective total number of simulated showers at each primary energy range is given in Table 6.2.1.

6.2.2 Calibration

As described in Section 6.1.2, many cosmic ray shower simulations were produced at different primary energy ranges. Two main corrections were performed in order to obtain more realistic numbers of secondary particles and, hence, resulting charge values in the tank response. The number of simulations in each range first had to be scaled to match the expected number of showers falling within the 500 m x 500 m area surrounding the tank. These were then also scaled to account for those particles lost by restricting the core to falling within this area.

The initial scaling simply multiplied the total charge output by the fractional difference between the number of simulated showers in each energy range and the number of showers expected within a 250,000 m^2 area and is summarised in Table 6.2.1. This was calculated using the relationship:

$$\frac{dN}{dE} = A.E^{\alpha} \tag{6.2.1}$$

where $A = 50118.72$, and $\alpha = -2.7$.

The second calibration involved a correction for those lost secondary particles that would have passed through the simulated tank and thus contributed to the total measured charge but which originated from showers in which the core fell outside the 500 m x 500 m area surrounding the tank. From the distributions in Figure 6.1.4, we see that a large number secondary particles are likely to fall outside this area and so a correction was calculated by taking the ratio of the number of particles (excluding

primary energy range		*effective no. of*	*no. of showers expected*	*scaling factor*
E_{min} (GeV)	E_{max} (GeV)	*simulated showers*	*within 250,000 m^2 (see Eqn 6.2.1)*	
10	10^2	96,605,830	4.13×10^{10}	427.53
10^2	$10^{2.5}$	75,216,782	6.68×10^8	8.88
$10^{2.5}$	10^3	84,823,922	9.22×10^7	1.09
10^3	$10^{3.5}$	50,000,000	1.28×10^7	0.26
$10^{3.5}$	10^4	10,000,000	1.80×10^6	0.18
10^4	10^5	100,000	2.92×10^5	0.29

Table 6.2.1: The total effective number of simulated showers produced for each primary particle energy range (multiple uses of the smaller AIRES shower datasets), with the number of showers expected to fall within a 250,000 m^2 area and the resulting scaling factor.

γ-ray photons) that fell beyond 250 m from the core to the total number of particles that fell within this distance. The resulting scaling factors for these lost particles are summarised in Table 6.2.2.

simulated energy range		*lost particle*
E_{min} (GeV)	E_{max} (GeV)	*correction factor*
10	10^2	18.69
10^2	$10^{2.5}$	5.67
$10^{2.5}$	10^3	4.12
10^3	$10^{3.5}$	2.96
$10^{3.5}$	10^4	2.00
10^4	10^5	1.14

Table 6.2.2: The fractional correction at each energy range for those particles lost due to restricting the core to fall within the 500 m x 500 m area surrounding the simulated tank.

As a final stage, the histograms of the corrected output charge were calibrated to units of MeV to match the charge histograms from the real water-Cherenkov tanks.

6.3 Results

Following the calibration processes, the simulated histograms were then able to be directly compared with the real charge histograms obtained from each PMT of the Pierre Auger Observatory's SD array. Since the aim of this simulation process was to discern the primary energies contributing to these charge histograms, the contribution of each of the simulated primary energy ranges to the total charge histogram was investigated. Figure 6.3.1 shows the contribution of each simulated energy range to

the summed calibrated simulated charge histogram, also shown is the average charge histogram for Station 101 (1) for the 2006 period.

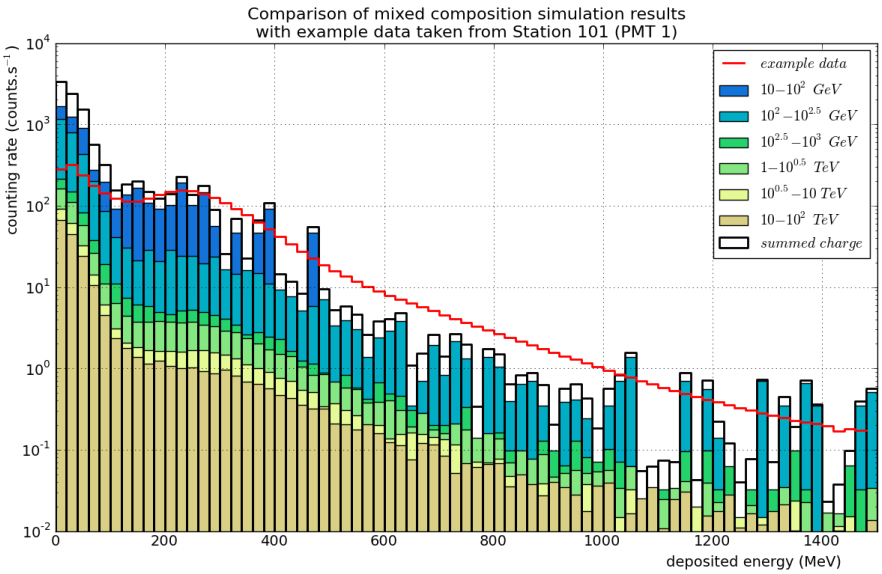

Figure 6.3.1: The calibrated charge histograms produced by secondary particles in each simulated energy range as well as the summed charge. The average charge histogram for Station 101 (1) from the 2006 period is also shown (red line) for comparison.

From Figure 6.3.1 it is clear that the simulation performed is relatively crude, and this must be taken into account with any conclusions drawn. It would be interesting to see the results of a similar simulation experiment performed in a more rigorous and sophisticated manner. However, within these limitations, the single particle peak associated with the passage of individual muons appears relatively well mapped for particles with primary energies in the range 10^1 GeV to 10^2 GeV. It is also clear that the signal beyond a deposition energy of around 500 MeV contains negligible contribution from those particles, but is instead dominated by particles with primary energies in the 10^2 GeV to $10^{2.5}$ GeV. Secondary particles produced by higher energy cosmic ray primaries do not appear to contribute significantly to the total charge. The fractional contribution of particles from each simulated energy range to the total simulated charge is shown in Figure 6.3.2 and clearly demonstrates this change in energy contribution.

From these results, it follows that the regions to be further investigated are:

- the region surrounding the single particle muon peak between 140 and 340 MeV,

- the region to the left (between 60 and 120 MeV) where the composition is less defined, and

- the region to the right of the single particle peak (between 480 and 940 MeV)

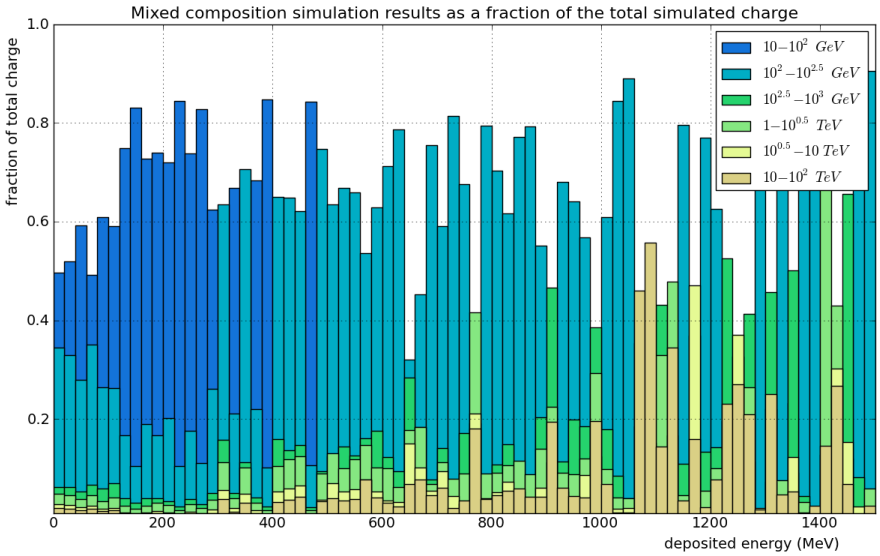

Figure 6.3.2: The fractional contribution of secondary particles from each simulated energy range to the total simulated charge.

where the lower energy contribution is negligible.

A study of the behaviour of the counting rates in these three independent regions will provide the basis of the main anisotropy investigation in this work.

7: Analysis, Results and Discussion

Following the cleaning and calibration process described in Chapter 5, and using the results from the simulations described in the Chapter 6, we are now in a position to investigate the intensity fluctuations at a range of independent energy ranges. The results of the numerical simulations indicate that the data contained in the charge histograms is dominated by two primary energy regions: below 100 GeV and 100-316 GeV. Since both these energies are very low, it is anticipated that there will be significant contribution to any observed anisotropy from solar effects. Indeed, these effects may dominate the results.

It was decided to analyse data from the charge histograms in 3 independent deposition energy regions: 60-120 MeV which lies to the left of the single particle muon peak, 140-340 MeV which spans the single particle peak, and 480-940 MeV which is a region well to the right. It is expected that the particles in the first two regions will display similar characteristics, containing predominantly muons originating from showers with primary energies below 100 GeV. The third region, however, is expected to contain particles originating from showers with the slightly higher energies of 100-316 GeV, and so may display different characteristics to the other regions. Figure 7.0.1 shows an example charge histogram calibrated into 75 bins, each spanning 20 MeV, highlighting the three regions to be investigated.

Figure 7.0.2 shows the timeseries of the data to be used in this analysis, averaged into 6-hourly intervals and displayed as a relative intensity to the yearly mean (%). Following the atmospheric correction and selection of a sub-array of only stations that were in operation for the full time period 2005 to 2009, it can be seen the data at each energy range still display significant modulations. The 2006 data at all three deposition energy levels shows a sharp decrease towards the end of the year. This is a Forbush decrease as described in Section 4.1.1 and is evidence that, although 2006-2009 was a period of very low solar activity, solar events did still occur. The 480-940 MeV deposition energy band also exhibits an increase in mean intensity during mid 2007 as well as a drop towards the end of 2009. However, the drop in rate in 2009 is also evident in the lower energy range (60-120 MeV) but not in the middle energy range (140-340 MeV). The origin of these changes in rate remains unclear at this stage.

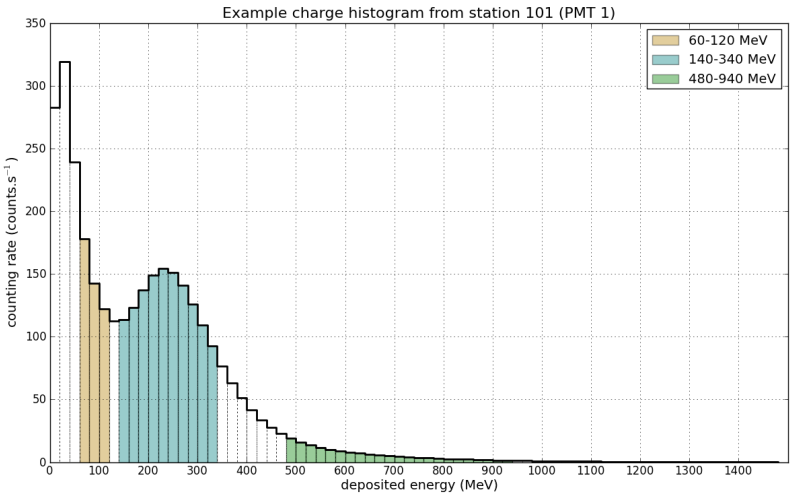

Figure 7.0.1: An example charge histogram calibrated into 75 bins, each spanning 20 MeV, highlighting the three deposition energy regions to be investigated. 1) 60-120 MeV, 2) 140-340 MeV and 3) 480-940 MeV.

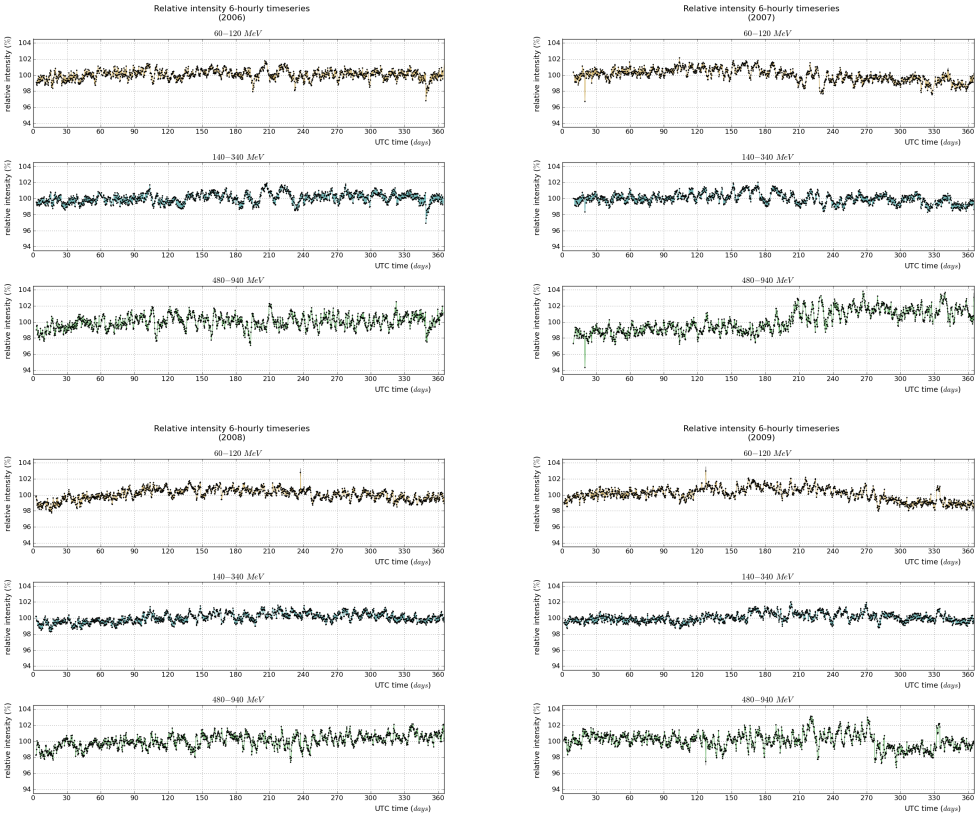

Figure 7.0.2: Timeseries of the data averaged into 6-hourly bins at each of the three energy ranges to be investigated. The data shown are plotted as relative intensities to the yearly mean value, and are calculated following the sub-array selection and atmospheric correction process described in Chapter 5.

We wish to investigate any anisotropies present in both the solar and sidereal frequencies and so, after subdividing the data into the three independent deposition energy regions, averages of the relative intensities were calculated in the different timeframes. Conversion formulae for each of the timeframes is provided in Appendix A. Figure 7.0.3 shows the solar activity cycle up till 2010 [122] in which it can be seen that the years 2006-2009 span a period of very low solar activity, whereas 2005 contains a higher level of solar activity. During periods of low solar activity, the cosmic ray flux is enriched by the very low energy particles which would otherwise be swept out from the solar system by the solar wind. Consequently, the period 2006-2009 is to be investigated first, studying the intensity fluctuations in both solar and sidereal frequencies, with comparative results from the more active 2005 period then also investigated. Solar events during the 2005 period are also studied and compared with measurements taken from various neutron monitors which are sensitive to solar activity.

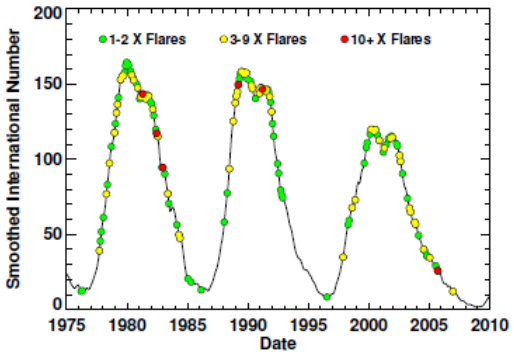

Figure 7.0.3: The International Sunspot Number for the period spanning 1975 to 2010 overlayed with the incidence of X-class flares. It can be seen that these flares can occur at any phase during the solar cycle [122].

7.1 Solar Anisotropy

The first frequency to be investigated is that of the solar time frame. Averages of the relative intensities were determined over 5 minute intervals, and folded over 24 hours in solar time. Figure 7.1.1 shows this average daily intensity fluctuation for each of years 2006-2009 while Figure 7.1.2 then shows the same, averaged over the whole four year time period. The curves plotted show the fits of the data to a first and second-order harmonic function of the form:

$$\sum_{i=1}^{2} A_i \cos\left(\frac{\pi}{12} i\,(t-\phi_i)\right) + B \tag{7.1.1}$$

where (A_i, ϕ_i) are the amplitude and phase of the ith harmonic, while t is the local time in hours and B is a constant. The shaded region represents the standard deviation of the difference between the fit and the data.

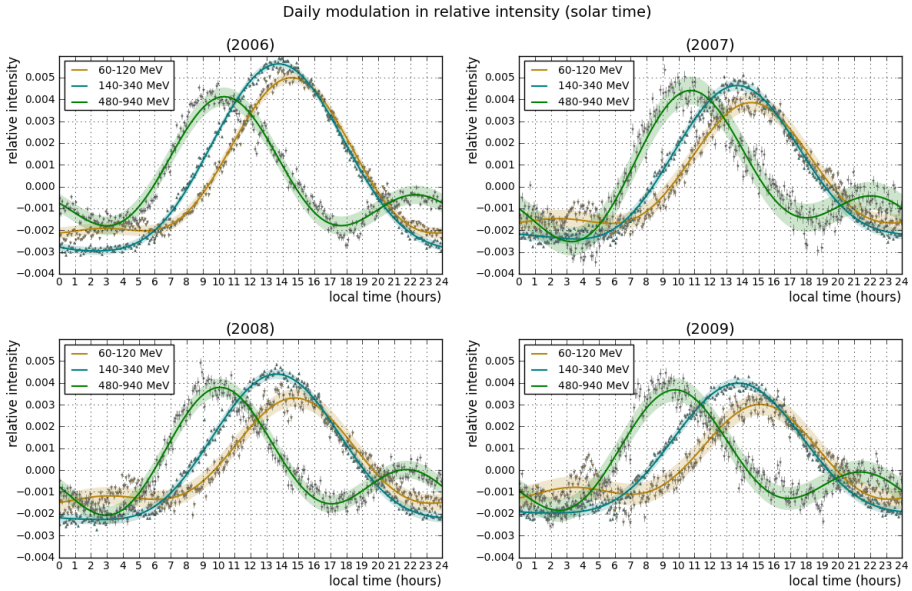

Figure 7.1.1: The average diurnal relative intensity modulation in local solar time at each deposition energy range in each of the years 2006 to 2009 with the data fitted to a first and second-order harmonic function. The shaded area represents the standard deviation of the fit. It can be seen that the characteristics of this modulation are consistent at each energy region across all four years.

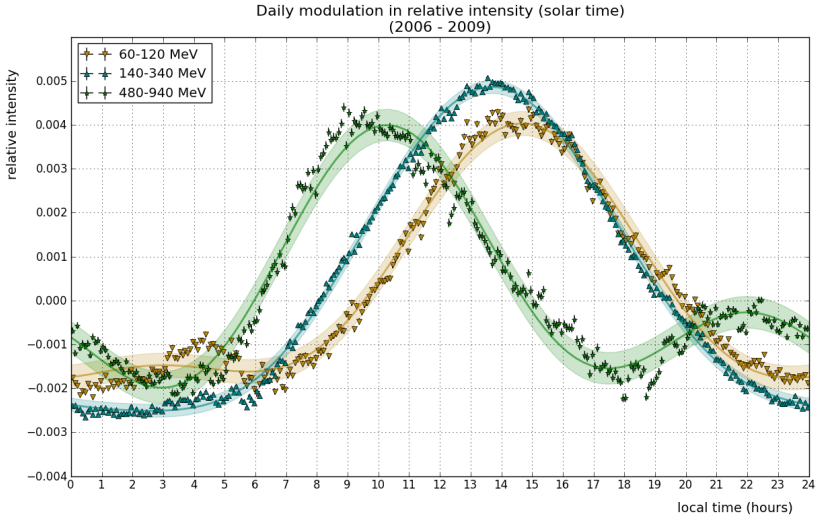

Figure 7.1.2: The average diurnal relative intensity modulation in local solar time averaged over the full 4 year period 2006-2009.

We can see from both these Figures that the data from regions 1 and 2 have maxima around 14 hours in local solar time. However, the third region has its maximum at around 10 hours with minima at around 3 and 18 hours. Table 7.1.1 lists the amplitudes and phases of the fitted 1st and 2nd harmonic, while Figure 7.1.3 shows the fitted first harmonic plotted as a phase diagram for each of the years 2006-2009 as well as over the full period.

Discussion of Solar Anisotropy

The solar modulation displays a remarkable degree of consistency between each of the years, and is particularly apparent in the phase diagrams. Particles influenced by heliospheric effects would be expected to display a phase of around 14 hours [67], while a signal in the solar frequency produced galactic cosmic rays influenced by the Compton-Getting effect of the Earth's orbit around the Sun would be expected to have a phase of ∼6 hours in local solar time. At the lower two energy ranges we see that the maximum solar modulation occurs at a phase of around 14 hours, as expected for heliospheric effects. However, at the higher energy region spanning deposition energies of 480-940 MeV, we see the phase begin to shift down to around 10 hours. It may be that, at these slightly higher energies, we begin to see a sufficient number of galactic cosmic rays to produce a total phase that results from a combination of both the heliospheric and the Compton-Getting effects.

At the lower energy ranges we may also be seeing evidence of the co-rotation anisotropy as described in Section 4.1.2, an effect associated with the motion of the solar magnetic field with respect to the Earth. This anisotropy is expected to have an amplitude of $\sim 0.6\%$ with a phase of ~ 18 hours in local solar time, and is expected to reduce to zero above primary energies of 10^{11} eV. We therefore expect this effect to be significantly reduced in the 480-940 MeV range. However, it may contribute to the phase difference between the lower two deposition energy ranges (60-120 MeV and 140-340 MeV) and the higher range (480-940 MeV).

7.2 Sidereal Anisotropy

As we have observed in the previous section, the data contain a significant modulation in solar time. We therefore anticipate that there will be considerable contamination of the sidereal time component from this solar modulation. Figure 7.2.1 shows the apparent daily relative intensity modulation in sidereal time at each of the three deposition energy ranges for each of the years 2006 to 2009 while Figure 7.2.2 shows the average over the full four year span. It can be seen that there is significant variation in the phase of the sidereal modulation between each year. This is especially evident in the 480-940 MeV deposition energy range. As before, the curved line shows

year	deposition E range (MeV)	1st harmonic (solar)		2nd harmonic (solar)		χ^2/ndf	# events
		amplitude ($\times 10^{-1}\%$)	phase ($hours$)	amplitude ($\times 10^{-1}\%$)	phase ($hours$)		
2006	60-120	3.46 ± 0.02	14.51 ± 0.02	1.17 ± 0.02	2.60 ± 0.03	2030.65 / 282	6455335
	140-340	4.28 ± 0.02	13.81 ± 0.01	0.85 ± 0.02	1.65 ± 0.03	3616.52 / 282	6455335
	480-940	2.25 ± 0.04	10.33 ± 0.06	1.64 ± 0.04	10.33 ± 0.04	2644.14 / 282	6455335
2007	60-120	2.66 ± 0.03	14.56 ± 0.05	0.99 ± 0.03	2.54 ± 0.07	2038.38 / 282	2956811
	140-340	3.47 ± 0.02	13.81 ± 0.02	0.89 ± 0.02	1.52 ± 0.04	2907.54 / 282	2956811
	480-940	2.50 ± 0.05	11.42 ± 0.08	1.76 ± 0.05	10.52 ± 0.06	2190.04 / 282	2956811
2008	60-120	2.25 ± 0.03	14.65 ± 0.06	0.89 ± 0.03	2.84 ± 0.07	2179.76 / 282	3046778
	140-340	3.33 ± 0.02	13.67 ± 0.02	0.79 ± 0.02	1.57 ± 0.05	2667.38 / 282	3046778
	480-940	1.91 ± 0.03	10.52 ± 0.07	1.73 ± 0.03	9.97 ± 0.04	1121.54 / 282	3046778
2009	60-120	1.91 ± 0.04	14.94 ± 0.08	0.92 ± 0.04	3.20 ± 0.09	2714.91 / 282	3044581
	140-340	2.98 ± 0.02	13.75 ± 0.02	0.66 ± 0.02	1.71 ± 0.06	2828.86 / 282	3044581
	480-940	1.91 ± 0.04	10.22 ± 0.09	1.54 ± 0.04	9.64 ± 0.06	1794.48 / 282	3044581
2006-2009	60-120	2.76 ± 0.02	14.60 ± 0.03	1.02 ± 0.02	2.73 ± 0.04	5157.01/ 282	15503505
	140-340	3.68 ± 0.01	13.77 ± 0.01	0.80 ± 0.01	1.61 ± 0.03	5686.72/ 282	15503505
	480-940	2.15 ± 0.03	10.59 ± 0.05	1.64 ± 0.03	10.17 ± 0.04	4155.44/ 282	15503505

Table 7.1.1: Amplitude and phase of the fitted first and second harmonics to the solar data for 2006 to 2009 at each deposition energy range with the χ^2/ndf of the fit to the data.

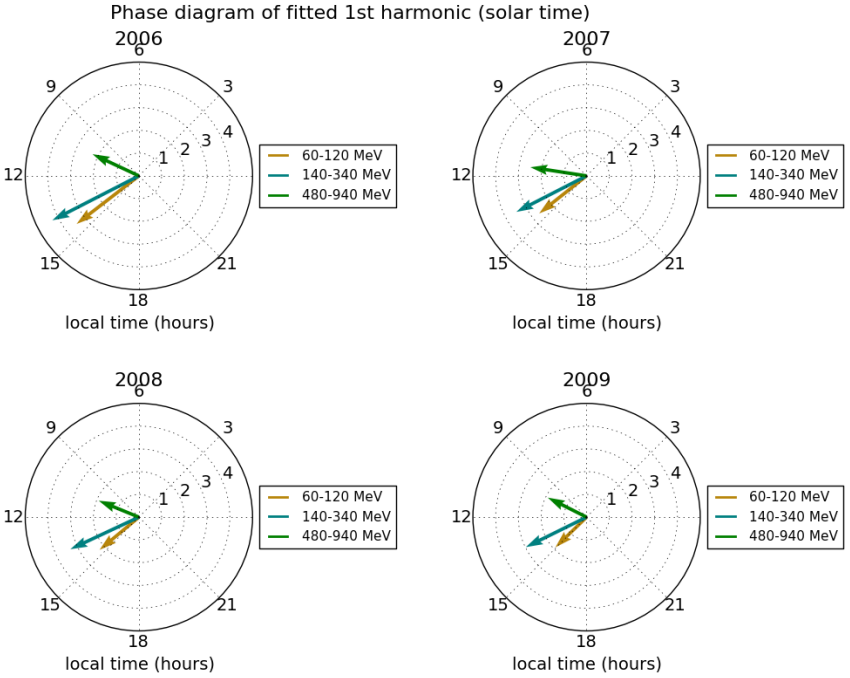

a)

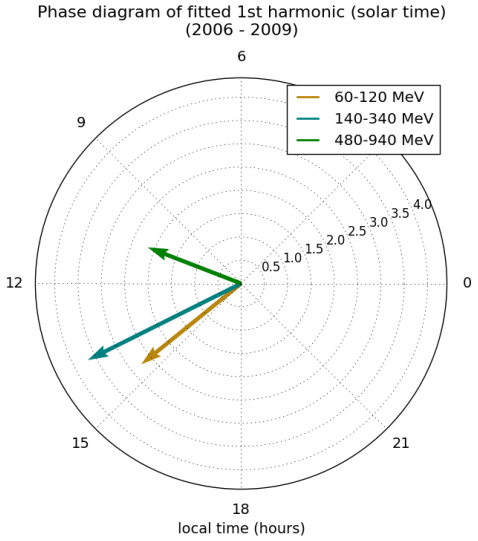

b)

Figure 7.1.3: Phase diagrams of the fitted first harmonic to the solar modulation of the relative intensity for a) each of the years 2006-2009 and b) the total 4 year period. The amplitudes are multiplied by 10^3. Note the consistency that can be seen each of the years.

the fit to a first and second-order harmonic function of the form described in Equation 7.1.1 with the shaded area representing the standard deviation of the fit. Table 7.2.1 lists the fitted amplitude and phase for each deposition energy range for each year, while Figure 7.2.3 shows the fitted first harmonic plotted as a phase diagram for each of the years 2006-2009 as well as over the full period.

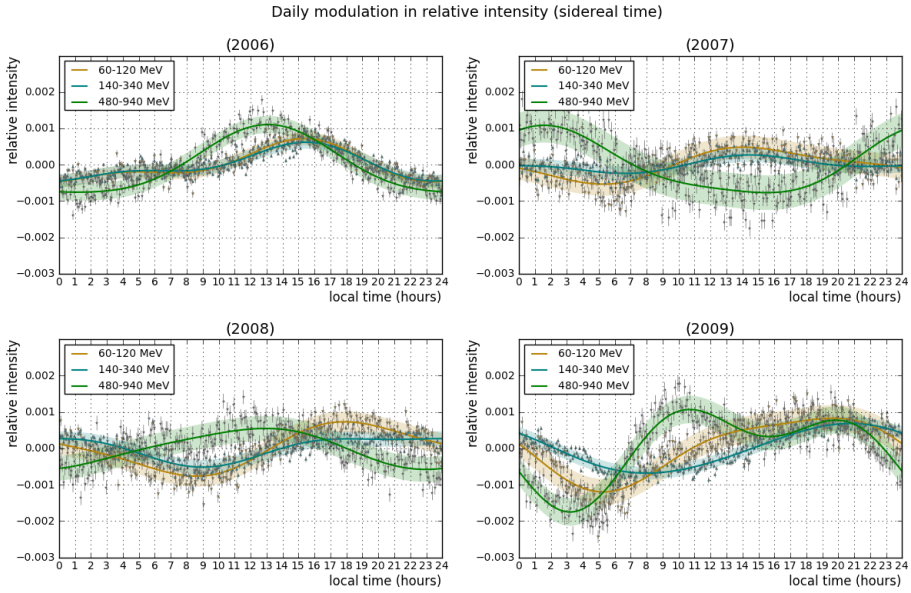

Figure 7.2.1: The average diurnal relative intensity modulation in local sidereal time at each deposition energy range in each of the years 2006 to 2009.

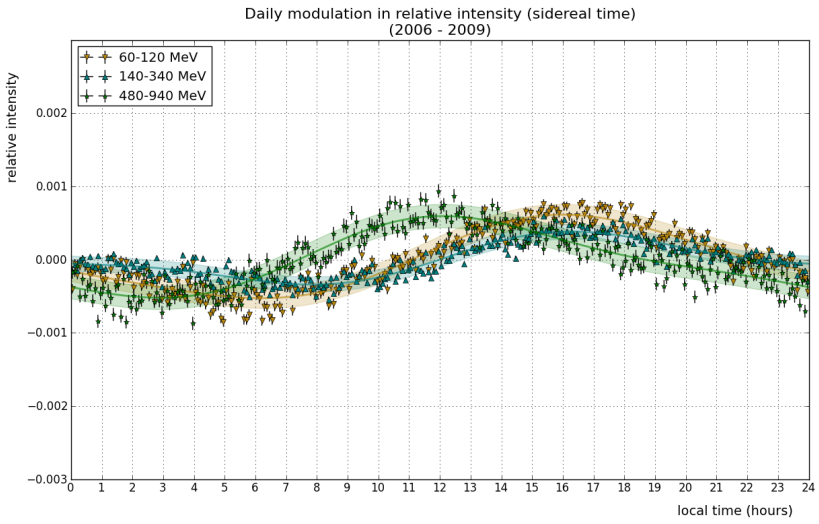

Figure 7.2.2: The average diurnal relative intensity modulation in local sidereal time averaged over the full 4 year period 2006-2009.

Section 4.3.2 describes a correction for the spurious signal which is generated in

year	deposition E range (MeV)	1st harmonic (sidereal)		2nd harmonic (sidereal)		χ^2/ndf	# events
		amplitude ($\times 10^{-2}\%$)	phase ($hours$)	amplitude ($\times 10^{-2}\%$)	phase ($hours$)		
2006	60-120	4.86 ±0.15	14.51 ± 0.02	2.38±0.15	3.75±0.12	1005.14 / 282	6455335
	140-340	4.31 ±0.15	13.81 ± 0.01	2.07±0.15	3.98±0.13	2992.87 / 282	6455335
	480-940	9.30 ±0.20	10.33±0.06	1.64±0.20	1.07±0.23	926.71 / 282	6455335
2007	60-120	4.45 ±0.27	14.56 ±0.05	1.40±0.27	0.40±0.36	1261.50 / 282	2956811
	140-340	1.86 ±0.16	13.81 ±0.02	1.10±0.16	1.78±0.28	1660.16 / 282	2956811
	480-940	9.03 ±0.40	11.42±0.08	1.92±0.40	1.12±0.40	1235.96 / 282	2956811
2008	60-120	6.86 ±0.24	14.65 ±0.06	1.61±0.24	4.16±0.29	1105.57 / 282	3046778
	140-340	3.81 ±0.17	13.67±0.02	1.30±0.16	2.97±0.24	2008.46 / 282	3046778
	480-940	5.43 ±0.29	10.52±0.07	0.82±0.29	3.47±1.67	868.78 / 282	3046778
2009	60-120	9.69 ±0.30	14.94±0.08	2.38±0.30	10.79±0.24	1421.89 / 282	3044581
	140-340	6.79 ±0.15	13.75±0.02	0.39±0.14	10.59±1.70	1606.50 / 282	3044581
	480-940	10.52 ±0.32	10.22±0.09	7.22±0.32	9.36±0.08	980.64 / 282	3044581
2006-2009	60-120	5.43±0.12	14.60±0.03	0.99±0.12	2.82±0.23	1311.72 / 282	15503505
	140-340	3.03±0.09	13.77±0.01	1.17±0.09	2.62±0.14	2616.90 / 282	15503505
	480-940	5.10±0.13	10.59±0.05	1.27±0.13	1.64±0.20	919.10 / 282	15503505

Table 7.2.1: Amplitude and phase of the fitted first and second harmonics to the sidereal data for 2006 to 2009 at each deposition energy range with the χ^2/ndf of the fit to the data.

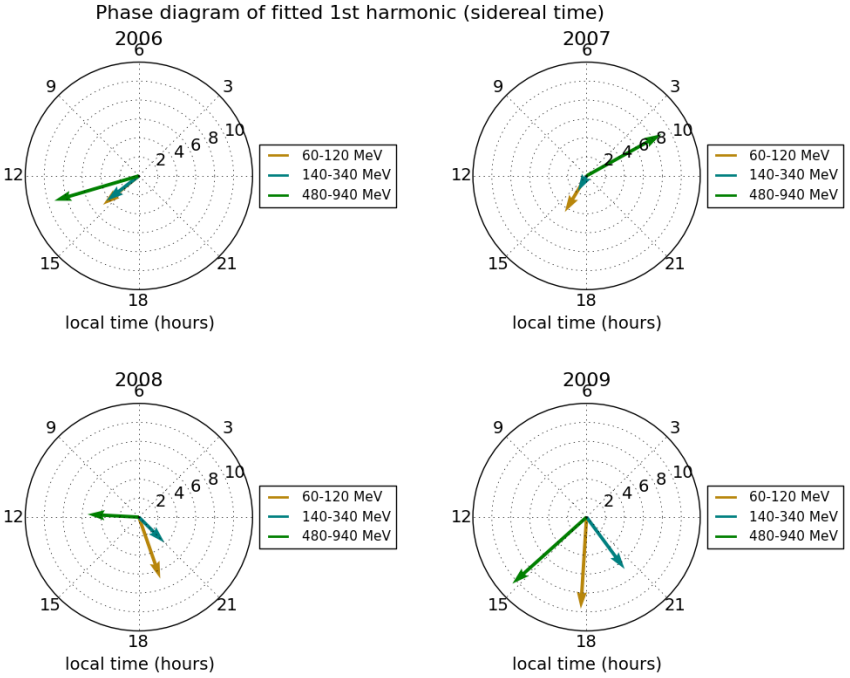

a)

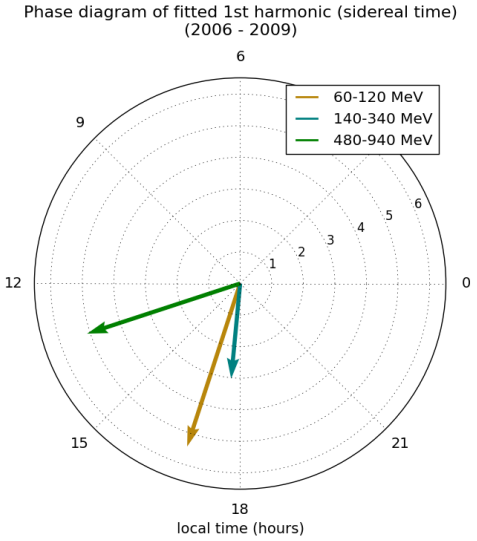

b)

Figure 7.2.3: Phase diagrams of the fitted first harmonic to the apparent sidereal modulation of the relative intensity for a) each of the years 2006-2009 and b) the total 4 year period. The amplitudes are multiplied by 10^4. Note the significant year to year variation.

the sidereal component from a modulation in the solar component. For an amplitude modulation in the solar frequency, spurious components will be produced in both sidereal and antisidereal time, where the antisidereal modulation will be a reflection of the sidereal modulation about the solar time axis. Farley and Storey [103] show that the apparent sidereal signal can be considered to be the sum of the "true" sidereal modulation and the spurious component produced by the solar amplitude modulation as follows:

$$\begin{aligned} A_{appsid}\cos 2\pi\left[(N+1)\,t+\phi_{appsid}\right] &= A_{asid}\cos 2\pi\left[(N+1)\,t+\phi_{refasid}\right] \\ &\quad +A_{truesid}\cos 2\pi\left[(N+1)\,t+\phi_{truesid}\right] \end{aligned} \tag{7.2.1}$$

where A_{appsid}, A_{asid} and $A_{truesid}$ are the apparent sidereal, antisidereal and "true" sidereal amplitudes respectively. Likewise, ϕ_{appsid}, $\phi_{refasid}$ and $\phi_{truesid}$ are the apparent sidereal, reflected antisidereal and "true" sidereal phases respectively. It follows that the "true" sidereal modulation can then be obtained by subtracting the antisidereal signal, reflected about the solar vector, from the apparent sidereal signal. The reflected antisidereal signal has a phase calculated by:

$$\phi_{refasid} = (\phi_{solar} - \phi_{asid}) + \phi_{solar} \tag{7.2.2}$$

where ϕ_{solar} is the phase of the 1st harmonic of the solar signal. Figure 7.2.4 shows the average daily modulation of the apparent sidereal and antisidereal signal at each deposition energy range for each of the years 2006-2009 while Figure 7.2.5 spans the full four year period. Table 7.2.2 lists the fitted amplitude and phase for the antisidereal signal at each deposition energy range for each year, while Figure 7.2.6 shows the fitted first harmonic plotted to the antisidereal modulation as a phase diagram for each of the years 2006-2009 as well as over the full period. In comparison to the phase diagrams of the apparent sidereal modulation, the antisidereal modulation shows a greater agreement between each of the years. Given the consistency between each year evident in the solar modulation, this is as expected.

We can see that the amplitudes of both the antisidereal and apparent sidereal modulations are similar and this indicates that the spurious signal dominates sidereal modulation. While a correction may be attempted, due to the combination of errors and the systematic uncertainty induced by a spurious signal of such magnitude, it may be that the resulting sidereal signal is of little significance.

Using the solar phases derived in the previous Section and listed in Table 7.1.1, the reflected antisidereal amplitude and phase were determined by reflecting the fitted curve about the solar phase. Figure 7.2.7 shows this procedure for the full

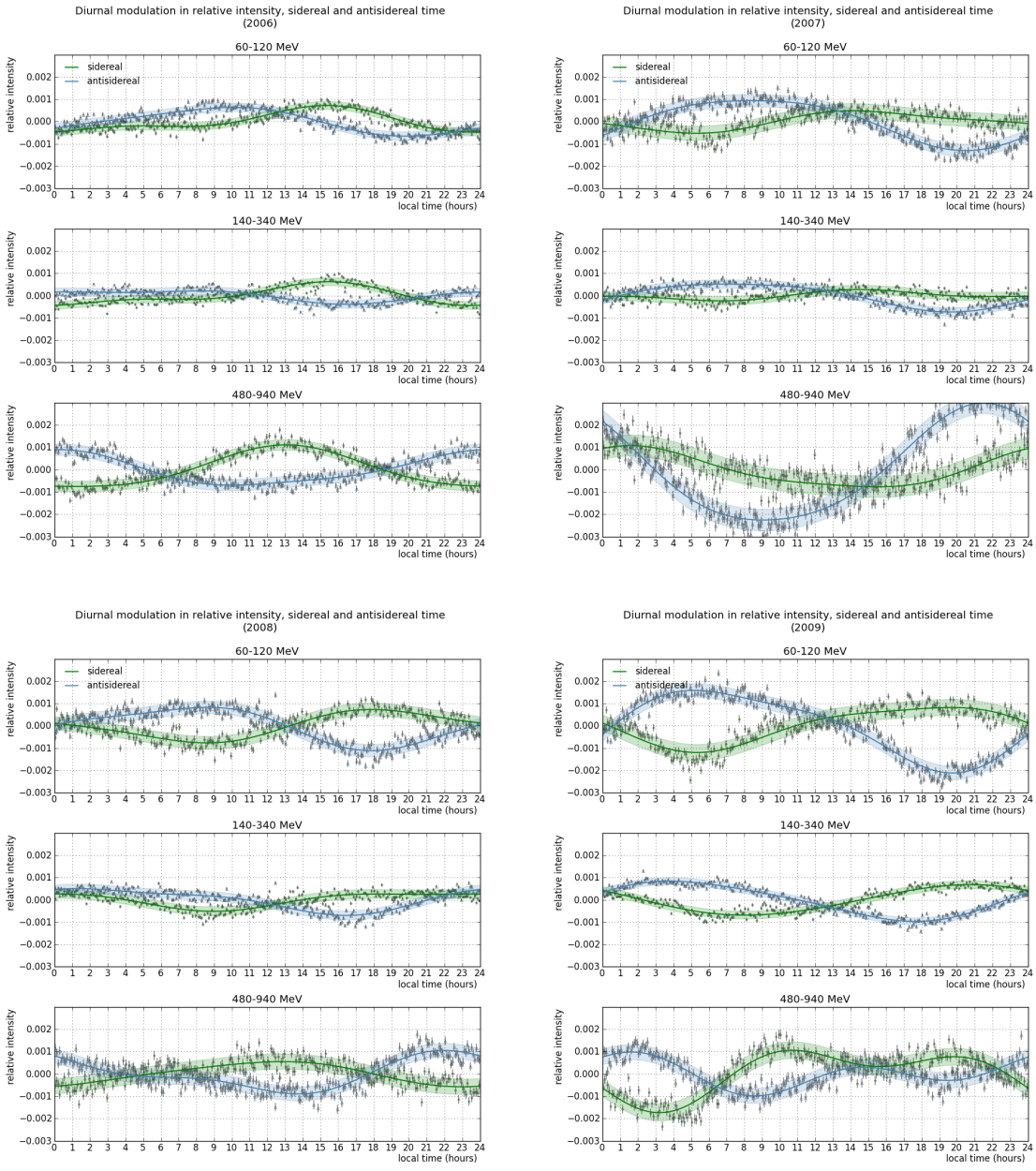

Figure 7.2.4: Comparison of the average daily modulation in sidereal time (green) with that of the antisidereal component (blue) at each deposition energy range for each of the years 2006-2009.

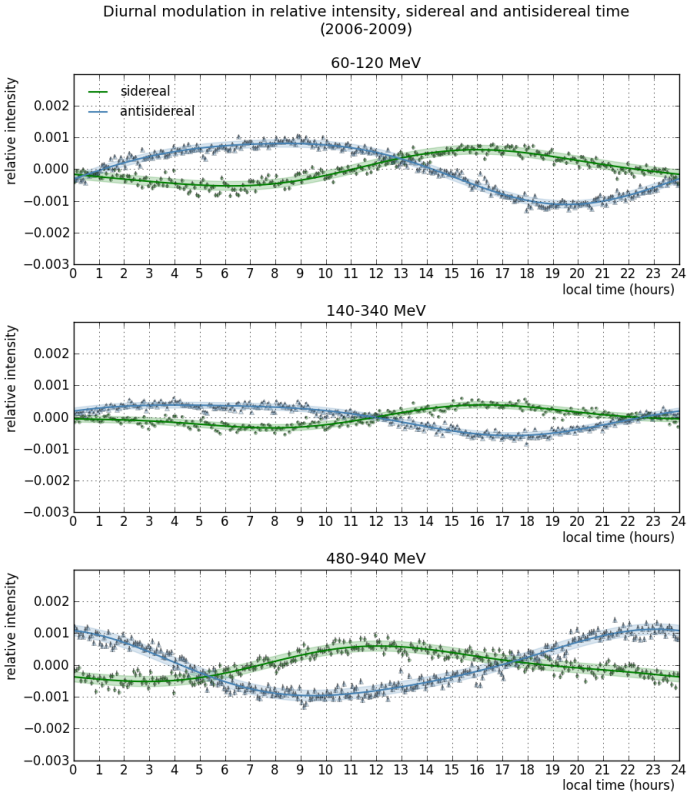

Figure 7.2.5: Comparison of the average daily modulation in sidereal time with that of the antisidereal component at each deposition energy range over the full four year period.

year	deposition E range (MeV)	1st harmonic (antisidereal)		2nd harmonic (antisidereal)		χ^2/ndf	# events
		amplitude ($\times 10^{-2}\%$)	phase ($hours$)	amplitude ($\times 10^{-2}\%$)	phase ($hours$)		
2006	60-120	6.09±0.16	8.87±0.10	1.15±0.16	0.12±0.26	1118.93 / 282	6455335
	140-340	2.68±0.15	4.75±0.21	1.20±0.15	10.38±0.24	3104.38 / 282	6455335
	480-940	7.55±0.22	23.74±0.11	1.70±0.22	1.00±0.24	1098.13 / 282	6455335
2007	60-120	11.18±0.23	8.45±0.08	1.81±0.23	2.49±0.25	994.41 / 282	2956811
	140-340	6.21±0.16	7.51±0.10	1.07±0.16	1.86±0.28	1652.35 / 282	2956811
	480-940	26.19±0.41	21.39±0.06	3.52±0.41	9.69±0.22	1290.86 / 282	2956811
2008	60-120	9.00±0.24	6.64±0.10	2.35±0.24	11.11±0.19	1057.69 / 282	3046778
	140-340	5.40±0.17	3.62±0.12	1.72±0.16	11.10±0.18	1992.42 / 282	3046778
	480-940	7.88±0.26	23.38±0.13	3.46±0.27	9.14±0.15	743.3 / 282	3046778
2009	60-120	17.39±0.26	7.01±0.06	4.13±0.26	2.54±0.12	1039.88 / 282	3044581
	140-340	8.72±0.14	4.89±0.06	1.25±0.13	1.17±0.20	1367.37 / 282	3044581
	480-940	4.90±0.29	23.06±0.22	6.14±0.29	2.10±0.09	804.51 / 282	3044581
2006-2009	60-120	9.57±0.10	7.73±0.04	1.49±0.10	1.26±0.13	934.8 / 282	15503505
	140-340	4.76±0.08	5.18±0.06	0.99±0.08	11.58±0.15	2259.86 / 282	15503505
	480-940	10.22±0.14	22.52±0.05	1.41±0.14	0.22±0.19	1022.21 / 282	15503505

Table 7.2.2: Amplitude and phase of the fitted first and second harmonics to the antisidereal data for 2006 to 2009 at each deposition energy range with the χ^2/ndf of the fit to the data.

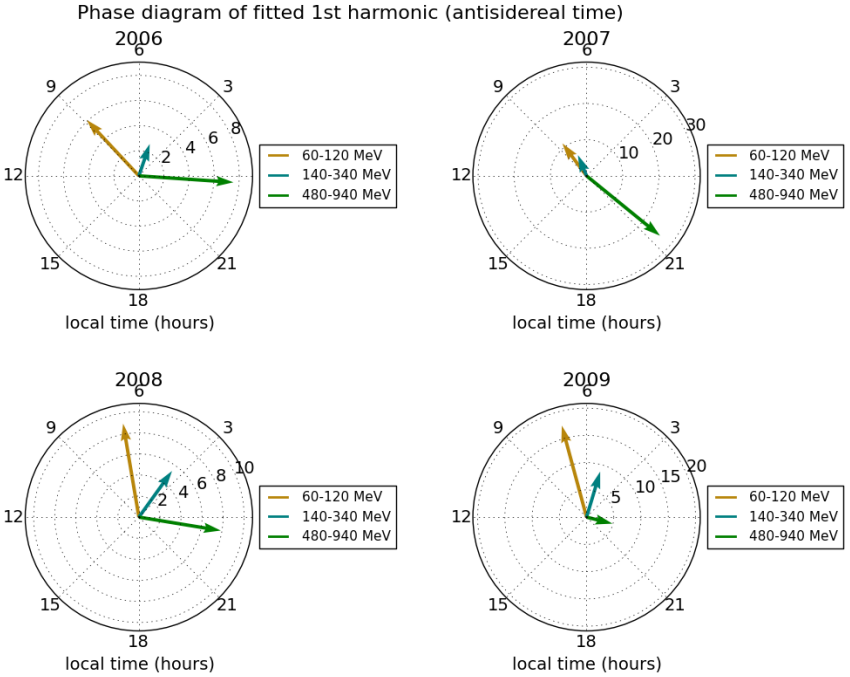

a)

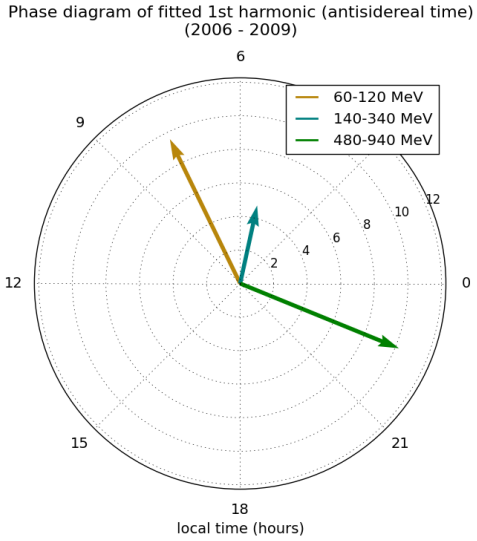

b)

Figure 7.2.6: Phase diagrams of the fitted first harmonic to the antisidereal modulation of the relative intensity for a) each of the years 2006-2009 and b) the total 4 year period. The amplitudes are multiplied by 10^4 and are shown on different scales. Note the general phase consistency between the yearly figures.

period 2006-2009, displaying the sidereal and antisidereal signals overlayed with the antisidereal signal reflected about the solar phase (vertical red line) as well as the final derived "true" sidereal modulation (thick black line), while Figure 7.2.8 shows this process performed at each of the four years individually. It can be seen that, like the apparent sidereal signals, the resulting "true" signals at each energy range differ significantly from year to year. Table 7.2.3 includes the amplitude and phase of the 1st and 2nd harmonic of the derived "true" sidereal signal for each of the years 2006 to 2009, while Figure 7.2.9 shows the fitted first harmonic plotted as a phase diagram for each of the years 2006-2009 as well as over the full period. When compared to the phase diagrams of the apparent sidereal modulation (Figure 7.2.3), the phase diagrams of the "true" sidereal modulation show a greater degree of consistency between each year. However, it must be noted that the phase diagrams do not contain information about either the second harmonic amplitude and phase, or the uncertainty in the first harmonic amplitude and phase.

Since this method of correction for a spurious solar signal in the sidereal modulation assumes only an amplitude modulation in the solar signal, it is also necessary to test for the presence of other spurious frequency modulations. If we assume that the only real modulations occur in the solar and sidereal time, then the presence of frequency components in the ultra-sidereal and ultra-antisidereal time (artificial time scales corresponding to +2 and -2 revolutions in a tropical year) may indicate that the solar time component is also modulated in phase. Formulae for the calculation of the various time scales are provided in Appendix A. Figure 7.2.10 shows the average daily ultra-sidereal and ultra-antisidereal modulation over the four year period. The amplitude of modulations in both these time scales are significantly lower than those observed in the sidereal, antisidereal and solar modulations, which indicates that there is unlikely to be a significant annual solar phase modulation present. This result is also consistent with the good agreement between the phases of the solar modulation in each of the years during the 2006-2009 period.

Discussion of Sidereal Anisotropy

There are two main anisotropies that we would expect to observe at these energies in sidereal time; the "tail-in" and "loss cone" anisotropies. The "tail-in" anisotropy is observed at energies below around 10^4 GeV as a directional excess around 6 hours in local sidereal time at a declination of $\sim -24°$ and in a cone with a half opening angle of $\sim 68°$, which coincides with the direction of the heliomagnetotail. The "loss-cone" anisotropy, however, is mainly observable only in the northern hemisphere and is characterised by a deficit at around 12 hours in local sidereal time at a declination of $\sim 20°$. Both these anisotropies are described in Section 4.4. Results from low energy muon experiments conducted at Mt Norikura, Nagoya, Sakashita and Hobart

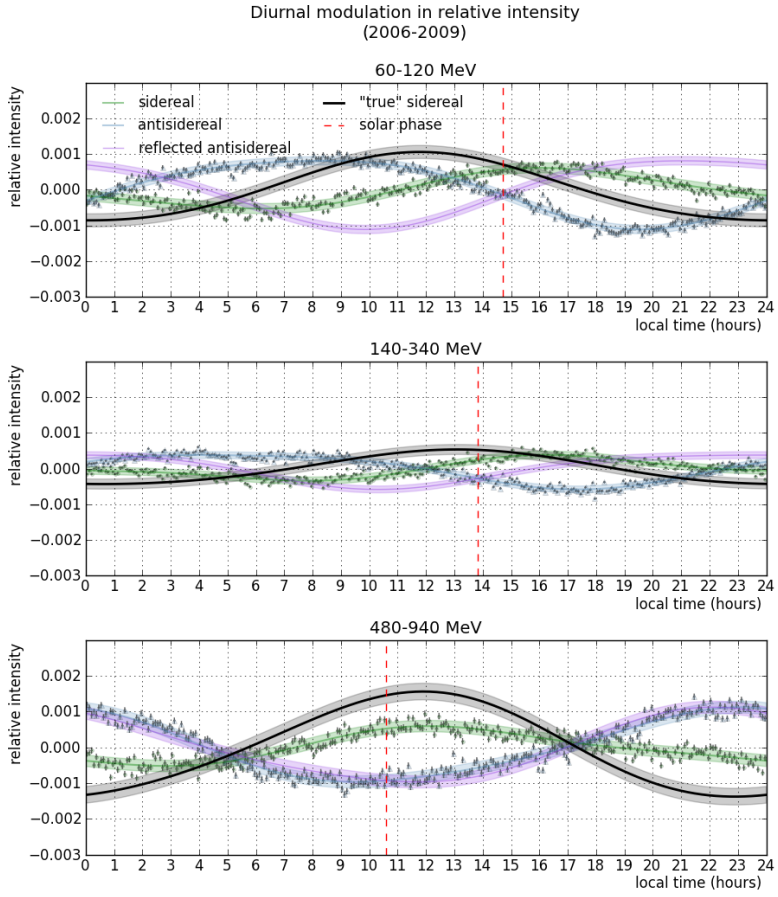

a)

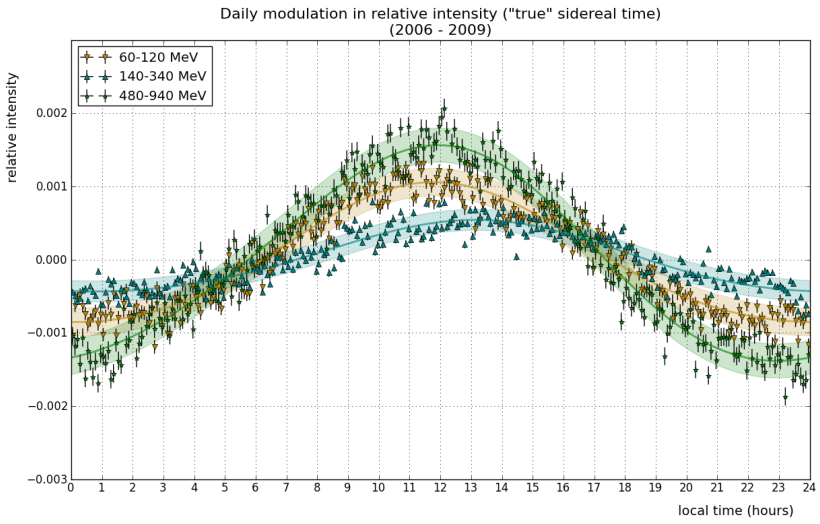

b)

Figure 7.2.7: Shows a) the process of removing the spurious signal produced in the apparent sidereal signal by an amplitude modulation in solar time. The antisidereal modulation (blue) is reflected about the solar vector (red dotted) to represent the spurious component in the sidereal signal (purple) which is then subtracted from the apparent sidereal signal (green) to leave only the "true" sidereal signal (thick black). Panel b) shows the resulting "true" sidereal signal over the 2006 to 2009 period.

year	deposition E range (MeV)	1st harmonic ("true" sidereal)		2nd harmonic ("true" sidereal)		χ^2/ndf	# events
		amplitude ($\times 10^{-2}\%$)	phase ($hours$)	amplitude ($\times 10^{-2}\%$)	phase ($hours$)		
2006	60-120	7.57±0.21	11.04±0.11	1.70±0.21	2.88±0.24	1007.86 / 282	6455335
	140-340	6.32±0.22	13.20±0.13	1.42±0.22	2.83±0.29	3335.88/ 282	6455335
	480-940	14.53±0.28	11.28±0.07	3.29±0.28	1.41±0.16	934.28 / 282	6455335
2007	60-120	10.94±0.34	10.51±0.12	1.98±0.34	10.38±0.33	1031.3 / 282	2956811
	140-340	5.62±0.22	9.38±0.15	0.07±0.22	11.85±6.19	1592.06 / 282	2956811
	480-940	17.26±0.55	13.30±0.12	1.58±0.55	7.36±0.66	1151.32 / 282	2956811
2008	60-120	7.54±0.33	14.14±0.17	2.35±0.33	1.80±0.27	1023.33 / 282	3046778
	140-340	3.59±0.23	14.77±0.24	1.08±0.23	11.93±0.40	1892.26 / 282	3046778
	480-940	12.83±0.41	10.55±0.12	3.78±0.41	5.53±0.21	879.58 / 282	3046778
2009	60-120	18.76±0.38	13.30±0.08	6.33±0.38	10.12±0.12	1171.89 / 282	3044581
	140-340	4.93±0.20	14.09±0.16	1.46±0.20	8.90±0.26	1532.05 / 282	3044581
	480-940	12.25±0.43	13.24±0.13	9.59±0.43	10.69±0.09	899.4 / 282	3044581
2006-2009	60-120	9.55±0.16	11.89±0.06	0.96±0.16	11.54±0.31	1199.64 / 282	15503505
	140-340	4.88±0.12	13.01±0.10	0.48±0.12	1.48±0.48	2545.5 / 282	15503505
	480-940	14.61±0.20	11.54±0.05	1.25±0.20	1.14±0.30	965.2 / 282	15503505

Table 7.2.3: Amplitude and phase of the first and second harmonics to the derived "true" sidereal signal for 2006 to 2009 at each deposition energy range.

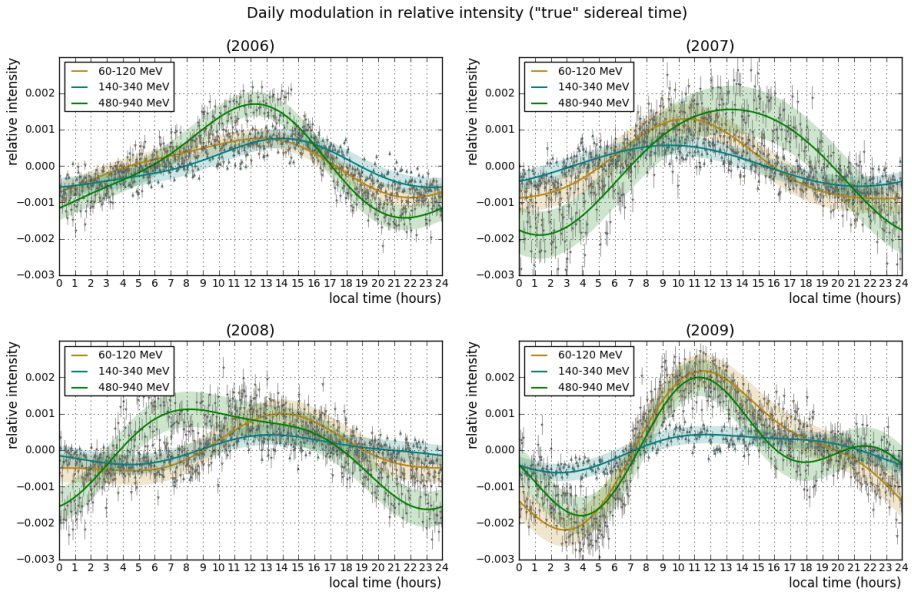

Figure 7.2.8: Shows the "true" sidereal signal derived by subtracting the antisidereal signal reflected about the solar vector from the apparent sidereal signal for each of the years 2006 to 2009.

[46] (shown in Figure 7.2.11) show the presence of these two anisotropies with the "loss-cone" anisotropy becoming less evident in the results from Hobart which, unlike the other three experiments, is in the southern hemisphere.

At higher energies, the TibetASγ and Milagro experiments both also observe an excess at around 6 hours local sidereal time as well as a deficit at around 12 hours. The results from the two experiments are shown in Figures 7.2.12 and 7.2.13, and have modal energies of 3 TeV and 6 TeV respectively [106, 53]. We see that the Milagro experiment observes a sidereal anisotropy with a greater magnitude than found at any of the deposition energy ranges in either apparent or "true" sidereal time ($\sim$ 0.25%), whereas the TibetASγ results show a similar amplitude to that found

The IceCube experiment also observes this excess around 6 hours in local sidereal time with a median energy of 20 TeV[63]. However, there is no longer a deficit evident around 12 hours local sidereal time (as expected from a southern hemisphere observatory), instead a deficit lies at around 15 hours local sidereal time. These results are shown in Figure 7.2.14 at a median energy of 20 TeV. Both the Milagro and IceCube antisidereal modulations are very small, indicating very little contamination from solar frequency effects.

In contrast, it can be seen that the results obtained from the charge histograms appear to exhibit different properties. The relative intensity modulation in apparent sidereal time over the whole 2006-2009 period (Figure 7.2.2) shows an excess at

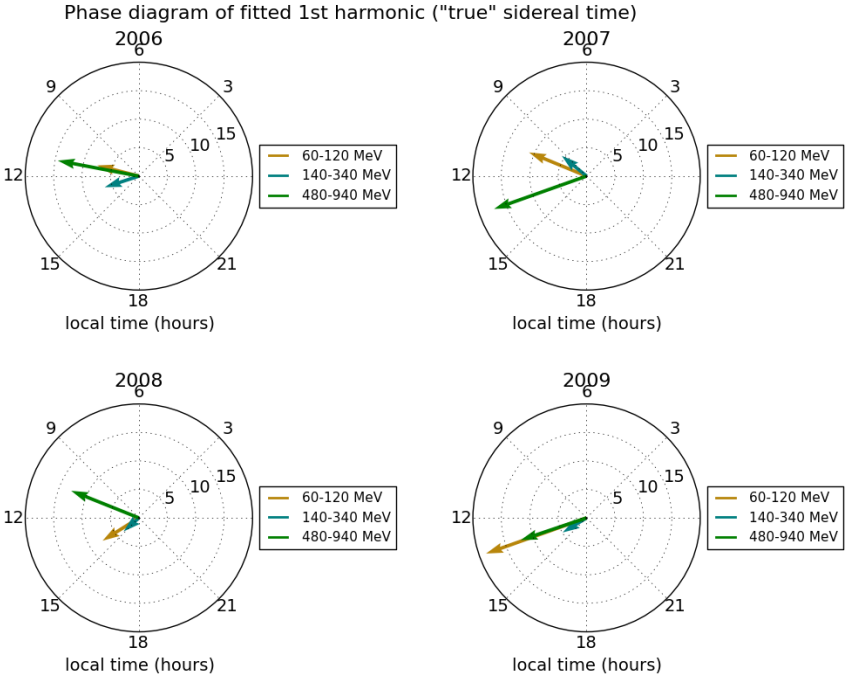

a)

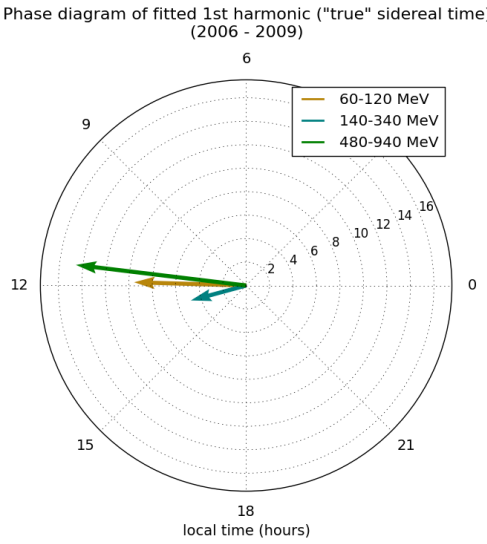

b)

Figure 7.2.9: Phase diagrams of the fitted first harmonic to the derived "true" sidereal modulation of the relative intensity for a) each of the years 2006-2009 and b) the total 4 year period. The amplitudes are multiplied by 10^4. Note the improvement in year to year agreement when compared to the apparent sidereal modulation shown in Figure 7.2.3).

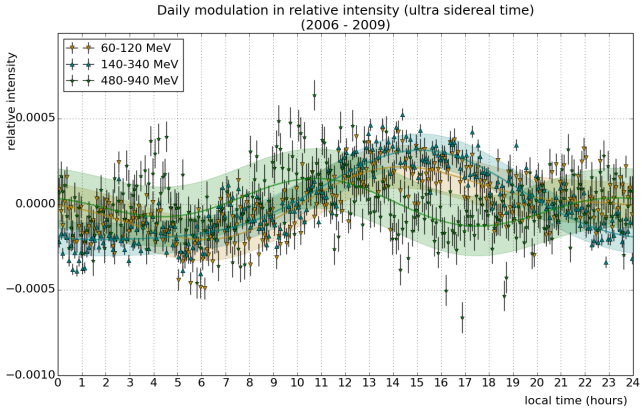

a)

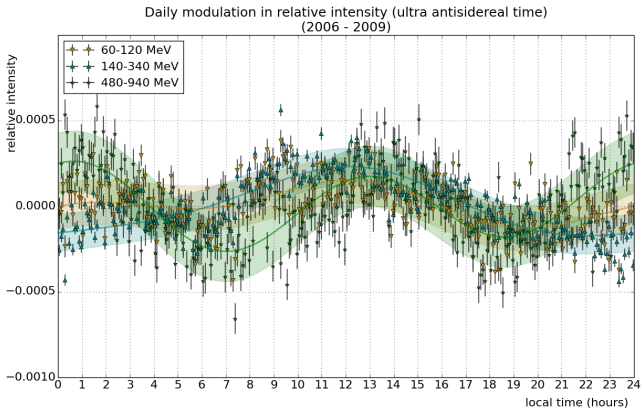

b)

Figure 7.2.10: The average diurnal relative intensity modulation in a) ultra-sidereal time and b) ultra-antisidereal time over the four year period 2006-2009. Note that these modulations are close to the level of statistical noise.

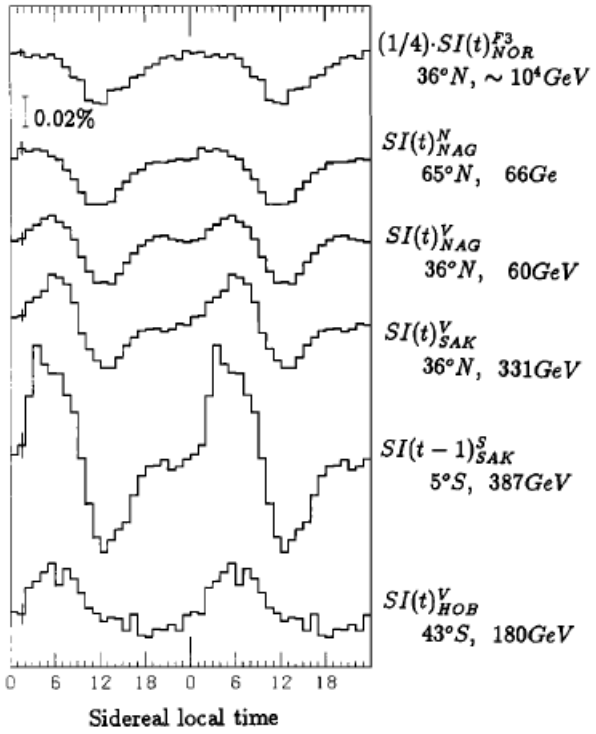

Figure 7.2.11: Shows the variation in local sidereal time from muon experiments conducted at Mt Norikura, Nagoya, Sakashita and Hobart. The median energy and latitude of the central viewing direction for each telescope are also shown [46].

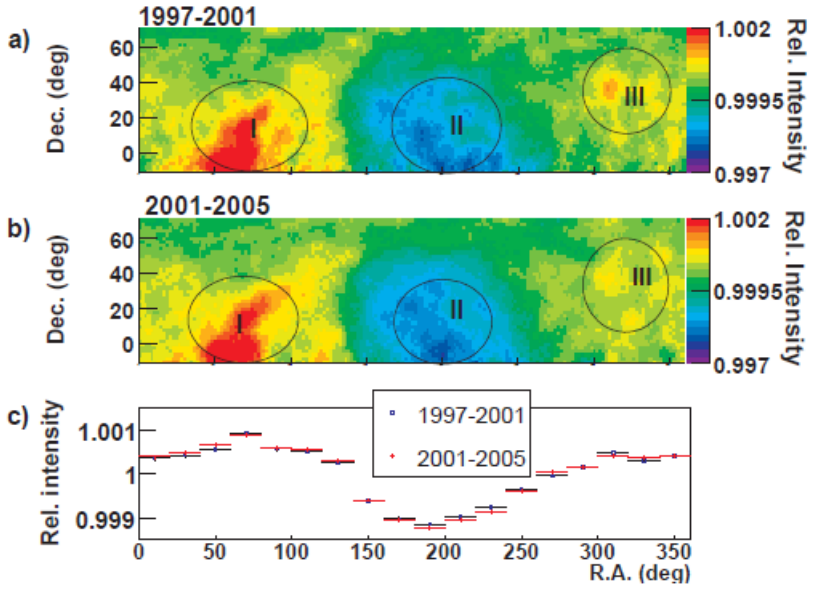

Figure 7.2.12: Relative intensity of the cosmic ray flux as observed by Tibet ASγ over the periods a) 1997 to 2001 and b) 2001 to 2005, with a modal energy of 3 TeV. Circles I and II show the tail-in and loss-cone anisotropy regions, while circle III indicates another anisotropy component near the Cygnus region. Panel c) shows the one-dimensional projection of the 2D maps in right ascension [106].

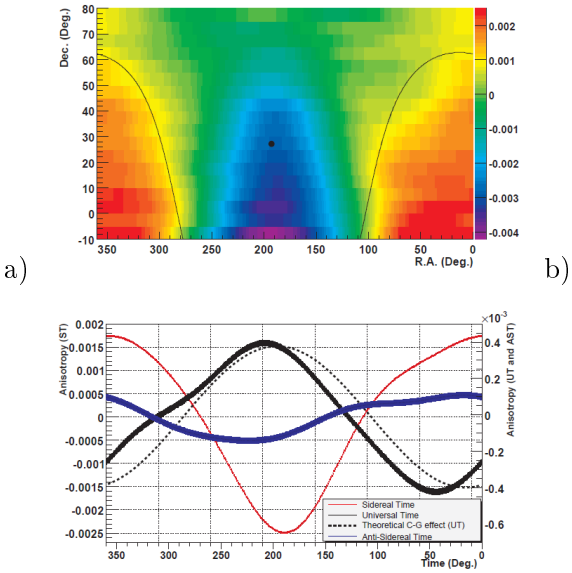

Figure 7.2.13: Shows a) a harmonic fit to the observed fraction intensity fluctuation from isotropy at Milagro over the years 2000-2007 with the position of the galactic equator and north pole overlayed (black line and dot respectively). The 1-dimensional projection of the analysed anisotropies are then plotted in b) in sidereal time (red) and universal solar time (black) as well as in anti-sidereal time (blue). The expected Compton-Getting anisotropy component in universal solar time arising from the Earth's motion around the Sun is also plotted (black dotted). The width of each of the curves indicates the statistical error [53].

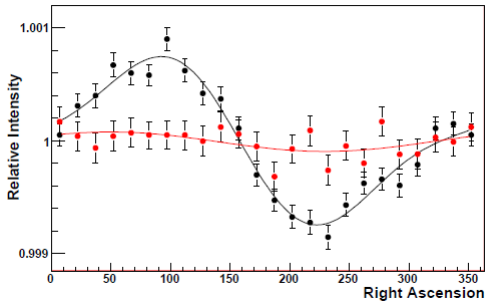

Figure 7.2.14: Shows the one-dimensional projection of the relative intensity of the cosmic ray fluctuations observed at IceCube with a median energy of 20 TeV in sidereal time (black) as well as the antisidereal modulation (red) [63].

around 17 hours at the lower two deposition energy ranges and at around 12 hours in the higher 480-940 MeV deposition energy band. The middle energy range, spanning the muon peak of the histogram (140-340 MeV), shows the most consistency over the 2006-2009 period with maxima at around 17 and 14 hours in the apparent and "true" sidereal modulations respectively. During the 2006-2009 period, the lowest energy data (60-120 MeV) shows a signal consistent with the 140-340 MeV data in the apparent sidereal modulation. However, in the derived "true" sidereal modulation, it begins to exhibit characteristics closer to those of the higher energy data (480-940 MeV).

The amplitudes of both the apparent and "true" sidereal anisotropies are comparable to those observed in the experiments described above and in Section 4.4. Over the full 2006-2009 period, the amplitude of the measured apparent sidereal anisotropy was found to be of the order 0.05% at both the 60-120 MeV and 480-940 MeV deposition energy bands, and of the order of 0.03% over the deposition energy band spanning the muon peak (140-340 MeV). The amplitude of the derived "true" sidereal anisotropy was found to be slightly larger over the same period; $\sim 0.10\%$ at the lowest energy range, $\sim 0.05\%$ over the energy range spanning the muon peak, and $\sim 0.15\%$ at the highest energy range. We see that the Milagro experiment observes a sidereal anisotropy with a greater magnitude than found at any of the deposition energy ranges in either apparent or "true" sidereal time ($\sim 0.25\%$), whereas the TibetASγ and IceCube results show a comparable amplitude to those found here. It must be noted, though, that the energies of these experiments remain higher than those observed using the charge histogram data and so cannot be compared directly.

From the plot of the solar activity (Figure 7.0.3) we see that, within this inactive period, 2009 had the least amount of solar activity. It is interesting to note that the corresponding phase diagram for the "true" sidereal modulation in this year (Figure 7.2.9) shows consistent 1st harmonic phases at each of the deposition energy ranges. Indeed, the phases of the "true" sidereal 1st harmonic for the total 2006-2009 period are also very similar between all three deposition energy ranges.

However, the significant disagreement between the phases of observations by the other experiments described above and those found in this study led to the concern that some spurious effect was being introduced. A likely point for this to occur was in the atmospheric correction of the data. Since this was done by initially performing the pressure correction and then the temperature correction, a concern was that the temperature correction may have re-introduced some solar frequency diurnal modulation. This was especially a concern in the lowest energy band where the calculated temperature coefficient was larger (see Figure 5.3.7). A short check was performed in which only the pressure correction was applied. This resulted in small differences in the solar modulation as expected, but negligible change to the

sidereal modulation.

Because of the very low amount of solar activity during the 2006-2009 period, it is possible that the anisotropies observed at these very low energies are 'real' signals that are usually masked by solar noise. However, since the amplitude of the antisidereal modulation was of a similar magnitude to that of the apparent sidereal modulation, it is likely that, even during this inactive period, the signal remains so dominated by solar effects at these energies that a 'real' sidereal modulation is no longer discernible. A contrast of the 2006-2009 results with those of the more active 2005 are described below.

7.3 Solar activity (2005)

The 2006 to 2009 time period was chosen for the majority of this research since it spanned a period of low solar activity. During the year 2005, however, there were several significant solar events. Figure 7.3.1 shows the timeseries of the 2005 data averaged into 6-hourly intervals, and in which it can be seen that the data carry considerably more variation than those spanning 2006 to 2009 (see Figure 7.0.2). In particular, two events stand out during which time a sharp decrease in the intensity can be seen; the first occurs during January (∼day 18), while the second occurs during September (∼day 253). These are Forbush decreases associated with the occurrence of solar activity and are described in more detail in Section 4.1.1. We will more closely investigate the September event here.

Figure 7.3.2 shows the timeseries zoomed in to September, averaged over one-hourly periods, during which time a Forbush decrease can be seen occurring on the 11th followed by a slow return to the original intensity over a period of several days. The Forbush decrease can be seen as a decrease of around 4% in the lower two energy ranges, while the 480-940 MeV energy range shows a slightly smaller decrease of around 3%.

This same Forbush decrease was observed by neutron monitors across the world. Figure 7.3.3 shows the decrease as seen at Oulu in Finland and at Moscow, Russia where drops in the background neutron counting rate of around 10% can be seen, followed by the slow return to the previous counting rate of several days. This decrease coincided with a jump in the solar wind speed from around 260 km/s on the 10th to more than 800 km/s on the 11th as reported in the spaceweather archive located at `http://spaceweather.com/archive.php`. September was a month of significant sunspot activity, in particular a very large sunspot (sunspot 798) was responsible for several flares. Figure 7.3.4 shows the Sun's appearance on 11 September 2005 with the dominant sunspots labeled.

It is evident that the data contained in these charge histograms is highly sensitive

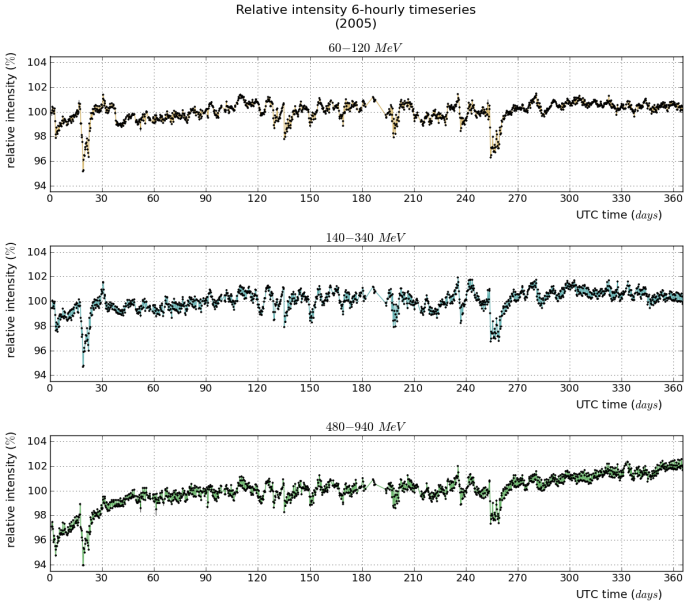

Figure 7.3.1: Timeseries of the data spanning 2005 averaged into 6-hourly time periods.

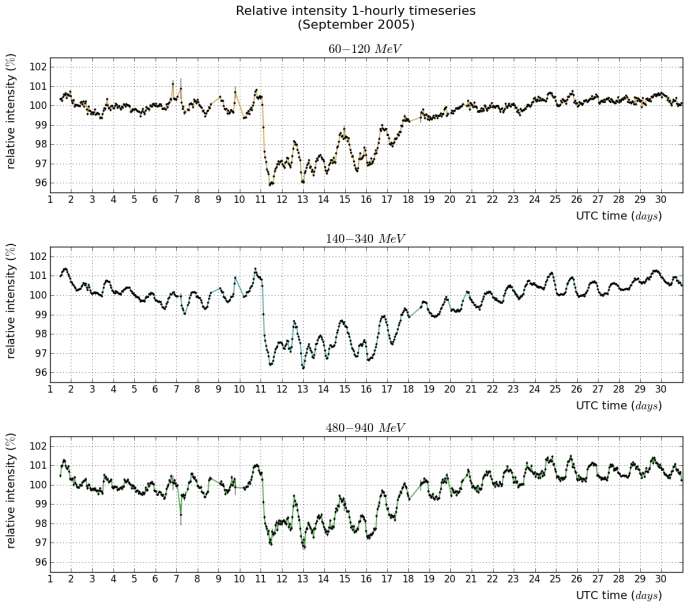

Figure 7.3.2: The one-hourly averaged timeseries signal observed during September at each of the three deposition energy ranges, a Forbush decrease can be seen occurring on the 11th followed by a slow return to the original intensity over a period of several days.

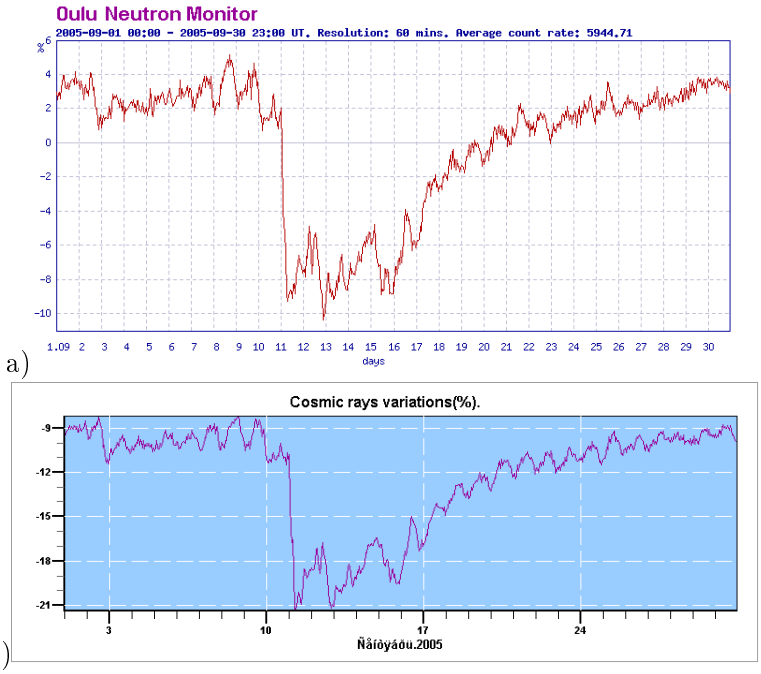

Figure 7.3.3: The September 2005 Forbush decrease as observed at neutron monitors located at a) Oulu and b) Moscow. A sharp decrease of around 10% can be seen occurring on the 11th with a slow return to the original counting rate over the period of several days. Both plots display the counting rate following atmospheric correction. Figures taken from `http://cosmicrays.oulu.fi/` and `http://cr0.izmiran.rssi.ru/mosc/main.htm`.

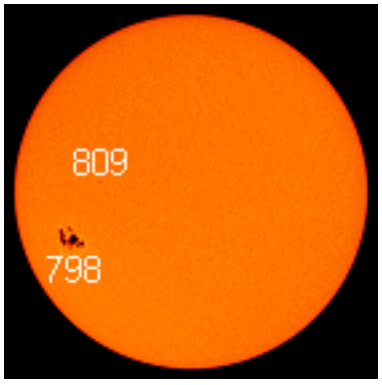

Figure 7.3.4: The Sun's appearance on 11 September 2005 showing the very dominant sunspot 798 which was responsible for much of the flare activity during the month. Image taken from `http://spaceweather.com/archive.php?day=11&month=09&year=2005&view=view`.

to solar effects and the higher energy range of the data discussed here compared to neutron monitors is responsible for the somewhat reduced level of modulation.

Diurnal modulation (solar time)

The amount of solar activity during 2005 may also have significantly altered the behaviour of the average daily modulation in solar time. Figure 7.3.5 shows a comparison of this average daily intensity modulation for 2005 with that of the more inactive period 2006-2009. As observed above, in Section 7.1, each of the years 2006-2009 display similar average daily intensity modulations in solar time. However, we can see that this modulation in 2005 differs from the 2006-2009 period at each of the 3 deposition energy ranges investigated with the amplitude and phase of the fitted curves listed in Table 7.3.1. Figure 7.3.6 shows the fitted first harmonic of the solar modulation plotted as a phase diagram for 2005 and the full 2006-2009.

In the 60-120 MeV and 140-340 MeV ranges, the phase can be seen to be consistent between the 2005 and the 2006-2009 periods. However the amplitude at the lowest energy range is considerably reduced from an average amplitude of the first harmonic of $\sim$0.27 % to only $\sim$0.17 %, while the 140-340 MeV amplitude remains consistent between these time periods.

At the higher energy range (480-940 MeV) the more significant difference between these time periods is evident. In contrast to the lowest energy range, the amplitude of the 1st harmonic in this energy range can be seen to approximately double for the 2005 period in comparison to that of the 2006-2009 period. The amplitude of the 2nd harmonic significantly reduces so that the 2005 signal becomes dominated by only the 1st harmonic with a phase of around 12 hours in local solar time. It may be that, during this time of increased solar activity, the relative proportion of solar radiation and galactic cosmic rays in the higher energy range becomes closer to that of the lower two energy ranges.

In its present configuration, the scaler mode of the Pierre Auger observatory (described in Section 3.1.5) spans a deposition energy range of around 15 to 100 MeV, which is approximately equivalent to that of the 60-120 MeV band investigated here. In its initial configuration, however, it collected data from all energies $\gtrsim$ 5 MeV [67], thus spanning almost the entire charge histogram. Figure 7.3.7 shows the solar modulation that is observed with the scaler data both before and after the atmospheric pressure correction during the initial configuration [67]. Before the application of the pressure correction, a twice diurnal modulation is apparent in the scaler data, which is absent in the corrected data. The pressure corrected data show an amplitude of around 0.25% with a phase of $\sim$14 hours in local time. These are consisted with those observed in the lower energy ranges of the charge histogram (as expected since these deposition energy ranges have the greater contribution to the

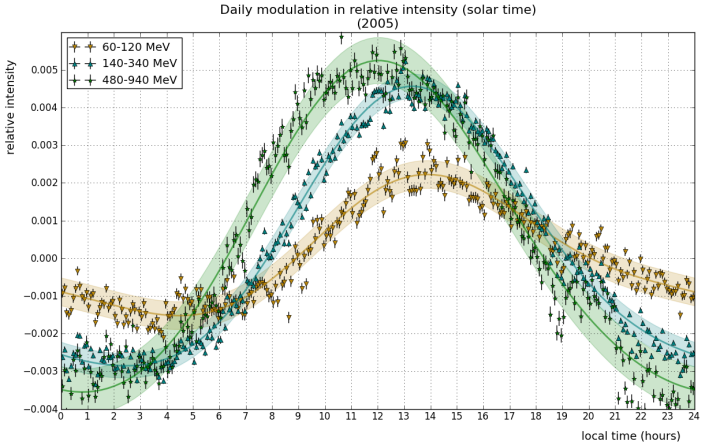

a)

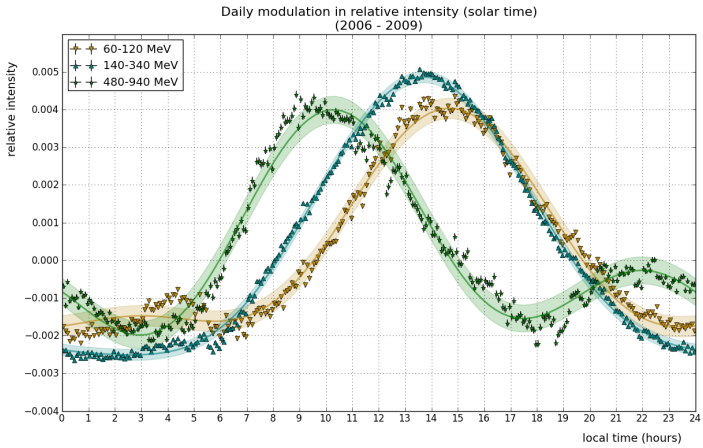

b)

Figure 7.3.5: Comparison of the average daily intensity modulation in solar time during a) 2005 with b) the total period 2006-2009. Differences in the modulations, especially in the phase, at each deposition energy range are evident.

year	deposition E range (MeV)	1st harmonic (solar)		2nd harmonic (solar)		χ^2/ndf	# events
		amplitude ($\times 10^{-1}\%$)	phase ($hours$)	amplitude ($\times 10^{-1}\%$)	phase ($hours$)		
2005	60-120	1.76±0.03	14.62±0.07	0.42±0.03	1.09±0.14	2068.09 / 282	3901834
	140-340	3.68±0.03	13.55±0.03	0.61±0.03	0.95±0.09	4277.01 / 282	3901834
	480-940	4.38±0.05	12.28±0.04	0.46±0.05	11.45±0.21	3038.68 / 282	3901834
2006-2009	60-120	2.76±0.02	14.60±0.03	1.02±0.02	2.73±0.04	5157.01/ 282	15503505
	140-340	3.68±0.01	13.77±0.01	0.80±0.01	1.61±0.03	5686.72/ 282	15503505
	480-940	2.15±0.03	10.59±0.05	1.64±0.03	10.17±0.04	4155.44/ 282	15503505

Table 7.3.1: Amplitude and phase of the fitted first and second harmonics to the solar data for 2005 and for the period 2006-2009 at each deposition energy range with the χ^2/ndf of the fit to the data.

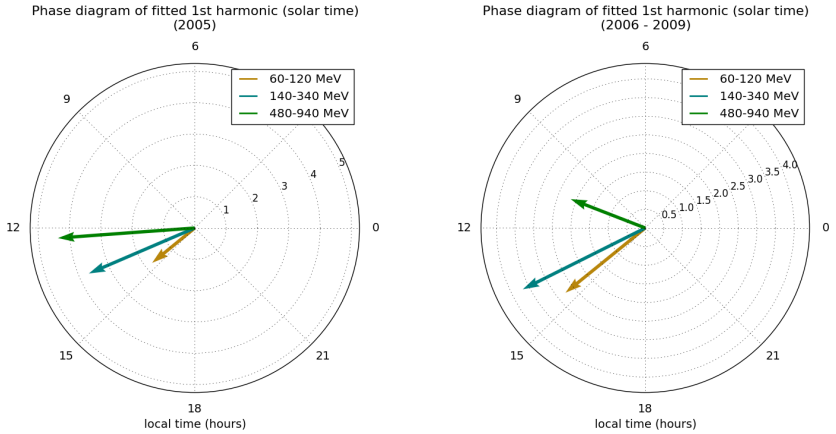

a) b)

Figure 7.3.6: Phase diagrams of the fitted first harmonic to the solar modulation of the relative intensity for a) 2005 and b) the full 2006-2009 period. The amplitudes are multiplied by 10^3.

scaler counting rate), see Figure 7.0.1.

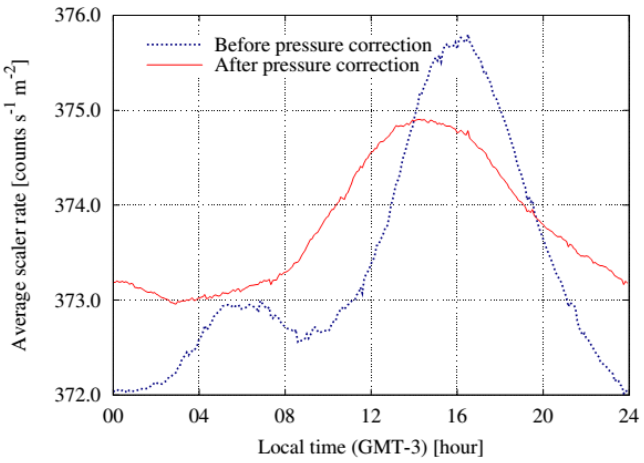

Figure 7.3.7: The average diurnal modulation in local solar time scaler rate, showing both the pressure corrected and uncorrected data for the period spanning 01 March to 20 September 2005 [67].

Diurnal modulation (sidereal time)

As with the diurnal modulation in solar time described above, it is expected that the enhanced solar activity during 2005 may also have influenced the behaviour of the average diurnal modulation in sidereal time. Figure 7.3.8 shows a comparison between the average modulation in relative intensity in apparent sidereal time during

2005 with that of the period 2006-2009 during which time there was less solar activity. However, unlike the modulation in solar time, which was very consistent across the whole 2006-2009 period, the apparent sidereal modulation does not display the same consistency. Table 7.3.9 lists the fitted first and second harmonic to the apparent sidereal modulation for 2005 and for the full 2006-2009 period, while Figure 7.3.9 shows the fitted first harmonic to the apparent sidereal modulation plotted as a phase diagram for 2005, the full 2006-2009 period as well as for each of the years 2006-2009 individually.

As with the 2006-2009 period, during 2005 there is a significant signal in the antisidereal frequency which indicates the presence of a spurious component to the apparent sidereal signal. Figure 7.3.10 shows a comparison of the apparent sidereal and antisidereal signals with the fitted first and second harmonic amplitude and phase listed in Table 7.3.3. Figure 7.3.11 then shows the derived "true" sidereal signals. The amplitude and phase of the 1st and 2nd harmonics of the derived "true" sidereal signal are listed in Table 7.3.4, while Figure 7.3.12 shows the fitted first harmonic to the derived "true" sidereal modulation plotted as a phase diagram for 2005, the full 2006-2009 period as well as for each of the years 2006-2009 individually.

It can be seen that the signal in 2005 has a much greater noise level than during any of the years 2006-2009, which increases in the derivation of the "true" sidereal signal. We would expect that, during a time of increased solar activity, the contamination from solar effects would also be increased. However, it can also be seen that the higher energy band (480-940 MeV) shows modulation in the derived "true" sidereal similar to that in 2009 around 12 hours in local time and a minima around 4 and 18 hours. This maximum around 12 hours local time is broadly consistent with the 2006-2009 average as well as with years 2006, 2007 and 2009.

The middle energy range (140-340 MeV) shows more consistency over the 2006-2009 period with a maximum at around 17 and 14 hours in the apparent and "true" sidereal modulations respectively. The 2005 data show a similar maximum but, again, a much greater noise level.

During the 2006-2009 period, the lowest energy data (60-120 MeV) shows a consistent signal with the 140-340 MeV data in the apparent sidereal modulation. However, in the derived "true" sidereal modulation, it begins to exhibit characteristics closer to those of the higher energy data (480-940 MeV). During 2005, this no longer appears to be the case, with the modulations at all three energies displaying similar characteristics in both the apparent and "true" sidereal modulations. It must, however, be emphasised that the "true" sidereal signal obtained by the correction for a spurious signal of such magnitude, may no longer retain significance.

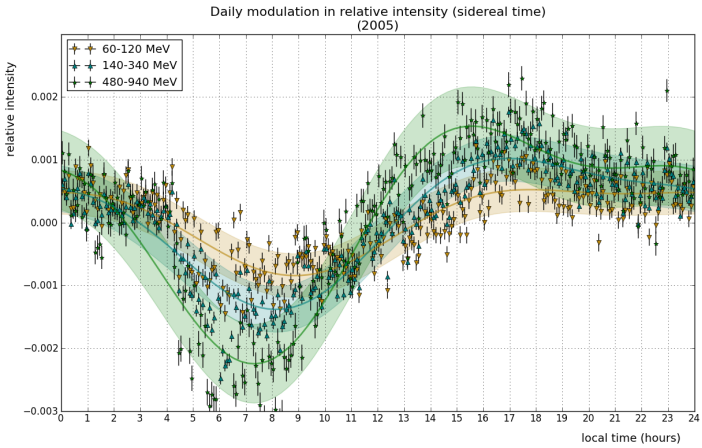

a)

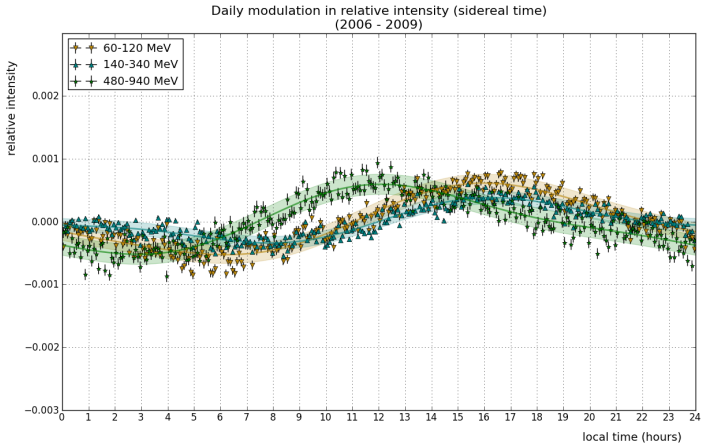

b)

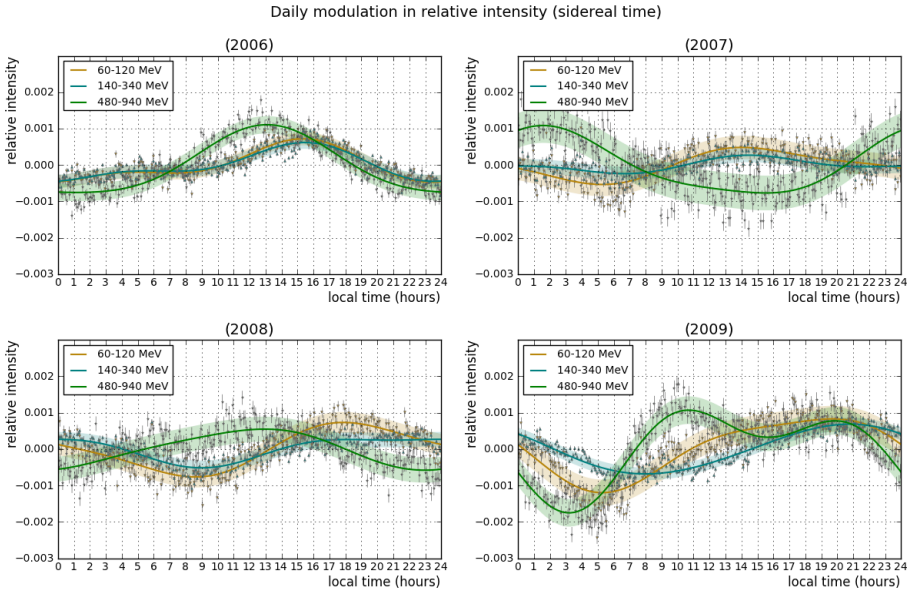

c)

Figure 7.3.8: Comparison of the average daily intensity modulation in sidereal time during a) 2005 with b) the total period 2006-2009 as well as c) each of the years 2006-2009 separately.

year	deposition E range (MeV)	1st harmonic (sidereal)		2nd harmonic (sidereal)		χ^2/ndf	# events
		amplitude ($\times 10^{-2}\%$)	phase ($hours$)	amplitude ($\times 10^{-2}\%$)	phase ($hours$)		
2005	60-120	6.55±0.29	20.76±0.17	2.27±0.29	2.89±0.24	1880.12 / 282	3901834
	140-340	10.96±0.30	19.52±0.10	3.57±0.30	2.57±0.16	4729.04 / 282	3901834
	480-940	16.34±0.53	18.72±0.12	7.19±0.52	1.60±0.14	2935.5 / 282	3901834
2006-2009	60-120	5.43±0.12	14.60±0.03	0.99±0.12	2.82±0.23	1311.72 / 282	15503505
	140-340	3.03±0.09	13.77±0.01	1.17±0.09	2.62±0.14	2616.90 / 282	15503505
	480-940	5.10±0.13	10.59±0.05	1.27±0.13	1.64±0.20	919.10 / 282	15503505

Table 7.3.2: Amplitude and phase of the fitted first and second harmonics to the apparent sidereal data for 2005 and for the period 2006-2009 at each deposition energy range with the χ^2/ndf of the fit to the data.

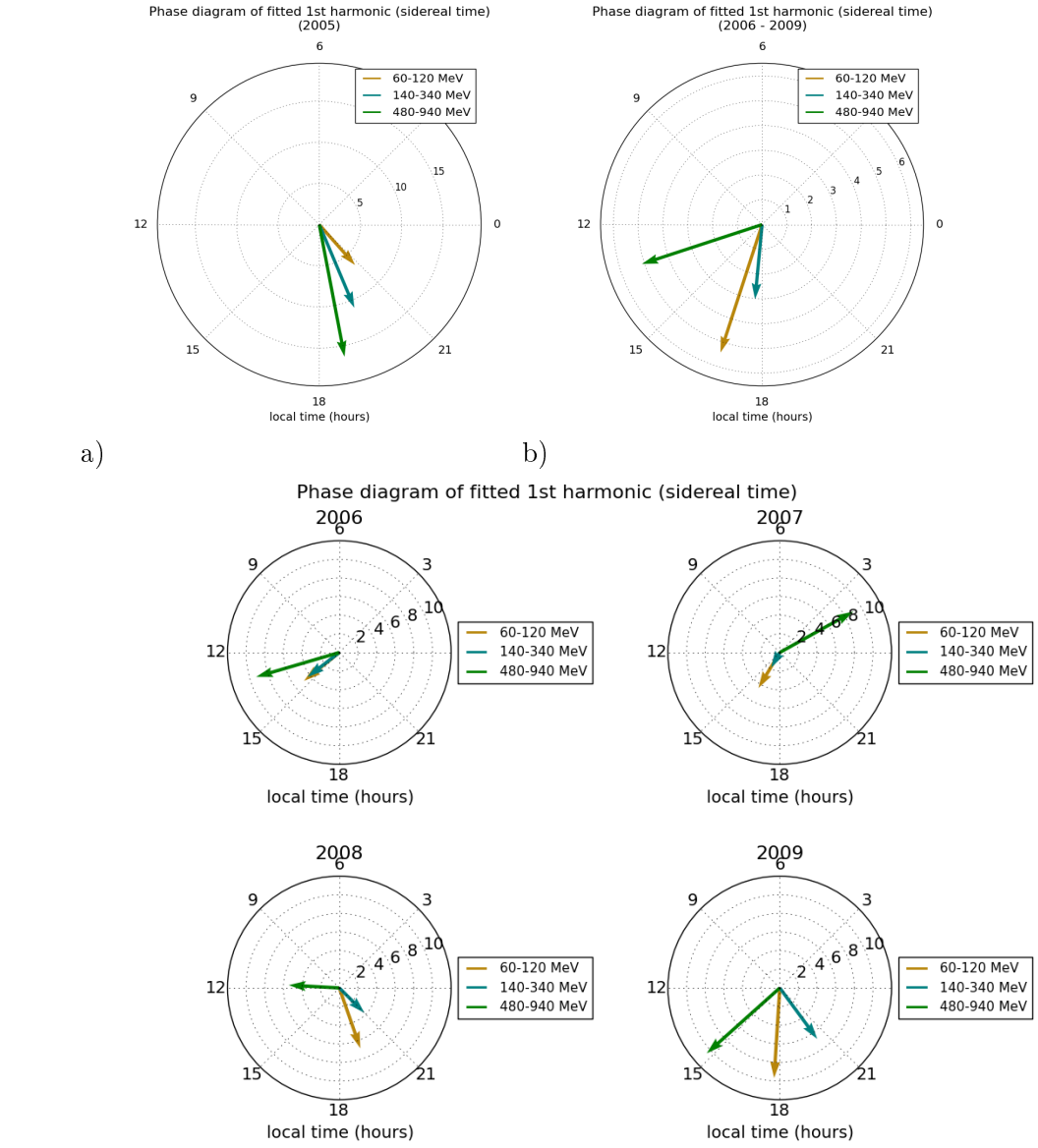

Figure 7.3.9: Phase diagrams of the fitted first harmonic to the apparent sidereal modulation of the relative intensity for a) 2005 and b) the full 2006-2009 period as well as c) each of the years 2006-2009 individually. The amplitudes are multiplied by 10^4.

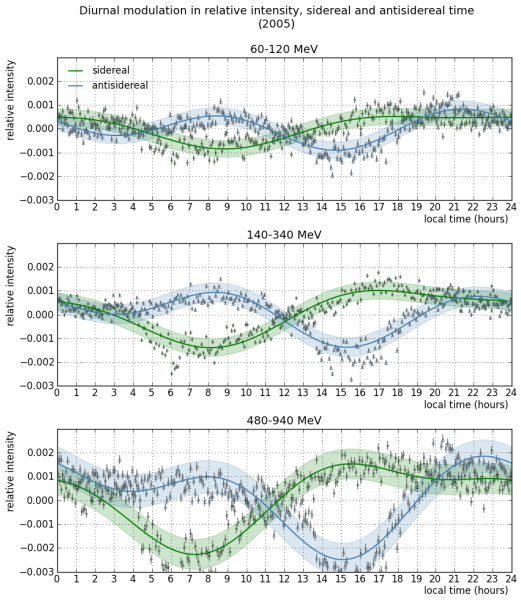

a)

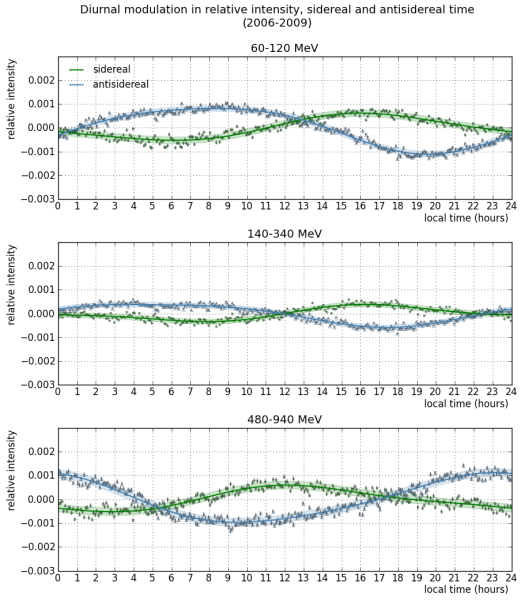

b)

Figure 7.3.10: Comparison of the average daily modulation in sidereal time with that of the antisidereal component at each deposition energy range for a) 2005 and b) 2006-2009.

year	deposition E range (MeV)	1st harmonic (antisidereal)		2nd harmonic (antisidereal)		χ^2/ndf	# events
		amplitude ($\times 10^{-2}\%$)	phase ($hours$)	amplitude ($\times 10^{-2}\%$)	phase ($hours$)		
2005	60-120	3.50±0.29	1.30±0.33	6.35±0.29	8.91±0.09	1922.92 / 282	3901834
	140-340	7.07±0.33	3.71±0.18	7.32±0.33	9.24±0.09	5735.05 / 282	3901834
	480-940	15.32±0.57	2.22±0.14	11.24±0.57	9.37±0.10	3560.64 / 282	3901834
2006-2009	60-120	9.57±0.10	7.73±0.04	1.49±0.10	1.26±0.13	934.8 / 282	15503505
	140-340	4.76±0.08	5.18±0.06	0.99±0.08	11.58±0.15	2259.86 / 282	15503505
	480-940	10.22±0.14	22.52±0.05	1.41±0.14	0.22±0.19	1022.21 / 282	15503505

Table 7.3.3: Amplitude and phase of the fitted first and second harmonics to the antisidereal data for 2005 and for the period 2006-2009 at each deposition energy range with the χ^2/ndf of the fit to the data.

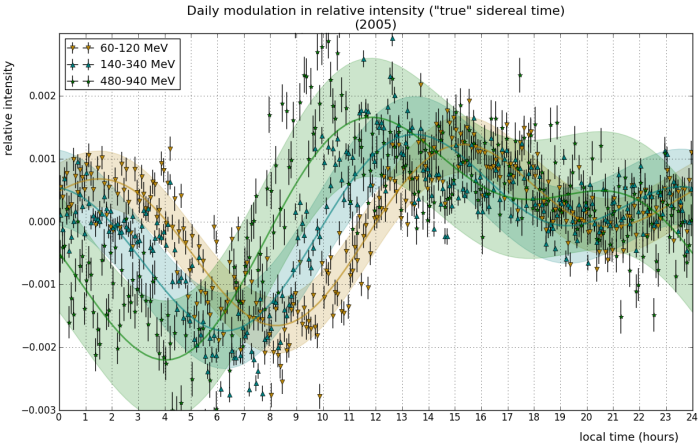

a)

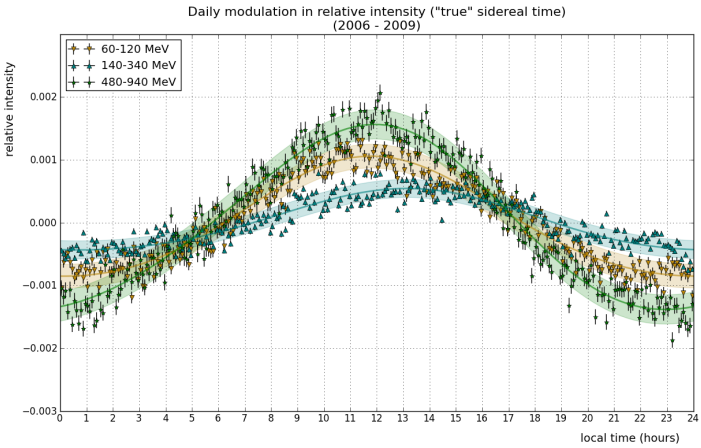

b)

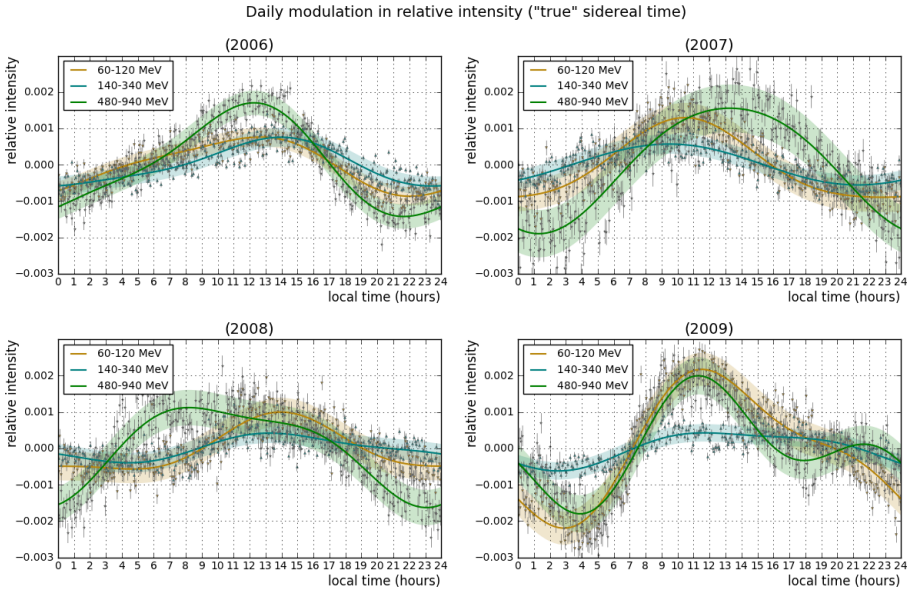

c)

Figure 7.3.11: Comparison of the derived "true" sidereal diurnal modulation during a) 2005 with b) the total period 2006-2009 as well as c) each of the years 2006-2009 separately. The "true" sidereal signal is derived by subtracting the antisidereal signal reflected about the solar vector from the apparent sidereal signal.

year	deposition E range (MeV)	1st harmonic ("true" sidereal)		2nd harmonic ("true" sidereal)		χ^2/ndf	# events
		amplitude ($\times 10^{-2}\%$)	phase ($hours$)	amplitude ($\times 10^{-2}\%$)	phase ($hours$)		
2005	60-120	8.38±0.38	19.18±0.17	8.61±0.37	2.49±0.08	1549.73 / 282	3901834
	140-340	9.47±0.50	16.86±0.20	8.72±0.50	0.66±0.11	6562.61 / 282	3901834
	480-940	14.56±0.77	14.82±0.21	8.30±0.78	10.55±0.18	3312.15 / 282	3901834
2006-2009	60-120	9.55±0.16	11.89±0.06	0.96±0.16	11.54±0.31	1199.64 / 282	15503505
	140-340	4.88±0.12	13.01±0.10	0.48±0.12	1.48±0.48	2545.5 / 282	15503505
	480-940	14.61±0.20	11.54±0.05	1.25±0.20	1.14±0.30	965.2 / 282	15503505

Table 7.3.4: Amplitude and phase of the first and second harmonics to the derived "true" sidereal signal for 2006 to 2009 at each deposition energy range.

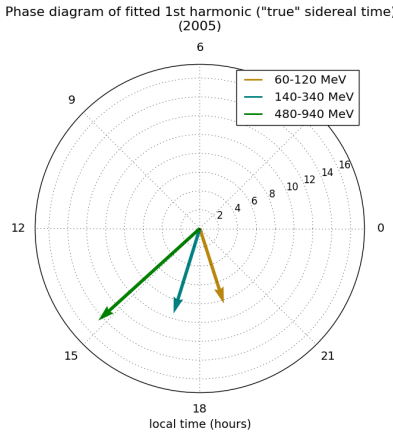

a)

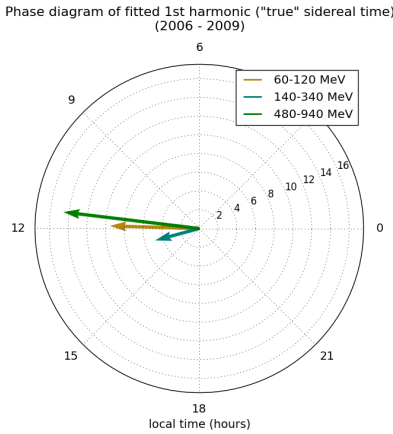

b)

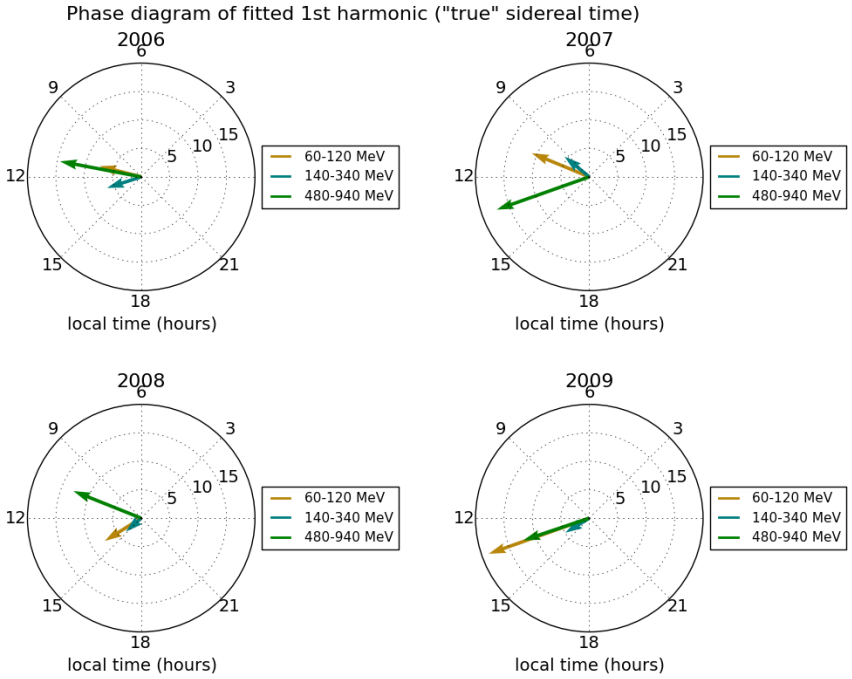

c)

Figure 7.3.12: Phase diagrams of the fitted first harmonic to the derived "true" sidereal modulation of the relative intensity for a) 2005 and b) the full 2006-2009 period as well as c) each of the years 2006-2009 individually. The amplitudes are multiplied by 10^4.

8: Conclusions and Future Possibilities

The vast quantities of low energy data collected by the Pierre Auger Observatory in the process of collecting data on the highest energy cosmic rays allowed a study to be made into the behaviour of the very low energy cosmic ray flux in the Southern Hemisphere. The low solar activity of the 2006 to 2009 period also presented a unique opportunity to study the behaviour of the very low cosmic ray flux which would otherwise be overwhelmed by the solar variations during more active periods, and the charge histograms produced as part of the Pierre Auger Observatory's surface detector calibration process were used to investigate the behaviour of the low cosmic ray flux during this time.

Numerical simulations were performed of low energy extensive air showers, as well as of a single water-Cherenkov station's response to the secondary particles reaching the ground. From these, it was possible to crudely determine the energy ranges of the primary particles contributing to the deposition energies spanned by the charge histograms. Much of the histogram was found to be populated by particles produced by very low energy cosmic ray primaries with energies less than 10^2 GeV. However, a transition region was also identified where the primary energies appeared to increase to 10^2-$10^{2.5}$ GeV. The lower energy region was divided into two separate deposition energy ranges for study: one of which spanned the single particle peak produced by the passage of unaccompanied muons, and the other at lower deposition energies where the particle contribution was more ambiguous. From the results of the numerical simulations and the expected particle contribution to the charge histograms, it was decided to investigate the following deposition energy regions: 60-120 MeV, 140-340 MeV and 480-940 MeV.

Following the calibration, quality cuts and atmospheric corrections to the charge histogram data described in Chapter 5, analyses of the solar and sidereal anisotropies were performed over the 2006-2009 period as well as over the more active 2005 period. The results of these analyses are described in detail in Chapter 7 and are summarised here.

Solar Anisotropy

The solar anisotropy was found to be very consistent across each year of the 2006 to 2009 period, though varying between deposition energy bands. The lower two deposition energy bands showed evidence of a maximum at ∼14 hours local time whereas the higher energy band showed a maximum at ∼10 hours in local time. The galactic cosmic rays are expected to show evidence of the Compton-Getting effect associated with the Earth's motion around the Sun which would appear as a maximum in the solar diurnal modulation at ~ 6 hours local solar time. The phase decrease that is evident between the lower two deposition energy bands and the 480-940 MeV band may be indicative of an increase in the proportion of galactic cosmic ray's contributing to this energy range.

The more active 2005 period no longer showed this marked separation of the phases between the lower two deposition energy bands and the 480-940 MeV band, which is consistent with a decrease in the relative contribution of low energy galactic cosmic rays to the higher energy deposition energy band.

The data are consistent with the Auger scalers which were independently analysed using a quite different technique.

Sidereal Anisotropy

At the energies expected from the results of the numerical simulations, there were two main anisotropies which were expected to be evident in the sidereal modulation: the "tail-in" and "loss-cone" anisotropies described in Section 4.4. The "tail-in" anisotropy is observed at energies below around 10^4 GeV as a directional excess around 6 hours in local sidereal time at a declination of $\sim -24^\circ$ and in a cone with a half opening angle of $\sim 68^\circ$, which coincides with the direction of the heliomagneto-tail. The "loss-cone" anisotropy, however, is mainly observable only in the northern hemisphere and is characterised by a deficit at around 12 hours in local sidereal time at a declination of $\sim 20^\circ$.These anisotropies are observed at TeV energies with experiments such as Tibet ASγ, Milagro and IceCube as well as at lower energies by experiments at Mt Norikura, Sakashita and Hobart.

At the very low energies spanned by the charge histograms, it was a concern that the magnitude of the solar influence may be too great to reliably discern a signal in sidereal time. Indeed, when correcting for any spurious signal resulting from an annual solar amplitude modulation, it was found that the antisidereal signal was of a similar magnitude to that of the sidereal signal.

It was anticipated that the 480-940 MeV deposition energy band may show evidence of some "true" low energy anisotropy in sidereal time during the 2006-2009 period, since the results from the solar anisotropy analysis indicated that there may

be a greater proportion of galactic cosmic rays contributing to this energy band. The apparent sidereal anisotropy exhibited very little consistency between the years 2006 to 2009 at the higher energy band, whereas the lower deposition energy bands did appear quite consistent. The derived "true" sidereal anisotropy, while slightly more consistent, remained inconclusive. The lowest energy deposition band began to exhibit similar behaviour to that of the 480-940 MeV band, while the 140-340 MeV band showed only a small phase difference from its corresponding apparent sidereal signal.

Of particular note was the consistency between the years 2006-2009 of both the antisidereal and "true" sidereal 1st harmonics in comparison to the uncorrected apparent sidereal modulation.

The amplitudes of both the apparent and "true" sidereal anisotropies were found to be comparable to those of the other experiments. However, the phases of the signal at any deposition energy range in either the apparent or "true" sidereal time do not agree with either of the expected anisotropies described above. Because of the very low amount of solar activity during the 2006-2009 period, it is possible that the anisotropies observed at these very low energies are 'real' signals that are usually masked by solar noise. However, since the amplitude of the antisidereal modulation was of a similar magnitude to that of the apparent sidereal modulation, it is likely that, even during this inactive period, the signal remains so dominated by effects with a solar period at these energies that a 'real' sidereal modulation is no longer discernible.

It was hoped that a contrast with the sidereal anisotropy observed in 2005 may shed light on the validity of any sidereal signal in the 2006-2009 period. In contrast to the behaviour of the three energy levels in the 2006-2009 period, both the apparent and derived "true" sidereal signals during the more active 2005 period showed similar characteristics across all three energy ranges. As with the signal evident in solar time, this may indicate a partial contribution of galactic cosmic rays to the charge histograms which is significantly less during periods of increased solar activity.

However, even with the enhanced flux of lower energy cosmic rays during the very inactive 2006-2009 period, it must be concluded the signal remains so dominated by solar effects at these energies that a 'real' sidereal anisotropy is no longer discernible.

Transient Solar Effects

The data available in the charge histograms also proved highly sensitive to transient solar effects such as Forbush Decreases. In addition to the solar and sidereal anisotropies present in the 2005 data, Section 7.3 also describes the timeseries of the 2005 histogram data. When binned into hourly intervals, these transient effects can be seen with a high degree of detail. A comparison between a Forbush decrease event

in September of 2005 observed by neutron monitors at Oulu and Moscow with the same event as observed with the charge histogram data, showed great similarity. The charge histogram data showed a significantly lower intensity change ($\sim 4\%$) than was recorded by the two neutron monitors ($\sim 10\%$) which are sensitive to lower primary particle energies.

Improvements and Future Work

The crudity of the numerical simulations performed to represent the energy range contribution to the charge distributions was, perhaps, the greatest limiting factor to this research. More detailed and sophisticated simulations in the future may provide a better resolution of the primary particle energies contributing to the charge histograms across the deposition energies spanned. A more robust method of simulating the shower core placement and detector response would limit the number of scaling corrections which potentially introduced large errors into the simulation results.

More stringent requirements and checks on the stability and operational continuity of the sub-array are also an important improvement in any future work since, at such low energies, the statistics remain high. This may reduce the unexplained fluctuations and instabilities evident in both the corrected and uncorrected time-series data. It was noted that a twice diurnal modulation remained evident in the solar frequency at each of the energy ranges and, consequently, it may be worthwhile re-evaluating the process by which the atmospheric corrections (particularly the barometric correction) are implemented in any future work. The presence of this second harmonic in the solar anisotropy may well be indicative of some under-corrected instrumental or meteorological effect.

While 2005 was a more active period than 2006-2009, the solar activity during this time was still relatively low (with a smoothed International Sunspot Number of around only 30). Results of a future study spanning a period of high solar activity (around solar maximum) could be contrasted with those found here and would assist in isolating those behaviours that are correlated with solar activity. Also, the 11 year solar cycle means that we are, again, approaching a time of low solar activity. The new cosmic ray detectors and enhancements to existing experiments at the Pierre Auger Observatory mean that it may be possible to perform a similar analysis over the next solar minimum in both the northern and southern hemispheres.

Appendix A: Timescale Formulae

The mean sidereal time at Greenwich can be calculated using the following formula [97],[123]:

$$\theta_0 = 280.46061837 + 360.98564736629(J - 2451545.0) \tag{A.0.1}$$

where J is the Julian data and θ_0 is in degrees. The Julian date 2451545.0 corresponds to the J_{2000} epoch (i.e. 2000, January 1.5 UTC). From this, a similar formula can then be derived for other time scales in the form:

$$T_n = A_n + B_n(J - J_{2000}) \tag{A.0.2}$$

where there are $(365.24219 + n)$ revolutions in a tropical year. That is, solar time is calculated as T_0 while sidereal time is then T_1. A_n is the phase at J_{2000} and B_n is the number of degrees by which the time increases per solar day. The phase is chosen such that all T_i coincide at the same instant every year; solar and sidereal time always coincide at the September equinox (around September 20).

n	*time scale*	A_n	B_n
-2	ultra-antisidereal	339.07876326	358.02870526742
-1	antisidereal	79.53938163	359.01435263371
0	solar	180.00000000	360.00000000000
1	sidereal	280.46061837	360.98564736629
2	ultra-sidereal	20.92123674	361.97129473258

Appendix B: Relative Abundances

The cosmic ray flux ratios for nuclei in the range H-Fe. The relative abundances are taken from Grieder's "*Cosmic Rays at Earth*"[121] and converted into a fraction of the total abundance. Table B.0.1 shows this relative abundance ordered from most abundant to least while Figure B.0.1 shows the relative abundance as a function of atomic number.

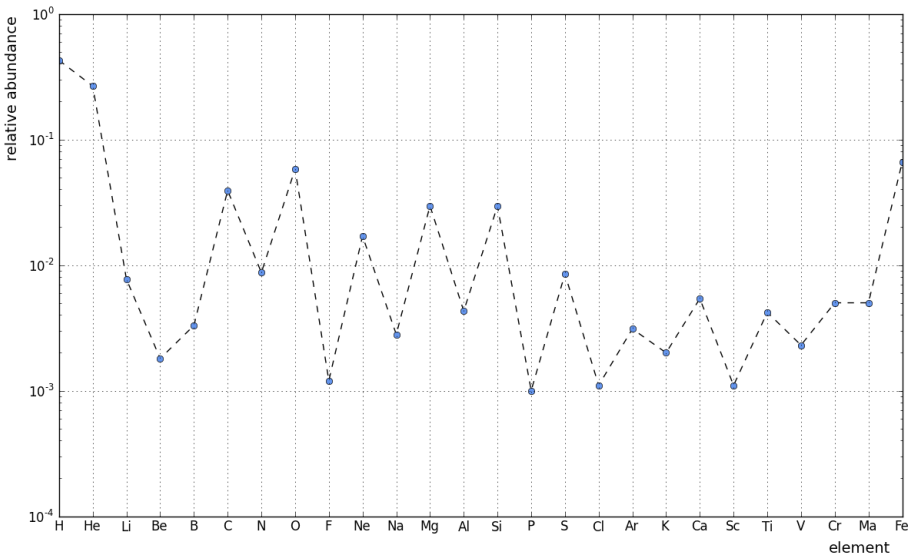

Figure B.0.1

element	atomic number (Z)	relative abundance
H	1	0.4260
He	2	0.2661
Fe	26	0.0659
O	8	0.0581
C	6	0.0392
Mg	12	0.0296
Si	14	0.0295
Ne	10	0.0170
N	7	0.0087
S	16	0.0085
Li	3	0.0077
Ca	20	0.0054
Cr	24	0.0050
Mn	25	0.0050
Al	13	0.0043
Ti	22	0.0042
B	5	0.0033
Ar	18	0.0031
Na	11	0.0028
V	23	0.0023
K	19	0.0020
Be	4	0.0018
F	9	0.0012
Cl	17	0.0011
Sc	21	0.0011
P	15	0.0010

Table B.0.1

Appendix C: Error Analysis and Propagation

This section briefly describes the analysis and propagation of the uncertainties in each quantity. The process is divided into two sections: the calibration and correction of the raw charge histogram data, and the subsequent analysis of the resulting data.

C.1 Data calibration and correction

Raw Histograms:

For n counts in bin i, $\sigma_{n_i} = \sqrt{n_i}$. So, when we convert this count to a rate such that $r_i = \frac{n_i}{61}$, then $\sigma_{r_i} = \frac{\sigma_{r_i}}{61} = \frac{\sqrt{n_i}}{61} = \sqrt{\frac{r_i}{61}}$

Atmospheric corrections (pressure):

For a counting rate r in bin i, the pressure corrected rate r_{pc_i} was calculated such that:

$$r_{pc_i} = r_i(1 - \bar{\alpha_i}\Delta P)$$

where $\bar{\alpha_i}$ is the average fractional pressure coefficient (hPa^{-1}) across all PMTs in the subarray of stations surviving the quality cuts on operation and performance, ΔP is the difference between the measured and mean pressure values (hPa) such that $\Delta P = P - \bar{P}$.

The uncertainty in α_i for each PMT of each station is output from the fitting process. The uncertainty in $\bar{\alpha_i}$ contains two components; the uncertainty of each individualα_i contributing to$\bar{\alpha_i}$, and the standard deviation of the distribution of α_i. Since the contribution due to the uncertainty of each individual α_i is small with respect to that of the standard deviation σ_α, the uncertainty in $\bar{\alpha_i}$ then becomes:

$$\sigma_{\bar{\alpha_i}} = \frac{\sigma_\alpha}{\sqrt{N}}$$

where N is the number of PMTs in the subarray of stations surviving the quality cuts on operation and performance.

The systematic uncertainty in each measurement P, $\sigma_{P_S} = 0.2$ hPa, while the error in the mean $\sigma_{\bar{P}} = \frac{\sigma_P}{\sqrt{N_P}}$ where σ_P is the standard deviation of the distribution of

all N_p pressure measurements (since the systematic contribution to this uncertainty is negligible). We then determine the uncertainty in the difference ΔP to be:

$$\begin{aligned}\sigma_{\Delta P} &= \sqrt{\sigma_{P_S}^2 + \sigma_{\bar{P}}^2} \\ &= \sqrt{\sigma_{P_S}^2 + \frac{\sigma_P^2}{N_P}}\end{aligned}$$

and so the resulting uncertainty in the pressure corrected rate r_{pc_i} becomes:

$$\sigma_{r_{pc_i}} = \sqrt{\sigma_{r_i}^2 + \left(\bar{\alpha_i}\Delta P\sigma_{r_i}\right)^2 + \left(r_i\Delta P\sigma_{\bar{\alpha}_i}\right)^2 + \left(r_i\bar{\alpha_i}\sigma_{\Delta P}\right)^2}$$

Atmospheric corrections (temperature):

The temperature correction is applied in a similar manner following the pressure correction such that the temperature corrected rate $r_{tpc_i}$is:

$$r_{tpc_i} = r_{pc_i}1 - \beta_i\Delta T \tag{C.1.1}$$

However, the temperature coefficient β_i used, for histogram bin i, is that calculated for each individual PMT rather than the average across all PMTs. Consequently the uncertainty in the temperature coefficient $\sigma_{\beta_i}$is simply that output from the fitting process.

The difference between the measured and mean temperature ΔT ($^{\mathrm{o}}$) is calculated by $\Delta T = T - \bar{T}$ with each temperature measurement having a systematic uncertainty $\sigma_{T_S} = 0.2\ ^{\mathrm{o}}$. As with the pressure measurements, the uncertainty in the mean temperature is given by $\sigma_{\bar{T}} = \frac{\sigma_T}{\sqrt{N_T}}$ where σ_T is the standard deviation of the distribution of all N_T temperature measurements (since the systematic contribution to this uncertainty is, again, very small). The uncertainty in ΔT then becomes:

$$\sigma_{\Delta T} = \sqrt{\sigma_{T_S}^2 + \frac{\sigma_T^2}{N_T}}$$

with the resulting uncertainty in the temperature corrected rate r_{tpc_i} then given by:

$$\sigma_{r_{tpc_i}} = \sqrt{\sigma_{r_{pc_i}}^2 + \left(\beta_i\Delta T\sigma_{r_{pc_i}}\right)^2 + \left(r_{pc_i}\Delta T\sigma_{\beta_i}\right)^2 + \left(r_{pc_i}\beta_i\sigma_{\Delta T}\right)^2}$$

C.2 Analysis

Calculation of the fractional intensity:

In order to compare the counting rates between different PMTs and stations, the mean counting rate $\bar{r_{c_i}}$ in each bin i was determined for each individual PMT (following atmospheric correction), and the counting rate r_{tpc_i} reported as a fractional deviation from this mean value. That is:

$$r_{frac_i} = \frac{r_{tpc_i} - \bar{r_{c_i}}}{\bar{r_{c_i}}}$$

Again, the uncertainty in the mean counting rate is given by $\sigma_{\bar{r_{c_i}}} = \frac{\sigma_{r_{c_i}}}{\sqrt{N_h}}$, where $\sigma_{r_{c_i}}$ is the standard deviation of the distribution of corrected counting rates from all N_h histograms contributing to the mean.

The resulting uncertainty in the fractional intensity r_{frac_i} then becomes:

$$\begin{aligned} \sigma_{r_{frac_i}} &= \sqrt{\left(\frac{\sigma_{r_{tpc_i}}}{\bar{r_{c_i}}}\right)^2 + \left(\frac{r_{tpc_i}\sigma_{\bar{r_{c_i}}}}{\bar{r_{c_i}}^2}\right)^2} \\ &\approx \frac{\sigma_{r_{tpc_i}}}{\bar{r_{c_i}}} \end{aligned}$$

Average daily modulations:

The daily modulations were then calculated by converting the gps time to the Julian date and then to the local time frame to be investigated (timescale conversion formulae given in Appendix A). This local time was then averaged over 5 minute intervals and over the corresponding interval of every day. As with the determination of the mean of the pressure coefficients (described above), there are two main contributions to the uncertainty in each 5 minute average; the uncertainty of each individual rate contributing to this average, and the standard deviation of the distribution of rates. The contribution from the uncertainty in each individual rate is negligible compared to the standard deviation and so the uncertainty in each 5 minute average becomes:

$$\sigma_{\bar{r_{5min}}} = \frac{\sigma_{r_{5min}}}{\sqrt{N_{5min}}}$$

where N_{5min} is the number of values of r_{frac} contributing to the 5 minute average.

Harmonic analysis:

The harmonic analysis of the daily modulation was performed in the same manner for each time frame with the first and second harmonics being determined by a fit

of the data to a function of the form:

$$\sum_{i=1}^{2} A_i \cos\left(\frac{\pi}{12} i\,(t-\phi_i)\right) + B$$

where (A_i, ϕ_i) are the amplitude and phase of the ith harmonic, while t is the local time in hours and B is a constant. The uncertainty in the fit parameters (A_i, ϕ_i) were returned during the fit as well as the χ^2/ndf.

Antisidereal correction:

The apparent sidereal signal was modified to correct for the presence of a spurious signal resulting from an amplitude modulation in the solar frequency. This spurious component appears in the antisidereal frequency with the same amplitude as in the sidereal frequency, but reflected in phase about the solar vector. The correction then involves the subtraction of the antisidereal signal (reflected about the solar vector) from the apparent sidereal signal such that:

$$\begin{aligned} A_{truesid} \cos 2\pi\left[(N+1)\,t + \phi_{truesid}\right] &= A_{appsid} \cos 2\pi\left[(N+1)\,t + \phi_{appsid}\right] \\ &\quad - A_{asid} \cos 2\pi\left[(N+1)\,t + \phi_{refasid}\right] \end{aligned}$$

where $A_{truesid}$, A_{appsid} and A_{asid} are the 'true' sidereal, apparent sidereal and antisidereal amplitudes, and $\phi_{truesid}$, ϕ_{appsid} and $\phi_{refasid}$ are the 'true' sidereal, apparent sidereal and reflected antisidereal phases respectively. The uncertainty in the derived 'true' sidereal signal was then estimated by adding the uncertainty in the apparent sidereal signal and antisidereal signal in quadrature.

References

[1] V. Hess, *Phys. Zeitschr.* **13**, 1084 (1912).

[2] R. Clay & B. Dawson, *Cosmic Bullets: High Energy Particles in Astrophysics*, Addison-Wesley (1997).

[3] J. Blümer, R. Engel & J. R. Hörandel, *Progress in Particle and Nuclear Physics* **63**(2), 293 – 338 (2009).

[4] P. Auger *et al.*, *Rev. Mod. Phys.* **11**, 288–291 (1939).

[5] J. Linsley, *Phys. Rev. Lett.* **10**, 146–148 (1963).

[6] C. D. Anderson, *Phys. Rev.* **43**, 491–494 (1933).

[7] J. C. Street & E. C. Stevenson, *Phys. Rev.* **52**, 1003–1004 (1937).

[8] T. K. Gaisser & T. Stanev, *Nuclear Physics A* **777**(0), 98 – 110 (2006).

[9] J. R. Hörandel, *Astroparticle Physics* **19**(2), 193 – 220 (2003).

[10] A. A. Penzias & R. W. Wilson, *The Astrophysical Journal* **142**, 419–421 (1965).

[11] K. Greisen, *Phys. Rev. Lett.* **16**, 748–750 (1966).

[12] G. T. Zatsepin & V. A. Kuz'min, *Soviet Journal of Experimental and Theoretical Physics Letters* **4**, 78 (1966).

[13] F. Salamida (The Pierre Auger Collaboration), *in Proceedings of the 32nd International Cosmic Ray Conference*, Beijing (2011).

[14] S. G. Mashnik, *arXiv preprint astro-ph/0008382* (2000).

[15] J. R. Hörandel, *Modern Physics Letters A* **22**(21), 1533–1551 (2007).

[16] W. Apel *et al.*, *Astroparticle Physics* **31**(2), 86–91 (2009).

[17] J. Abraham *et al.* (The Pierre Auger Collaboration), *Physics Letters B* **685**(4-5), 239–246 (2010).

[18] R. J. Protheroe & R. W. Clay, *Publications of the Astronomical Society of Australia* **21**(1), 1–22 (2004).

[19] A. M. Hillas, *Annual Review of Astronomy and Astrophysics* **22**, 425–444 (1984).

[20] T. K. Gaisser, *Cosmic rays and particle physics*, Cambridge University Press (1990).

[21] T. K. Gaisser & A. M. Hillas, *in International Cosmic Ray Conference*, volume 8, pp. 353–357 (1977).

[22] M. Unger *et al.*, *Nuclear Instruments and Methods in Physics Research Section A: Accelerators, Spectrometers, Detectors and Associated Equipment* **588**(3), 433 – 441 (2008).

[23] R. U. Abbasi *et al.*, *The Astrophysical Journal* **622**(2), 910 (2005).

[24] W. Heitler, *The quantum theory of radiation*, Courier Dover Publications (1954).

[25] T. Stanev, *High energy cosmic rays*, Springer (2010).

[26] J. R. Hörandel, *Reviews in Modern Astronomy, Cosmic Matter* **20**, 198 (2008).

[27] F. Aharonian *et al.* (The H.E.S.S. Collaboration), *Astrononomy and Astrophysics* **457**, 899–915 (2006).

[28] G. Askaryan, *Zhur. Eksptl'. i Teoret. Fiz.* **41** (1961).

[29] J. Jelley *et al.*, *Nature* **205**, 327–328 (1965).

[30] M. A. Lawrence, R. J. O. Reid & A. A. Watson, *Journal of Physics G: Nuclear and Particle Physics* **17**(5), 733 (1991).

[31] R. M. Tennent, *Proceedings of the Physical Society* **92**(3), 622 (1967).

[32] D. R. Bergman & J. W. Belz, *Journal of Physics G: Nuclear and Particle Physics* **34**(10), R359 (2007).

[33] M. Nagano & A. A. Watson, *Rev. Mod. Phys.* **72**, 689–732 (2000).

[34] D. J. Bird *et al.*, *The Astrophysical Journal* **424**, 491–502 (1994).

[35] R. Baltrusaitis *et al.*, *Nuclear Instruments and Methods in Physics Research Section A: Accelerators, Spectrometers, Detectors and Associated Equipment* **240**(2), 410 – 428 (1985).

[36] T. Abu-Zayyad *et al.*, *Nuclear Instruments and Methods in Physics Research Section A: Accelerators, Spectrometers, Detectors and Associated Equipment* **450**(2-3), 253 – 269 (2000).

[37] J. H. Boyer *et al.*, *Nuclear Instruments and Methods in Physics Research Section A: Accelerators, Spectrometers, Detectors and Associated Equipment* **482**(1-2), 457 – 474 (2002).

[38] R. U. Abbasi *et al.* (High Resolution Fly's Eye Collaboration), *Phys. Rev. Lett.* **92**, 151101 (2004).

[39] M. M. Winn *et al.*, *Journal of Physics G: Nuclear and Particle Physics* **12**(7), 653 (1986).

[40] M. Nagano *et al.*, *Journal of Physics G: Nuclear and Particle Physics* **18**(2), 423 (1992).

[41] H. Ohoka *et al.*, *Nuclear Instruments and Methods in Physics Research Section A: Accelerators, Spectrometers, Detectors and Associated Equipment* **385**(2), 268 – 276 (1997).

[42] M. Aglietta *et al.*, *Astroparticle physics* **21**(6), 583–596 (2004).

[43] M. Aglietta *et al.*, *Astroparticle physics* **21**(3), 223–240 (2004).

[44] M. Aglietta *et al.*, *The Astrophysical Journal Letters* **692**(2), L130 (2009).

[45] Solar-Terrestrial Environment Laboratory, *Nagoya Multi-Directional Muon Telescope* (http://www.stelab.nagoya-u.ac.jp/ste-www1/div3/muon/dbtext22.pdf).

[46] K. Nagashima, K. Fujimoto & R. M. Jacklyn, *Journal of Geophysical Research: Space Physics* **103**(A8), 17429–17440 (1998).

[47] V. Aynutdinov *et al.*, *Nuclear Instruments and Methods in Physics Research Section A: Accelerators, Spectrometers, Detectors and Associated Equipment* **567**(2), 433 – 437 (2006).

[48] P. Coyle (The ANTARES Collaboration), *in Proceedings of the 31st International Cosmic Rays Conference*, Łódź (2009).

[49] C. Spiering, *in American Institute of Physics Conference Series*, volume 1085, pp. 18–29 (2008).

[50] M. Amenomori *et al.* (Tibet ASγ Collaboration), *The Astrophysical Journal* **678**(2), 1165 (2008).

[51] M. Amenomori *et al.* (Tibet ASγ Collaboration), *The Astrophysical Journal* **711**(1), 119 (2010).

[52] M. Amenomori *et al.* (Tibet ASγ Collaboration), *Astrophysics and Space Science* **309**(1-4), 435–439 (2007).

[53] A. Abdo *et al.*, *The Astrophysical Journal* **698**(2), 2121 (2009).

[54] R. Atkins *et al.*, *Phys. Rev. Lett.* **95**(25), 251103 (2005).

[55] A. Falcone & J. Ryan, *Astroparticle Physics* **11**(1-2), 283 – 285 (1999).

[56] M. Mostafá (The HAWC Collaboration), *in Proceedings of the 33rd International Cosmic Ray Conference*, Rio de Janeiro (2013).

[57] A. Tepe (The HAWC Collaboration), *in Journal of Physics: Conference Series*, volume 375, p. 052026, IOP Publishing (2012).

[58] R. Abbasi *et al.*, *Nuclear Instruments and Methods in Physics Research Section A: Accelerators, Spectrometers, Detectors and Associated Equipment* **601**(3), 294 – 316 (2009).

[59] A. Karle *et al.* (The IceCube Collaboration), *arXiv preprint arXiv:1401.4496* (2014).

[60] S. Toscano (The IceCube Collaboration), *Nuclear Physics B-Proceedings Supplements* **212**, 201–206 (2011).

[61] F. Halzen, *in Journal of Physics: Conference Series*, volume 171, p. 012014, IOP Publishing (2009).

[62] A. Achterberg *et al.* (The IceCube Collaboration), *Astroparticle Physics* **26**, 155–173 (2006).

[63] R. Abbasi *et al.*, *The Astrophysical Journal Letters* **718**(2), L194 (2010).

[64] T. Stanev (The IceCube Collaboration), *arXiv preprint arXiv:1011.1879* (2010).

[65] C. Jui *et al.* (The Telescope Array Collaboration), *in Journal of Physics: Conference Series*, volume 404, p. 012037, IOP Publishing (2012).

[66] H. Kawai *et al.*, *Nuclear Physics B - Proceedings Supplements* **175-176**(0), 221 – 226 (2008).

[67] P. Abreu *et al.* (The Pierre Auger Collaboration), *Journal of instrumentation* **6**, P01003–1 (2011).

[68] I. Allekotte *et al.*, *Nuclear Instruments and Methods in Physics Research Section A: Accelerators, Spectrometers, Detectors and Associated Equipment* **586**(3), 409 – 420 (2008).

[69] X. Bertou *et al.*, *Nuclear Instruments and Methods in Physics Research Section A: Accelerators, Spectrometers, Detectors and Associated Equipment* **568**(2), 839 – 846 (2006).

[70] J. Abraham *et al.* (The Pierre Auger Collaboration), *Nuclear Instruments and Methods in Physics Research Section A: Accelerators, Spectrometers, Detectors and Associated Equipment* **613**(1), 29 – 39 (2010).

[71] D. Allard *et al.* (The Pierre Auger Collaboration), *in Proceedings of the 29th International Cosmic Ray Conference*, Pune (2005).

[72] C. Bonifazi, A. Letessier-Selvon & E. Santos, *Astroparticle Physics* **28**(6), 523 – 528 (2008).

[73] M. Ave, *in Proceedings of the 30th International Cosmic Ray Conference*, Merida (2007).

[74] J. Abraham *et al.* (The Pierre Auger Collaboration), *Phys. Rev. Lett.* **101**, 061101 (2008).

[75] M. Roth, *in Proceedings of the 30th International Cosmic Ray Conference*, Merida (2007).

[76] J. Abraham *et al.* (The Pierre Auger Collaboration), *Nuclear Instruments and Methods in Physics Research Section A: Accelerators, Spectrometers, Detectors and Associated Equipment* **620**(2-3), 227 – 251 (2010).

[77] B. Fick *et al.*, *Journal of Instrumentation* **1**(11), P11003 (2006).

[78] K. Loudec, *in 32nd International Cosmic Ray Conference*, Beijing (2011).

[79] P. Abreu *et al.* (The Pierre Auger Collaboration), *Astroparticle Physics* **34**(6), 368 – 381 (2011).

[80] F. Suarez (The Pierre Auger Collaboration), *in Proceedings of the 33rd International Cosmic Ray Conference*, Rio de Janeiro (2013).

[81] F. Sanchez (The Pierre Auger Collaboration), *in Proceedings of the 32nd International Cosmic Ray Conference*, Beijing (2011).

[82] T. H. Mathes (The Pierre Auger Collaboration), *in Proceedings of the 32nd International Cosmic Ray Conference*, Beijing (2011).

[83] J. Kelley (The Pierre Auger Collaboration), *in Proceedings of the 32nd International Cosmic Ray Conference*, Beijing (2011).

[84] F. Schröder (The Pierre Auger Collaboration), *in Proceedings of the 33rd International Cosmic Ray Conference*, Rio de Janeiro (2013).

[85] R. Gaïor (The Pierre Auger Collaboration), *in Proceedings of the 33rd International Cosmic Ray Conference*, Rio de Janeiro (2013).

[86] P. Blasi & E. Amato, *Journal of Cosmology and Astroparticle Physics* **2012**(01), 011 (2012).

[87] L. Sveshnikova, O. Strelnikova & V. Ptuskin, *Astroparticle Physics* **50**, 33–46 (2013).

[88] V. Ptuskin *et al.*, *Advances in Space Research* **37**(10), 1909–1912 (2006).

[89] C. Evoli *et al.*, *Physical review letters* **108**(21), 211102 (2012).

[90] K. Herbst *et al.*, *Journal of Geophysical Research: Atmospheres (1984–2012)* **115**(D1) (2010).

[91] A. Hundhausen, *in* K. Strong *et al.* (eds.), *The Many Faces of the Sun*, pp. 143–200, Springer New York (1999).

[92] S. E. Forbush, *Phys. Rev.* **51**, 1108–1109 (1937).

[93] V. F. Hess & A. Demmelmair, *Nature* **140**, 316 (1937).

[94] J. A. Simpson, *Phys. Rev.* **94**, 426–440 (1954).

[95] H. Cane, *Space Science Reviews* **93**(1-2), 55–77 (2000).

[96] A. H. Compton & I. A. Getting, *Phys. Rev.* **47**, 817–821 (1935).

[97] A. Smith, *The Cosmic Ray Anisotropy at High Energies (Ph.D. Thesis)*, University of Adelaide (1995).

[98] T. Thambyahpillai, *in* J. Osborne & A. Wolfendale (eds.), *Origin of Cosmic Rays*, volume 14 of *NATO Advanced Study Institutes Series*, pp. 37–59, Springer Netherlands (1975).

[99] P. Király *et al.*, *La Rivista del Nuovo Cimento* **2**(7), 1–46 (1979).

[100] L. Rayleigh, *The London, Edinburgh, and Dublin Philosophical Magazine and Journal of Science* **10**(60), 73–78 (1880).

[101] S. Chapman & J. Bartels, *Geomagnetism*, volume 2, Clarendon Press Oxford (1940).

[102] J. Linsley, *Phys. Rev. Lett.* **34**, 1530–1533 (1975).

[103] F. J. M. Farley & J. R. Storey, *Proceedings of the Physical Society. Section A* **67**(11), 996 (1954).

[104] D. Hall *et al.*, *Journal of Geophysical Research: Space Physics (1978–2012)* **104**(A4), 6737–6749 (1999).

[105] A. Lazarian & P. Desiati, *The Astrophysical Journal* **722**(1), 188 (2010).

[106] M. Amenomori *et al.* (Tibet ASγ Collaboration), *Science* **314**(5798), 439–443 (2006).

[107] M. G. Aartsen *et al.*, *The Astrophysical Journal* **765**(1), 55 (2013).

[108] S. Argiro *et al.*, *Nuclear Instruments and Methods in Physics Research Section A: Accelerators, Spectrometers, Detectors and Associated Equipment* **580**(3), 1485 – 1496 (2007).

[109] W. Fulgione, *private communication (Auger Technical Note GAP-2007-081)* (2007).

[110] P. Ghia & I. Lhenry-Yvon, *private communication (Auger Technical Note GAP-2007-132)* (2007).

[111] A. Chilingarian & T. Karapetyan, *Advances in Space Research* **47**(7), 1140 – 1146 (2011).

[112] L. I. Dorman, *Cosmic rays in the Earth's atmosphere and underground*, Astrophysics and Space Science Library, Springer, Dordrecht (2004).

[113] A. M. Hillas, *Nuclear Physics B - Proceedings Supplements* **52B**, 29 (1997).

[114] A. M. Hillas, *in Proceedings of the Paris Workshop on Cascade Simulations*, p. 39, Paris (1981).

[115] R. S. Fletcher *et al.*, *Phys. Rev. D* **50**, 5710–5731 (1994).

[116] E.-J. Ahn *et al.*, *Phys. Rev. D* **80**, 094003 (2009).

[117] N. Kalmykov, S. Ostapchenko & A. Pavlov, *Nuclear Physics B - Proceedings Supplements* **52**(3), 17 – 28 (1997).

[118] S. Ostapchenko, *Nuclear Physics B - Proceedings Supplements* **151**(1), 143 – 146 (2006).

[119] S. Macmillan & S. Maus, *Earth, Planets, and Space* **57**(12), 1135–1140 (2005).

[120] S. Sciutto, *in Proceedings of the 27th International Cosmic Ray Conference*, volume 1, p. 237, Hamburg (2001).

[121] P. K. F. Grieder, *Cosmic Rays at Earth: Researcher's Reference Manual and Data Book*, Elsevier Science, Amsterdam (2001).

[122] D. H. Hathaway, *Living Reviews in Solar Physics* **7**(1) (2010).

[123] J. H. Meeus, *Astronomical Algorithms*, Willmann-Bell, Incorporated (1991).